UNIVERSITEIT GENT

FACULTEIT WETENSCHAPPEN

EXPLORING THE LIMITS OF A HADRONIC PICTURE OF NUCLEI THROUGH PION AND NUCLEON REMOVAL REACTIONS

Wim Cosyn

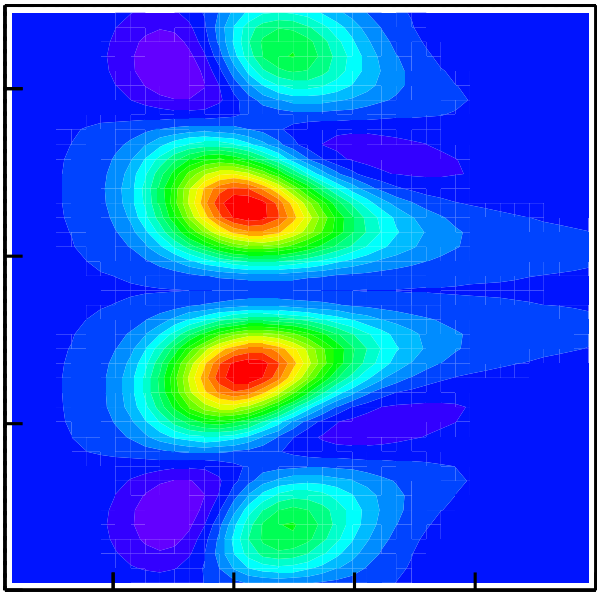

Promotor: Prof. dr. JAN RYCKEBUSCH

Proefschrift ingediend tot het behalen van de academische graad van
Doctor in de Wetenschappen: Fysica

Universiteit Gent
Faculteit Wetenschappen
Vakgroep Subatomaire en Stralingsfysica
Academiejaar 2008-2009

I'll tell you one thing.
There's nothing like building up an old automobile from scratch
and wiping out one of these Detroit machines.
That'll give you a set of emotions that'll stay with you.
Know what I mean? Those satisfactions are permanent.

G.T.O., Two Lane Blacktop

Preface

Omdat eerste zinnen vinden nooit mijn sterkste kant geweest is en er direct invliegen in een dankwoord misschien wel werkt...: Eerst en vooral bedankt, Jan, om al deze jaren een geduldig promotor te zijn. Mijn excuses om het de eerste lezer zo veelvuldig moeilijk te maken. Thank you, Cris, for guiding me during the first years of this work and being stubborn when it was needed. Thanks to Dipangkar, Ben, Ishay, Eli and Sabine for useful discussions and answering a lot of questions, on- and offline. Deze thesis zou ondenkbaar geweest zijn zonder al het vroegere werk van Pascal en Bart, jullie nalatenschap werd zeer geapprecieerd. Klaas, momenteel zit je luid te zuchten op een meter van me, maar ik vrees dat we de “Niet functioneren is geen schande” toch stilaan van de deur mogen halen. Merci voor het oplossen van vele computer-, fysica-, en andere problemen. Christophe hield het wat minder lang bij ons uit, maar ik zal altijd met weemoed aan die Turijnse winter in 2006 op het eerste verdiep terugdenken. Dank aan Lesley en Tim om het aantal dt fouten in de samenvatting met drie naar beneden te halen. Aan alle collega’s en ex-collega’s bedankt om voor vele onvergetelijke randanimatie sessies (al dan niet met proevertjes) te zorgen tijdens middag- en koffiepauzes. Ik heb meer bijgeleerd dan ik ooit vooraf kon vermoeden. Iedereen die de woensdag mee kwam voetballen, bedankt om mij al die tijd geen enkele blessure te bezorgen en de nodige (own)goals te laten scoren. Greets to all the cool physicists I met during HUGS and conferences. Exploring the local folklore with you was always very enlighting. Aan alle vrienden en vriendinnen die me de afgelopen jaren op allerlei dolle en minder dolle avonturen vergezeld hebben, het heeft me tonnen goeie herinneringen opgeleverd. Tenslotte, bedankt aan de familie om mij de hele tijd te sparen van lastige vragen!

Wim,
maart 2009

Contents

Chapter 1

Introduction

The building blocks of visible matter (ranging from cells to stars) consist of nuclei. Research in nuclear physics and the technological advances spurred by its demands have made a large impact on society. It has for example, resulted in the building of nuclear power plants, which account for a significant share of the global electricity production. Nuclear sources are also used to power pacemakers, ships and space vehicles. The development of the atomic bomb and the threat of nuclear warfare made a large impact on international relations in the second half of the 20th century. Radioactive isotopes are used in many medical procedures and proton radiation therapy provides a more controllable alternative to more standard therapies that involve electrons. Accelerator mass spectrometry is used in archaeology, environmental and biomedical research. The tools used in the ion doping of integrated circuits or medical prosthetics are spin-offs from accelerator technology used in nuclear physics.

The nucleus, however, still harbours a lot of uncharted territory. Since the experiments of Rutherford [1], Chadwick's discovery of the neutron [2] and the work of Yukawa [3], we adopt the picture that a nucleus is made up of protons and neutrons held together by the meson-mediated strong force. The development of Quantum Chromodynamics (QCD) and the deep inelastic scattering experiments in the 1950s and 1960s provided evidence that quarks and gluons are the fundamental degrees of freedom of the strong force. The use of colorless nucleons and mesons as effective degrees of freedom in the nucleus, stems from the inability to solve QCD in the confinement region and has proved highly efficient and successful. The study of the crossover from hadronic to partonic degrees of freedom is an active and exciting line of current research [4]. To map the transition region, one can look for the onset of phenomena originating from QCD predictions as deviations from standard nuclear-physics predictions. In this work we adopt the view that QCD phenomena can be clearly identified when there are deviations between meaurements and sophisticated

calculations that adopt hadronic degrees of freedom.

Color Transparency

One of the QCD predictions is the color transparency (CT) effect. For recent overviews of the phenomenon, we point the reader to [5, 6]. Color transparency was first described by Mueller and Brodsky [7, 8] and deals with the expansion of a small-sized configuration of quarks into a regular hadron state. To the nuclear medium, this small-sized configuration (also called Point Like Configuration or PLC) seems a colorless object and the mechanisms of nuclear shadowing lose in importance: the normally strong interacting hadron can propagate without final-state interactions (FSI). This can be compared to several similar effects in QED. An electron-positron pair experiences a reduced energy loss in the vicinity of their creation point due to internal screening of their charges. This is called the King-Perkins-Chudakov effect [9], and has been observed in cosmic ray tracks [10, 11] and a gold target [12]. A similar reduction of interactions can be observed in vacuum-assisted photo-ionization [13]. The created electron-positron pair that mediates the ionization is subject to charge screening, lowering the ionization cross section. Cerenkov radiation is also found to be reduced for radiation from a electron-positron pair when the pair separation is smaller than the wavelength of the emitted light [14], and relativistic positronium beams become "super-penetrating" for solid targets [15–18].

In order to observe true color transparency, three conditions must be satisfied [19–22]:

1. **Reactions with a high momentum transfer squared.** This is related to the uncertainty principle: an impinging particle with high momentum and correspondingly small de Broglie wavelength, will probe small distance scales. When hitting a confined colored quark, it can only interact with quarks in a small region within the range associated with the wavelength of the probe before hadronization occurs. This production of an object with small size was originally derived as a consequence of perturbative QCD at very high Q^2 [23, 24]. Studies within hadronic models, however, have shown that a PLC could be produced at momentum transfers squared as low as $1-2$ $(\mathrm{GeV/c})^2$ [25, 26].

2. **The PLC experiences reduced interactions (color screening).** The diagram of lowest order describing the interaction between a color singlet and the medium involves the exchange of two gluons. One of the possible diagrams is depicted in Fig. 1.1. Perturbative QCD dictates that the cross section of the singlet-medium reaction is proportional to b^2, with b the transverse distance between the constituents of the singlet. For a PLC, the interactions with the medium will hence vanish. One can com-

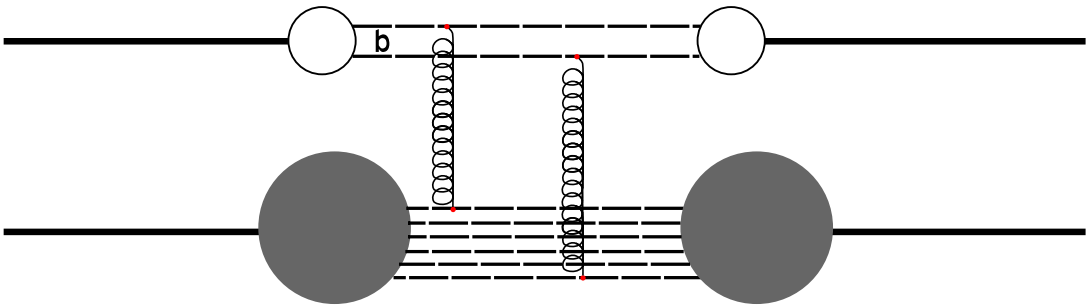

Figure 1.1 One of the possible lowest-order diagrams for the interaction of a color singlet of two constituents with transverse size b, with a medium containing constituents grouped in colorless objects. The thick incoming and outgoing lines stand for colorless objects. The two gluons can originate and end on any of the constituents, and cross diagrams are also possible.

pare this behaviour to the reduced interaction experienced by an object with a small dipole moment in QED.

3. **Ejected particles with a high momentum.** As the PLC is not an eigenstate of the QCD Hamiltonian, it will evolve to the normal hadron state along a certain *formation length* l_f. As the lifetime of the PLC is dilated in the rest frame of the nucleus, higher PLC momenta imply a larger l_f. In order to maximize the color-transparency phenomenon, the condition $l_f \gg R_A$ (with R_A the radius of the nucleus) should be met. Under current experimental conditions, this condition is as yet not fulfilled and the PLC expands in the nucleus and is subject to FSI while traversing the nucleus ($l_f \approx R_A$).

The observable measured in experiments in search for CT is the nuclear transparency, defined as the ratio of the cross section per target nucleon for a process on a nucleus to the cross section of the process on a free nucleon

$$T = \frac{\sigma^{\text{nucleus}}}{A\sigma^{\text{free nucleon}}}. \tag{1.1}$$

Accordingly, the nuclear transparency provides a measure of the attenuation effects of the nuclear medium on the hadrons produced in some reaction. One can study the hard-scale dependence of the transparency for a certain target nucleus A, or the A dependence at a fixed value of the hard-scale parameter. If CT effects were to appear at a certain energy, the nuclear transparency would be observed to overshoot the predictions from traditional nuclear physics expectations. The measurement of the onset and magnitude of the CT effect allows to constrain models describing the evolution of a PLC into a hadron. The CT effect also plays a role in the access to generalized parton distributions (GPDs) in deeply virtual Compton scattering (DVCS) and meson production (DVMP) processes [27, 28], as it is a

necessary condition for factorization to occur. The factorization is related to the assumption that from a certain virtuality the soft and hard physics can be separated.

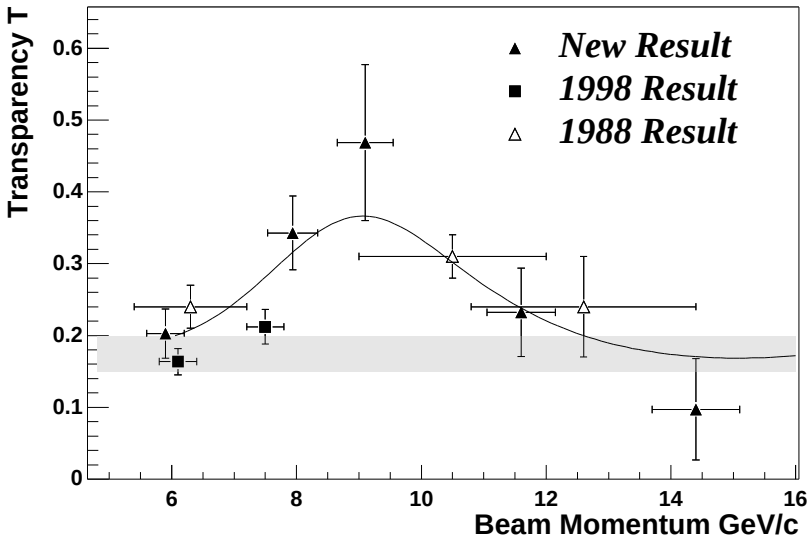

Figure 1.2 The transparency T versus beam momentum for the $^{12}C(p,2p)$ reaction. Data are from Refs. [29–31]. The shaded band represents a Glauber calculation from Ref. [32] and the solid curve a parametrization from Ref. [33]. Figure taken from Ref. [31].

Since the late 1980s several experiments looking for signs of color transparency have been performed for a variety of reactions. So far, there is no conclusive evidence for the CT effect. The $^{12}C(p,2p)$ reaction was studied a t Brookhaven National Laboratory (BNL) [29–31]. As shown in Fig. 1.2, the transparency for the $^{12}C(p,2p)$ reaction first shows a rise as a function of incoming beam momentum, but drops again for momenta larger than 9 GeV/c. This behavior is not in line with traditional nuclear physics calculations. However, it is currently not considered a clean sign of CT, but also attributed to nuclear filtering [33, 34] or the threshold for charm resonance production [35]. Several experiments [36–41] have measured the transparency using the $A(e,e'p)$ reaction up to $Q^2 = 8.1$ $(\mathrm{GeV/c})^2$ for targets including deuterium, carbon, iron and gold. No sign of CT was observed up to the largest energies.

As a meson has two constituent quarks, one could expect that signatures of CT occur at lower energies compared to a baryon. Indeed, it seems easier to produce a PLC with two constituents. Measurements of the transparency for the production of ρ^0 mesons at Fermilab [42] showed a positive slope in the Q^2 dependence of α in the parametrization $T = A^{\alpha-1}$, indicating CT effects. However, this slope has since been associated with variations in the initial state interactions associated with the fluctuation of the virtual photon into

a $q\bar{q}$-pair [43]. More recent measurements at DESY [44] for ρ^0 production from a ^{1}H and ^{14}N target at $Q^2 = 0.9 - 3$ (GeV/c)^2 show a rise in the nuclear transparency. Another experiment at JLab measuring incoherent ρ^0 production is completed and under analysis [45]. The measurement of the cross section of diffractive dissociation of 500 GeV/c pions into dijets at Fermilab [46] yielded the clearest signal of CT so far. The cross section was parametrized as $\sigma = \sigma_0 A^\alpha$, with σ_0 a constant independent of A. The fitting value of $\alpha \approx 1.55$ deviates from the nominal value of 2/3 and is in agreement with calculations assuming 100% color transparency. The value of Q^2 in this experiment was estimated at $Q^2 \gtrsim 10$ (GeV/c)^2. As such, the Fermilab results do not give a precise value for the hard scale where CT effects start appearing, but only places an upper limit on it.

During the last couple of years, three specific experiments to measure transparencies have been conducted at the 6 GeV electron accelerator in Jefferson Lab. Two had a pion, and the third two protons in the final state. The nuclear transparency for the pion photoproduction process $A(\gamma, \pi^- p)A-1$ in ^{4}He [47] and for double proton knockout $A(\gamma, pp)A-2$ in ^{3}He and ^{12}C [48, 49] have been measured in Hall A. In Hall C, data was taken for the pion electroproduction process $A(e, e'\pi^+)$ in ^{4}He, ^{27}Al, ^{63}Cu and ^{197}Au [50].

Short-Range Correlations

In a many-body system, correlations between the constituents of the system are induced by the interparticle forces. For a system with a one-body density $\rho(\vec{r})$, the two-body density $\rho(\vec{r}_1, \vec{r}_2)$ can be expressed as the conditional probability of finding a particle at $\vec{r}_1$ if there is one present at $\vec{r}_2$:

$$\rho(\vec{r}_1, \vec{r}_2) = \rho(\vec{r}_1)\rho(\vec{r}_2)g(|\vec{r}_1 - \vec{r}_2|), \tag{1.2}$$

with $g(r)$ the correlation function. In the absence of correlations, $g(r) \equiv 1$ and all particles move independently of each other. For an atomic ^{4}He liquid, the correlation function was measured with neutron [51] and X-ray [52] scattering and is shown in Fig. 1.3. The correlations are a consequence of the hard repulsive core of the interatomic potential $v(r)$ that is also shown in Fig. 1.3. The hard core reflects itself in $g(r)$ becoming zero for small interparticle separations. For larger distances, $g(r)$ rises, and then oscillates before reaching the asymptotic value of 1. These correlations increase the high-momentum components in the momentum distribution of the atoms in the liquid.

Since its conception in the 1950s, the nuclear shell model has provided us with an efficient approach to the nuclear many-body problem. In the nuclear shell model, the nucleons are fermions that move independently in a mean field that accounts for a great

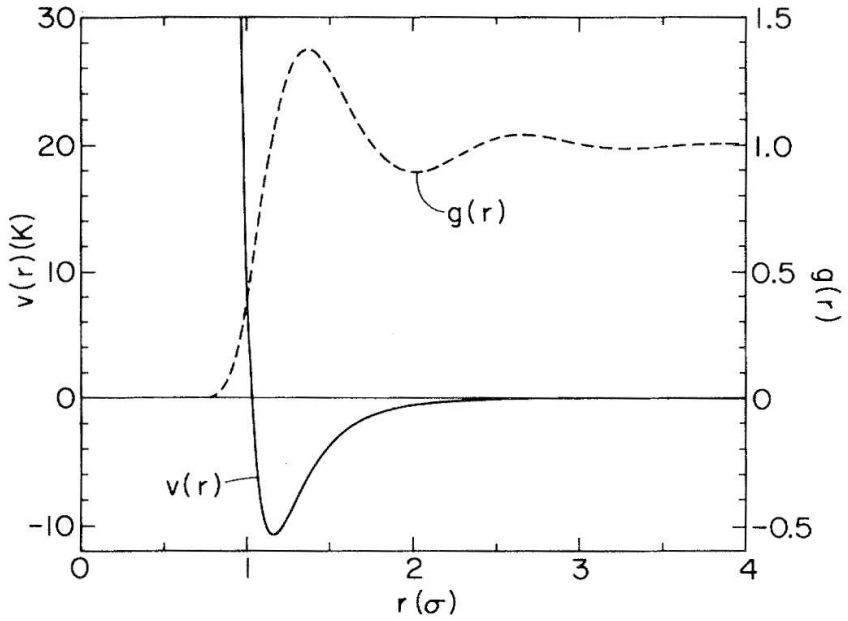

Figure 1.3 Interatomic potential $v(r)$ and correlation function $g(r)$ for an atomic ^{4}He liquid. σ is a measure for the diameter of ^{4}He. Figure taken from [53].

fraction of the interactions with the other nucleons. In the nuclear shell model, the A-nucleon wave functions are Slater determinants with single-nucleon wave functions that are eigenfunctions of the Hamiltonion. The latter conatins a kinetic energy term and a mean-field potential. As the Pauli principle prevents two nucleons from occupying the same single particle state, quantum levels are filled up to the Fermi-level for the ground state of the nucleus.

Since the nucleons move in a mean-field potential, no explicit correlations between two nucleons are present in the nuclear shell model wave functions. The realistic nucleon-nucleon interaction consists of an attractive long distance part and a strong repulsive part for separations shorter than 0.8 fm, all depending on the spins and isospins of the two nucleons. The nuclear mean-field potential does not fully account for all aspects of the nucleon-nucleon interaction. In particular, the repulsive hard core and tensor part give rise to short-range correlations (SRC) that go beyond the typical mean-field approach. As two nucleons get close together, the strong repulsion induces pairs with a high relative momentum. As the nucleus is a closely packed system, those correlations make significant contributions to the total wave function. The SRC cause high-density fluctuations in the nucleus and might allow us to access cold dense matter like one would encounter in neutron stars [54]. They enhance the high-momentum part of the shell model wave function [55] and deplete (populate) levels below (above) the Fermi-sea. As the SRC play at a small distance scale, their effect should be relatively A independent. This is confirmed by the

scaling of high momentum components in the nuclear wave functions of light and complex nuclei to those of the deuteron wave function [56]. The long-range correlations (LRC) associated with pion exchange induce modifications to shell model properties and give rise to highly collective modes, like giant resonances, in nuclei.

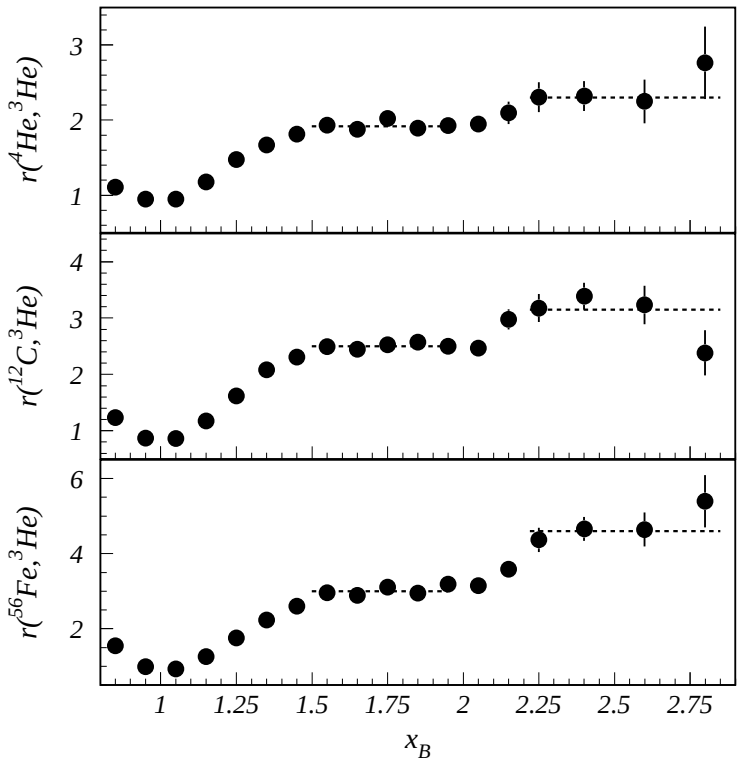

Figure 1.4 Weighted inclusive electron scattering cross sections ratios for ^{4}He (upper panel), ^{12}C (middle panel) and ^{56}Fe (lower panel), to the ^{3}He one as a function of Bjorken x. The horizontal dashed lines indicate the NN and $3N$ scaling regions. Figure taken from Ref. [57].

One- and two-nucleon knockout reactions have the potential to probe SRC. In inclusive $A(e,e')$ measurements performed at Hall B in JLab, scaling was observed in the ratio of the cross section of the different nuclei to the ^{3}He one for Bjorken x values of $1.5 < x < 2$ and $2.25 < x$ [57, 60] (see Fig. 1.4). The observed scaling suggests that the electrons probe high-momentum bound nucleons originating from two-nucleon (first plateau) and three-nucleon (second plateau) SRC. Moreover, the similar shape of the scaling for all measured nuclei implies that the properties of these SRC do not depend on the residual nucleus. $A(e,e'p)$ experiments showed the spectroscopic strength of valence protons was only 55 to 75 % of the value predicted by shell model calculations, and around 10 % for shells just above the Fermi sea [61]. Calculations showed both SRC and LRC contribute to these values [62]. Measurements with missing momentum above 300 MeV and missing energy

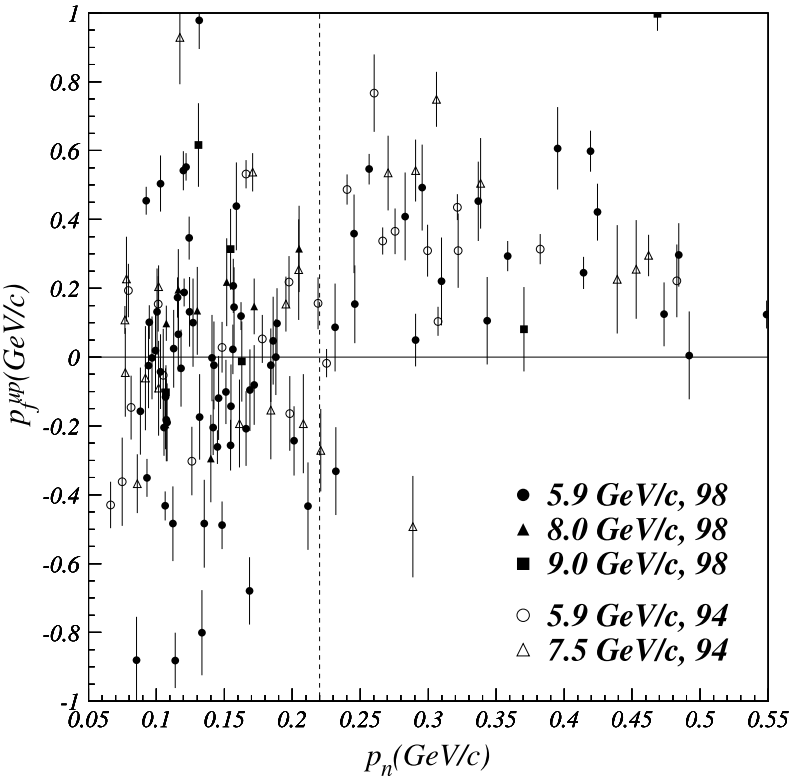

Figure 1.5 Scatter plot of the projection p_f^{up} of the initial proton momentum on an axis opposite to the momentum of the detected neutron versus the neutron momentum p_n in the $^{12}C(p,ppn)$ reaction. Data are labelled according to the initial beam momentum. Data labelled *98* (*94*) are from Refs. [58] ([59]). The vertical dashed line at 0.22 GeV/c corresponds to k_F, the Fermi momentum for ^{12}C. Figure taken from Ref. [58]

larger than 50 MeV also yielded strengths larger up to an order of a magnitude than shell-model predictions [63]. The results (Fig. 1.5) of the $^{12}C(p,ppn)$ experiment carried out at BNL by the EVA collaboration [58], show that the neutron in the final state is accompanied by a proton in a random direction for neutron momenta below the Fermi surface ($\sim$ 220 MeV). For neutron momenta exceeding the Fermi surface on the other hand, all the protons were emitted with a projection ≥ 0. This translates to proton-neutron angles larger than 90 degrees. These directional correlations again form a clear signature of the dominance of SRC for high momentum nucleons. A recent $^{12}C(e,e'pN)$ experiment at Hall A in Jefferson Lab provided indications that about 20% of the nucleons in carbon form correlated pairs [64, 65]. Of those about 90 % is of the proton-neutron type, as shown in Fig. 1.6.

Outline

In this thesis, we present a model that can be used to describe pion and double nucleon removal reactions. It enables us to calculate transparencies and compare them with the

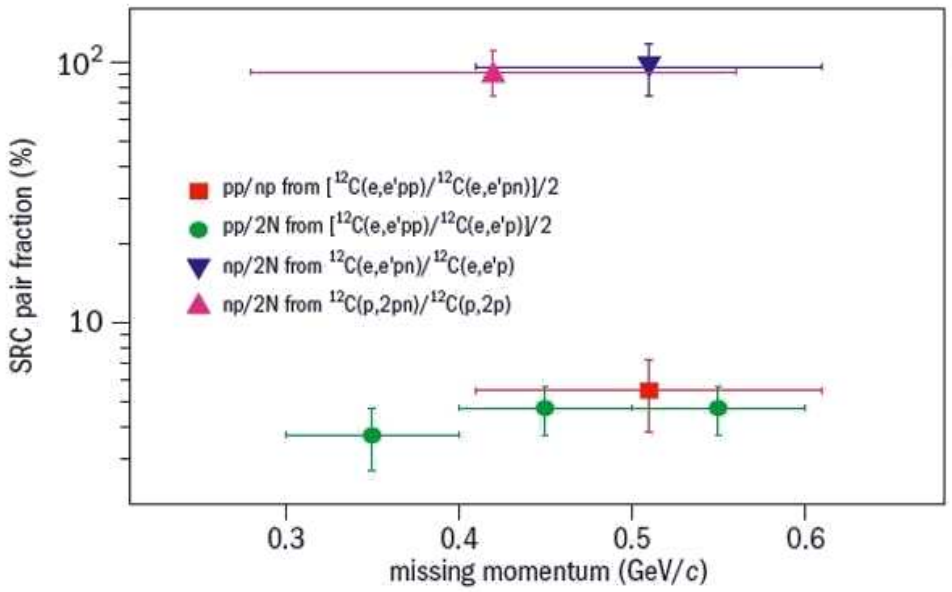

Figure 1.6 Relative abundance of pp- and np-pairs for the ^{12}C(e,e'pN) [65] and ^{12}C(p,2pn) reaction [58]. Figure taken from Ref. [66].

data from the above-mentioned recent experiments. Three essential ingredients will draw our attention:

- The hard process of the beam interacting with a constituent of the nucleus and producing the ejected particles in the final state.
- The structure of the target and residual nucleus.
- The propagation of the ejected particles through the nuclear medium and their FSI with the residual nucleons.

We assume that the incoming beam interacts with one of the bound nucleons, which is known as the impulse approximation (IA). Two different approaches are used to model the hard process. For the pion removal reactions, we factorize the amplitude into a part containing the pion production process and a part containing the FSI. This yields an expression for the cross section for a nuclear target that can be related to their counterparts for a free nucleon target. For the description of the two-nucleon knockout process, we employ an unfactorized amplitude by including an explicit form for the interaction of the photon with a bound nucleon, and by relating the hard nucleon-nucleon scattering amplitude to a parametrization for the free-space amplitude obtained from the SAID database [67].

In our work, the wave functions of the target and residual nucleus are obtained in an independent particle model (IPM). The single-particle wave functions in the A-body Slater

determinants are solutions of a one-body Dirac equation with a spherically symmetric Dirac potential. We use relativistic bound-state single particle wave functions calculated in the Hartree approximation of the $\sigma - \omega$ model [68–70].

The experiments considered in this work have kinematics with outgoing particle momenta of a few GeV/c. In this range, the eikonal approximation (EA) can be employed to describe the FSI. The EA was first used in optics. When light has a wavelength that is smaller than the reflecting and refracting objects that it finds on its way, one-dimensional rays suffice to describe the physics of the process. Similarly, in quantum mechanics the EA can be used for the small-angle scattering of high energy particles in a potential V. For a non-relativistic incoming particle with energy $E = \frac{(\hbar k)^2}{2m}$, the condition on the wavelength in optics translate to $V/E \ll 1$ and $\frac{1}{V/E} \ll ka \ll \frac{1}{(V/E)^2}$, with a the scattering length of the potential [71]. A relativistic formulation of the eikonal approximation has been developed for ejected nucleons and applied to $A(e,e'p)$ [72, 73] and $A(p,2p)$ [74, 75] reactions. In this work, we extend this model, based on multiple-scattering Glauber theory, to accommodate outgoing pions. This provides us with a framework that can be applied to a broad spectrum of reactions with hadronic or leptonic probes and outgoing nucleons and/or pions.

The outline of this work is as follows.

- Chapter 2 describes the theoretical framework that has been developed to model the pion and two-nucleon knockout reactions. First, a factorized expression for the electromagnetically induced $A(\gamma, N\pi)$ cross section is derived. In a next step, this is extended to the pion electroproduction reaction $A(e,e'\pi)$. For the $A(\gamma, NN)$ reaction, we consider two competing reaction mechanisms and describe both in an unfactorized manner. First, we assume that the two-nucleon knockout can be the result of the breakup of a correlated nucleon-nucleon pair. Thereby, the photon interacts with one nucleon in the pair and both are ejected. A competing mechanism is hard rescattering whereby the ejectile induces a hard nucleon-nucleon interaction that makes two nucleons to reach the detectors.
  In Section 2.2 we deal with the implementation of the FSI. We introduce a relativistic multiple-scattering Glauber approximation (RMSGA) to treat the FSI of nucleons and pions with intermediate to high momentum. Special attention is paid to a parametrization of the πN scattering parameters which are required in Glauber calculations. For nucleons with low momentum we cover an alternative implementation of the FSI by means of optical potentials in an eikonal approach.
  Sections 2.3 and 2.4 explain how the CT and SRC effects are implemented in our

model. Color transparency is included through the quantum diffusion model and correlations through a well chosen correlation function that modifies the one-body density. In our procedure, the proper normalization of the wave functions is guaranteed.

- Chapter 3 deals with the results of the numerical calculations done with our model. We start with a detailed study of the FSI factor, wherein all effects of the FSI are contained. Next, we show the results of the transparency calculations for the different reactions. We study the influence of the CT and SRC effects on these results and try to distinguish between the two. In order to value the robustness of the results of our model, we compare them with predictions from alternative approaches. In the final section, we investigate the density dependence of several reactions. We study the influence of the FSI on the effectively probed density and compare reactions involving one $\big((e,e'p)\big)$, two $\big((\gamma,pp)\big)$, and three $\big((p,2p)\big)$ nucleons.

- Finally, our conclusions are stated in Chapter 4. Appendix A gives an overview of the adopted notations. The bound-state wave functions used in the model to describe the target and residual nucleus are covered in Appendix B. Appendix C treats the scattering of a relativistic spinless particle in a potential. The transformations for the representations used for the hard nucleon-nucleon rescattering matrix element are outlined in Appendix D. Eventually, Appendix E lists the parametrization used for the free pion electroproduction cross section.

Chapter 2

Formalism

2.1 Kinematics and Observables

In this section, the formalism for the description of two types of reactions covered in this thesis is outlined. We adopt the conventions $\hbar = c = 1$. In subsec. 2.1.1, the factorized form of the differential cross section for pion photoproduction from a nucleus is derived. It is shown that, even when excluding final state interactions, the factorization is not exact and can only be achieved after neglecting the negative energy contributions. In subsec. 2.1.2, the factorization scheme is extended to pion electroproduction reactions. Subsec. 2.1.3 introduces the two competing reaction mechanisms for $A(\gamma, NN)$: knockout of a correlated nucleon pair and hard rescattering.

2.1.1 Pion Photoproduction: The $A(\gamma, N\pi)$ Cross Section

We use the following notations for the four-momenta in the laboratory frame: $q^\mu(q,\vec{q})$ for the photon, $P_A^\mu(E_A,\vec{p}_A=\vec{0})$ for the target nucleus, $P_{A-1}^\mu(E_{A-1},\vec{p}_{A-1})$ for the residual nucleus, $P_N^\mu(E_N,\vec{p}_N)$ and $P_\pi^\mu(E_\pi,\vec{p}_\pi)$ for the ejected nucleon and pion. The missing momentum $\vec{p}_m$ is defined as $\vec{p}_m \equiv -\vec{p}_{A-1} = \vec{p}_N + \vec{p}_\pi - \vec{q}$ and the outgoing nucleon has spin m_s. The fivefold differential cross section in the laboratory frame reads [76]

$$\frac{d^5\sigma}{dE_\pi d\Omega_\pi d\Omega_N} = \frac{M_{A-1} m_N p_\pi p_N}{4(2\pi)^5 q E_A} f_{\text{rec}}^{-1} \overline{\sum_{fi}} \left| \mathscr{M}_{fi}^{(\gamma,N\pi)} \right|^2 , \tag{2.1}$$

where M_A, M_{A-1} and m_N denote the rest mass of the target nucleus, the residual nucleus and the nucleon, respectively. $\overline{\sum}_{fi}$ involves an averaging over the photon polarizations and a summation over the spins of the final particles. The recoil factor f_{rec} is given by

$$f_{rec} = \frac{E_{A-1}}{E_A} \left| 1 + \frac{E_N}{E_{A-1}} \left(1 + \frac{(\vec{p}_\pi - \vec{q}) \cdot \vec{p}_N}{p_N^2} \right) \right| , \tag{2.2}$$

and $\mathscr{M}_{fi}^{(\gamma,N\pi)}$ denotes the invariant matrix element:

$$\mathscr{M}_{fi}^{(\gamma,N\pi)} = \langle P_\pi^\mu, P_N^\mu m_s, P_{A-1}^\mu J_R M_R | \hat{\mathscr{O}} | q^\mu, P_A^\mu 0^+ \rangle \,, \tag{2.3}$$

where $J_R M_R$ are the quantum numbers of the residual nucleus. We restrict ourselves to processes with an even-even target nucleus A.

The ground-state wave function of the target nucleus $|P_A^\mu 0^+\rangle \equiv \Psi_A^{g.s.}(\vec{r}_1,\ldots,\vec{r}_A)$ is obtained by fully antisymmetrizing the product of the individual nucleon wave functions ϕ_α. We model the pion photoproduction process by means of a contact interaction: the initial nucleon, impinging photon, and the ejected pion and nucleon join in a single space-time vertex. As the process can take place on any of the nucleons in the target nucleus, we get the following expression for the corresponding photoproduction operator:

$$\hat{\mathscr{O}} = \sum_{i=1}^{A} O_\mu(\vec{r}_i) \,. \tag{2.4}$$

We assume that $\hat{\mathscr{O}}$ is exempted from medium effects. This is a common assumption in nuclear and hadronic physics and is usually referred to as the impulse or quasi-free approximation (IA). In the context of $A(e,e'p)$ reaction, for example, the impulse approximation provides a fair description of the data [72]. It is also applied in the experimental analysis of Ref. [50] and the model of Ref. [77]. The impinging photon with polarization λ is represented by

$$A^\mu(\lambda,\vec{r}_i) = \epsilon^\mu(\lambda) e^{i\vec{q}\cdot\vec{r}_i} \,. \tag{2.5}$$

Here, $\epsilon^\mu(\lambda)$ is the polarization four-vector of the photon. The wave function of the ejected nucleon is written as

$$|P_N^\mu m_s\rangle \equiv \Psi^{(+)}_{\vec{p}_N,m_s}(\vec{r}_i) = \hat{\mathscr{S}}^\dagger_{N'N}(\vec{r}_i;\vec{r}_1,\ldots,\vec{r}_{j\neq i},\ldots,\vec{r}_A) u(\vec{p}_N,m_s) e^{i\vec{p}_N\cdot\vec{r}_i} \,, \tag{2.6}$$

which is the product of a positive-energy Dirac plane wave $\phi_{\vec{p}_N}(\vec{r}_i) = u(\vec{p}_N,m_s)e^{i\vec{p}_N\cdot\vec{r}_i}$ and an operator $\hat{\mathscr{S}}^\dagger_{N'N}$. This operator describes the attenuation of the ejected nucleon through soft final-state interactions with the other nucleons. The wave function for the ejected pion adopts a similar form as the nucleon one, i.e. a plane wave convoluted with a FSI factor $\hat{\mathscr{S}}^\dagger_{\pi N}$:

$$|P_\pi^\mu\rangle \equiv \Phi^{(+)}_{\vec{p}_\pi}(\vec{r}_i) = \hat{\mathscr{S}}^\dagger_{\pi N}(\vec{r}_i;\vec{r}_1,\ldots,\vec{r}_{j\neq i},\ldots,\vec{r}_A) e^{i\vec{p}_\pi\cdot\vec{r}_i} \,. \tag{2.7}$$

The final A-nucleon wave function is constructed by antisymmetrizing $\Psi^{(+)}_{\vec{p}_N,m_s}$ with the wave function for the residual nucleus $\Psi_{A-1}^{J_R,m_R}$:

$$\begin{aligned} |P_N^\mu m_s, P_{A-1}^\mu J_R M_R\rangle \equiv \Psi_A^{\vec{p}_N,m_s}(\vec{r}_1,\ldots,\vec{r}_A) = \\ \hat{\mathscr{A}}\left[\hat{\mathscr{S}}^\dagger_{N'N}(\vec{r}_1;\vec{r}_2,\ldots,\vec{r}_A) u(\vec{p}_N,m_s) e^{i\vec{p}_N\cdot\vec{r}_1} \Psi_{A-1}^{J_R,m_R}(\vec{r}_2,\ldots,\vec{r}_A)\right] . \end{aligned} \tag{2.8}$$

As $\Psi_A^{\text{g.s.}}$ and $\Psi_A^{\vec{p}_N,m_s}$ are fully antisymmetric, each term of the operator (2.4) will yield the same contribution to the matrix element (2.3) and we can restrict ourselves to the term with coordinate $\vec{r}_1$ and multiply it with A. With the above expressions for the operator and the wave functions of the hadrons involved in the reaction, we can write for the matrix element of Eq. (2.3) in coordinate space:

$$\mathcal{M}_{fi}^{(\gamma,N\pi)} = A \int d\vec{r}_1 \int d\vec{r}_2 \ldots \int d\vec{r}_A \left[\Psi_A^{\vec{p}_N,m_s}\left(\vec{r}_1,\vec{r}_2,\ldots,\vec{r}_A\right)\right]^\dagger \times e^{-i\vec{p}_\pi\cdot\vec{r}_1}\hat{\mathcal{S}}_{\pi N}(\vec{r}_1;\vec{r}_2,\ldots,\vec{r}_A)O_\mu(\vec{r}_1)\epsilon^\mu(\lambda)e^{i\vec{q}\cdot\vec{r}_1}\Psi_A^{g.s.}\left(\vec{r}_1,\vec{r}_2,\ldots,\vec{r}_A\right) . \quad (2.9)$$

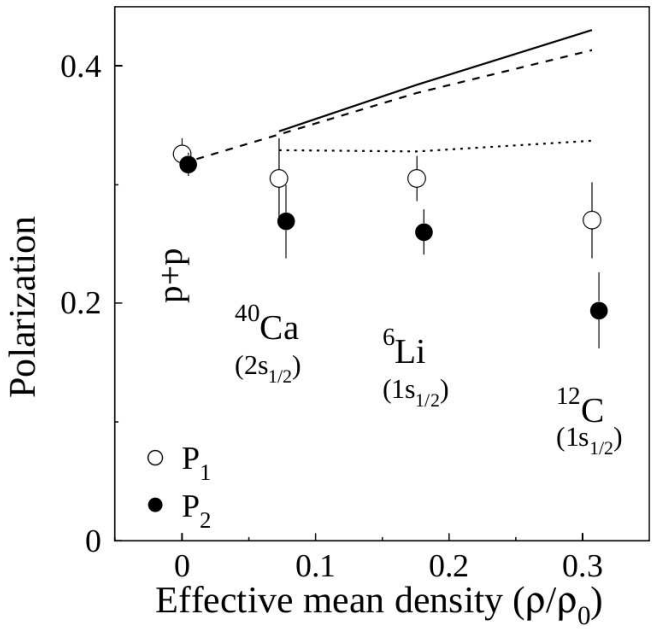

Figure 2.1 Target dependence of the polarization data for $p-p$ scattering and $(p,2p)$ reactions. P_1 (P_2) denotes the polarization of the fast forward (slow backward) nucleon. The solid (dashed) curve represents a DWIA (PWIA) calculation [78, 79]. The PWIA result is extended to free proton-proton scattering, where the value was obtained from a $p-p$ scattering phase- shift analysis [80]. The dotted line is the DWIA result is the DWIA result, in which the relativistic effect is taken into account in a Schrödinger equivalent form. Figure taken from Ref. [81].

We assume that $\hat{\mathcal{S}}_{N'N}$ and $\hat{\mathcal{S}}_{\pi N}$ are spin independent and only retain the central part of the FSI. This is a commonly used approximation in calculations for $A(e,e'p)$, $A(p,2p)$ and proton-nucleus reactions, based on the rapid decrease of the contribution from the spin-dependent terms in the intermediate energy range. A recent experiment measured the polarization for the fast forward and slow backward outgoing proton in the $A(p,2p)$ reaction for several nuclei (^{6}Li, ^{12}C and ^{40}Ca) [81]. As is shown in Fig. 2.1, a decrease of the polarization with raising density was observed, but the effect for the fast proton

($p_N \approx 800$ MeV), was a lot smaller than for the slow proton ($p_N \approx 180$ MeV). We also assume that only elastic and mildly inelastic collisions with the spectator nucleons occur. The actual nuclear transparency measurements select events whereby the undetected final state with $(A-1)$ nucleons $\left|P^{\mu}_{A-1} J_R M_R\right\rangle$ is left with an excitation energy of the order of 100 MeV or less, which makes these assumptions very plausible. In computing the matrix element of Eq. (2.9) we consider processes of the type displayed in Fig. 2.2. The following spectator approximation is assumed to be valid for a struck nucleon with quantum numbers α_1 :

$$
\begin{aligned}
\int d\vec{r}_1 \ldots \int d\vec{r}_A \Big[& \phi_{\vec{p}_N}(P_n(\vec{r}_1)) \hat{\mathscr{S}}^{\dagger}_{N'N}(P_n(\vec{r}_1); P_n(\vec{r}_2), \ldots, P_n(\vec{r}_A)) \\
& \times \phi_{\alpha_2}(P_n(\vec{r}_2)) \ldots \phi_{\alpha_A}(P_n(\vec{r}_A)) \Big]^{\dagger} e^{-i\vec{p}_\pi \cdot \vec{r}_1} \hat{\mathscr{S}}_{\pi N}(\vec{r}_1; \vec{r}_2, \ldots, \vec{r}_A) \\
& \times O_\mu(\vec{r}_1) e^{i\vec{q}\cdot\vec{r}_1} \phi_{\alpha_1}(P_m(\vec{r}_1)) \phi_{\alpha_2}(P_m(\vec{r}_2)) \ldots \phi_{\alpha_A}(P_m(\vec{r}_A)) \\
& \approx \delta_{P_n(\vec{r}_2) P_m(\vec{r}_2)} \ldots \delta_{P_n(\vec{r}_A) P_m(\vec{r}_A)} \int d\vec{r}_1 \ldots \int d\vec{r}_A \\
& \times \phi^{\dagger}_{\vec{p}_N}(\vec{r}_1) \hat{\mathscr{S}}_{N'N}\left(\vec{r}_1; P_n(\vec{r}_2), \ldots, P_n(\vec{r}_A)\right) e^{-i\vec{p}_\pi \cdot \vec{r}_1} \hat{\mathscr{S}}_{\pi N}(\vec{r}_1; \vec{r}_2, \ldots, \vec{r}_A) \\
& \times O_\mu(\vec{r}_1) e^{i\vec{q}\cdot\vec{r}_1} \phi_{\alpha_1}(P_m(\vec{r}_1)) |\phi_{\alpha_2}(P_m(\vec{r}_2))|^2 \ldots |\phi_{\alpha_A}(P_m(\vec{r}_A))|^2 ,
\end{aligned}
\tag{2.10}
$$

with P_m and P_n permutations of the set $\{\vec{r}_1, \ldots, \vec{r}_A\}$ occurring in the antisymmetrization of the nucleon wave functions. Due to the presence of the δ-functions, the right-hand side of Eq. (2.10) is non-vanishing under the condition that $P_m(\vec{r}_1) = \vec{r}_1$ and $P_m(\vec{r}_i) = P_n(\vec{r}_i)$ for $i = 2, .., A$. This means that both the bound wave function α_1 and the ejected nucleon have the same spatial coordinate as the operator, $\vec{r}_1$. Moreover, all $(A-1)!$ permutations of the subset $\{\vec{r}_2, \ldots, \vec{r}_A\}$ yield an identical right-hand side.

Thus, after expanding the wave functions in Eq. (2.9) and employing Eq. (2.10), we arrive at

$$
\begin{aligned}
\mathscr{M}^{(\gamma, N\pi)}_{fi} \approx \frac{A(A-1)!}{A!} \int d\vec{r}_1 \int d\vec{r}_2 \ldots \int d\vec{r}_A \Big[& |\phi_{\alpha_2}(\vec{r}_2)|^2 \ldots |\phi_{\alpha_A}(\vec{r}_A)|^2 u^{\dagger}(\vec{p}_N, m_s) \\
& \times \hat{\mathscr{S}}_{\pi N}(\vec{r}_1; \vec{r}_2, \ldots, \vec{r}_A) \hat{\mathscr{S}}_{N'N}(\vec{r}_1; \vec{r}_2, \ldots, \vec{r}_A) \epsilon^{\mu}(\lambda) O_\mu(\vec{r}_1) e^{-i\vec{p}_m \cdot \vec{r}_1} \phi_{\alpha_1}(\vec{r}_1) \Big] .
\end{aligned}
\tag{2.11}
$$

We now define the FSI factor $\mathscr{F}_{\rm FSI}(\vec{r})$:

$$
\mathscr{F}_{\rm FSI}(\vec{r}) = \int d\vec{r}_2 \ldots \int d\vec{r}_A |\phi_{\alpha_2}(\vec{r}_2)|^2 \ldots |\phi_{\alpha_A}(\vec{r}_A)|^2 \hat{\mathscr{S}}_{\pi N}(\vec{r}; \vec{r}_2, \ldots, \vec{r}_A) \hat{\mathscr{S}}_{N'N}(\vec{r}; \vec{r}_2, \ldots, \vec{r}_A) , \tag{2.12}
$$

and write

$$
\mathscr{M}^{(\gamma, N\pi)}_{fi} \approx \int d\vec{r}_1 \mathscr{F}_{\rm FSI}(\vec{r}_1) u^{\dagger}(\vec{p}_N, m_s) \epsilon^{\mu}(\lambda) O_\mu(\vec{r}_1) e^{-i\vec{p}_m \cdot \vec{r}_1} \phi_{\alpha_1}(\vec{r}_1) . \tag{2.13}
$$

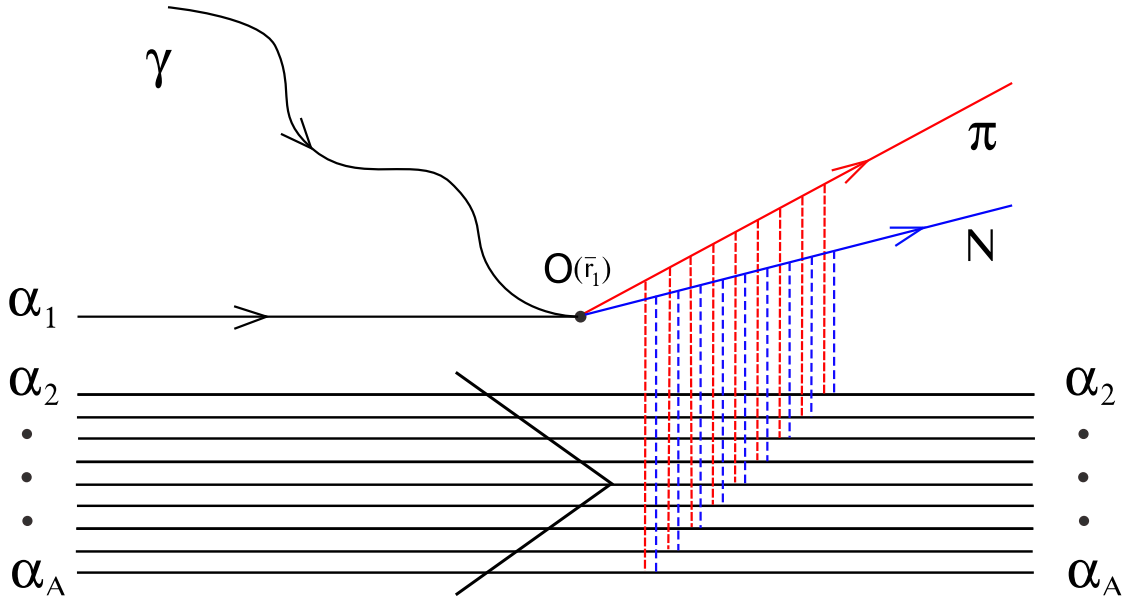

Figure 2.2 Diagram included in computing the matrix element of Eq. (2.9). The dotted lines denote the FSI of the ejected pion (red) and nucleon (blue) with the spectator residual nucleons. The diagram shown here is representative for the spectator approximation: one active nucleon N and π are subject to soft collisions with frozen spectator nucleons that occupy the single-particle levels $\alpha_2, \alpha_3, \ldots, \alpha_A$ and are not subject to changes in their quantum numbers.

In what follows, we assume that the pion production operator acts on a bound-state wave function as a scalar (factorization assumption): $O_\mu(\vec{r})\phi_{\alpha_1}(\vec{r}) \equiv \mathscr{C}_\mu \phi_{\alpha_1}(\vec{r})$. With

$$\phi^D_{\alpha_1}(\vec{p}) = \int d\vec{r} e^{-i\vec{p}\cdot\vec{r}} \phi_{\alpha_1}(\vec{r}) \mathscr{F}^{\,\mathrm{FSI}}(\vec{r}), \tag{2.14}$$

we can write

$$\mathscr{M}^{(\gamma,N\pi)}_{fi} \approx u^\dagger(\vec{p}_N, m_s)\epsilon^\mu(\lambda)\mathscr{C}_\mu \phi^D_{\alpha_1}(\vec{p}_m). \tag{2.15}$$

When studying nuclear transparencies, it is convenient to factorize the invariant matrix element in such a manner that it becomes a convolution of a factor describing the elementary pion photoproduction process and a factor modeling the combined effect of all FSI mechanisms of the outgoing hadrons. In order to arrive at such a factorized form for the cross section, we relate the $\gamma + A \to (A-1) + N + \pi$ matrix element in Eq. (2.15) to the one for for free nucleons $\gamma + N_i \to N + \pi$

$$\left(\mathscr{M}^{(\gamma,N\pi)}_{fi\,\mathrm{free}}\right)_{m_s,m'_s} = u^\dagger(\vec{p}_N, m_s)\epsilon^\mu(\lambda)\mathscr{C}_\mu u(\vec{p}_m, m_{s'}), \tag{2.16}$$

with $m_{s'}$ the spin of the initial nucleon. First, we consider the situation with vanishing FSI, second the more realistic case with inclusion of a FSI phase operator. When ignoring FSI, the wave functions for the ejected hadrons reduce to plane waves and $\mathscr{F}_{\mathrm{FSI}}(\vec{r}) \equiv 1$,

$\phi^D_{\alpha_1}(\vec{p}_m) \equiv \phi_{\alpha_1}(\vec{p}_m)$. After substituting in Eq. (2.15) the completeness relation for Dirac spinors:

$$\sum_{m'_s} \left[u(\vec{p}_m, m'_s)\bar{u}(\vec{p}_m, m'_s) - v(\vec{p}_m, m'_s)\bar{v}(\vec{p}_m, m'_s) \right] = \mathbb{1}_{4\times 4}\,, \tag{2.17}$$

one obtains

$$\left(\mathscr{M}^{(\gamma,N\pi)}_{fi}\right)_{\text{RPWIA}} = \sum_{m'_s} \left(\mathscr{M}^{(\gamma,N\pi)}_{fi\,\text{free}}\right)_{m_s,m'_s} \bar{u}(\vec{p}_m, m'_s)\phi_{\alpha_1}(\vec{p}_m) \\ - \text{negative energy terms}\,, \tag{2.18}$$

where RPWIA stands for the relativistic plane-wave impulse approximation. From this last expression it is clear that even with vanishing FSI the presence of negative-energy components makes factorization impossible. The contraction of the Dirac spinors $\bar{u}$ and $\bar{v}$ with the bound nucleon wave function ϕ_{α_1} is given by

$$\bar{u}(\vec{p}_m, m'_s)\phi_{\alpha_1}(\vec{p}_m) = (2\pi)^{3/2}(-i)^l \sqrt{\frac{E_{N_i}(p_m) + m_{N_i}}{2m_{N_i}}}\alpha_{n\kappa}(p_m)\chi^\dagger_{\frac{1}{2},m'_s}\mathscr{Y}_{\kappa m}(\Omega_p, \vec{\sigma})\,, \tag{2.19}$$

$$\bar{v}(\vec{p}_m, m'_s)\phi_{\alpha_1}(\vec{p}_m) = (2\pi)^{3/2}(-i)^l \sqrt{\frac{E_{N_i}(p_m) + m_{N_i}}{2m_{N_i}}}\beta_{n\kappa}(p_m)\chi^\dagger_{\frac{1}{2},m'_s}\mathscr{Y}_{-\kappa m}(\Omega_p, \vec{\sigma})\,, \tag{2.20}$$

where m_{N_i} is the free nucleon mass, $E_{N_i}(p_m) = \sqrt{m^2_{N_i} + p^2_m}$ and

$$\alpha_{n\kappa}(p_m) = \frac{E_{N_i} + m_{N_i}}{2m_{N_i}}\left(g_{n\kappa}(p_m) - \frac{p_m}{E_{N_i} + m_{N_i}}\frac{\kappa}{|\kappa|}f_{n\kappa}(p_m)\right)\,, \tag{2.21}$$

$$\beta_{n\kappa}(p_m) = \frac{E_{N_i} + m_{N_i}}{2m_{N_i}}\left(\frac{p_m}{E_{N_i} + m_{N_i}}g_{n\kappa}(p_m) - \frac{\kappa}{|\kappa|}f_{n\kappa}(p_m)\right)\,, \tag{2.22}$$

with $g_{n\kappa}(p_m)$ and $f_{n\kappa}(p_m)$ defined as in Eqs. (B.4) and (B.5). From Eqs. (2.19) and (2.20), one observes the positive-, negative-, and crossterm-energy contributions to the cross section. They are proportional to $|\alpha_{n\kappa}(p_m)|^2$, $|\beta_{n\kappa}(p_m)|^2$ and $2\alpha_{n\kappa}(p_m)\beta_{n\kappa}(p_m)$ respectively. In Fig. 2.3 we have plotted these three contributions for the two proton shells in ^{12}C. For the $1p3/2$ shell the positive energy projections are about an order of a magnitude larger than the cross term and more than two orders than the negative energy projections. The difference, however, becomes smaller for high momenta. For the $1s1/2$ shell, similar features emerge for momenta smaller than 300 MeV/c. At higher momenta, however, the situation changes and the negative-energy components start playing an important role. For the calculations in this work, we deal with integrations over phase space with a missing

momentum cut off at 300 MeV/c. Accordingly, we deem it a reasonable approximation to neglect the negative energy contributions in Eq. (2.18):

$$\left(\mathcal{M}_{fi}^{(\gamma,N\pi)}\right)_{\text{RPWIA}} \approx \sum_{m_s'} \left(\mathcal{M}_{fi\,\text{free}}^{(\gamma,N\pi)}\right)_{m_s,m_s'} \bar{u}(\vec{p}_m, m_s')\phi_{\alpha_1}(\vec{p}_m)\,, \tag{2.23}$$

and $\alpha_{n\kappa}(p_m)$ reduces to

$$\alpha_{n\kappa}(p_m) \approx \frac{2m_{N_i}}{E_{N_i}+m_{N_i}} g_{n\kappa}(p_m)\,. \tag{2.24}$$

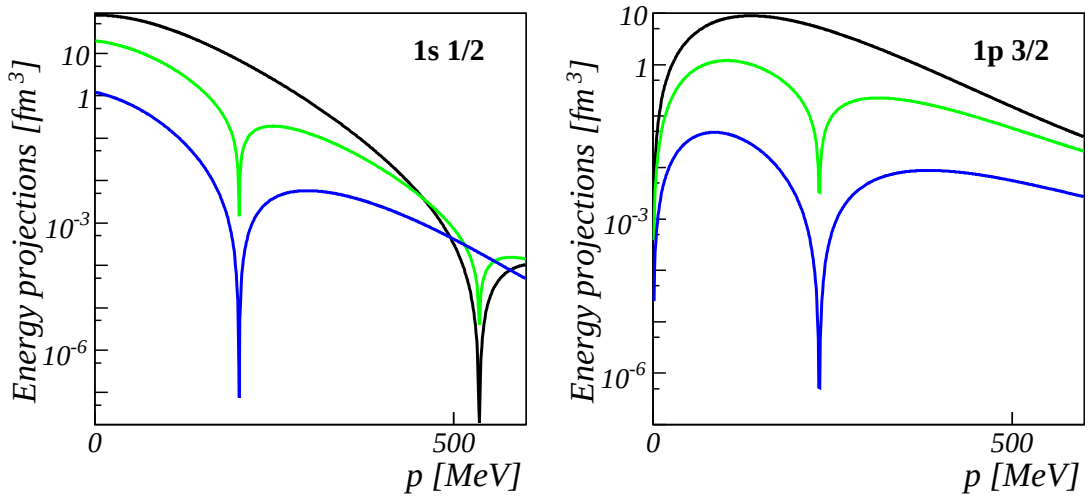

Figure 2.3 Contributions of the different energy projections to the momentum distribution for the $1s1/2$ (left panel) and $1p3/2$ (right panel) in ^{12}C. The black curve denotes $|\alpha_{n\kappa}(p_m)|^2$) (proportional to the positive-energy projection, the blue curve $|\alpha_{n\kappa}(p_m)|^2$ (proportional to the negative-energy projections, and the green curve $2|\alpha_{n\kappa}(p_m)\beta_{n\kappa}(p_m)|$ (proportional to the cross terms).

After squaring the matrix element and summing over the quantum number m of the bound nucleon wave function, one can use the following property of the spin spherical harmonics $\mathcal{Y}_{\kappa m}$ [82]

$$\sum_m \mathcal{Y}_{\kappa m}(\Omega_p,\vec{\sigma})\mathcal{Y}^{\dagger}_{\kappa m}(\Omega_p,\vec{\sigma}) = \frac{(2j+1)}{8\pi}\mathbb{1}_{2\times 2}\,. \tag{2.25}$$

Finally, by using $\chi^{\dagger}_{\frac{1}{2},m_s}\chi_{\frac{1}{2},m_s'} = \delta_{m_s m_s'}$, the free pion production process can be formally decoupled from the typical nuclear effects:

$$\overline{\sum_{fi}}|\mathcal{M}_{fi}^{(\gamma,N\pi)}|^2 = \frac{1}{2}\sum_{\lambda,m,m_s}|\mathcal{M}_{fi}^{(\gamma,N\pi)}|^2 \approx (2\pi)^3\frac{2j+1}{4\pi}\frac{E_{N_i}(p_m)+m_{N_i}}{2m_{N_i}}|\alpha_{n\kappa}(p_m)|^2$$
$$\times\frac{1}{4}\sum_{\lambda,m_s,m_s'}|\left(\mathcal{M}_{fi\,\text{free}}^{(\gamma,N\pi)}\right)_{m_s,m_s'}|^2\,. \tag{2.26}$$

The right-hand side of the above equation requires knowledge about the off-shell extrapolation of the pion photoproduction amplitude. For the on-shell situation, the matrix element for the pion photoproduction process can be linked to the cross section

$$\frac{1}{4}\sum_{\lambda,m_s,m_s'} |\left(\mathscr{M}_{fi\,\text{free}}^{(\gamma,N\pi)}\right)_{m_s,m_s'}|^2 \approx \frac{4\pi(s-m_{N_i}^2)^2}{m_{N_i}m_N}\frac{d\sigma^{\gamma\pi}}{d|t|}, \tag{2.27}$$

with $s=(p_N^\mu+p_\pi^\mu)^2$ and $t=(q^\mu-p_\pi^\mu)^2$ the Mandelstam variables of the free process. The off-shell extrapolation of Eq. (2.27) involves a correction due to the Fermi motion and the binding of the nucleon on which the photon is absorbed. This can be done in several different ways and it is not yet clear which of them are the most efficient and reliable. In this work, we consider photon energies ≥ 1.5 GeV that make off-shell corrections to s relatively small for typical nucleon momenta. For this reason, we deem it a reasonable approximation to adopt the Eq. (2.27) for sufficiently high photon energies. After substituting Eqs. (2.26) and (2.27) in Eq. (2.1), the differential cross section for $\gamma+A\rightarrow(A-1)+N+\pi$ in the RPWIA reads

$$\left(\frac{d^5\sigma}{dE_\pi d\Omega_\pi d\Omega_N}\right)_{RPWIA} \approx \frac{M_{A-1}p_\pi p_N(s-m_{N_i}^2)^2}{4\pi m_{N_i}qE_A} f_{rec}^{-1} \times \frac{2j+1}{4\pi}\frac{\left[E_{N_i}(p_m)+m_{N_i}\right]}{2m_{N_i}}|\alpha_{n\kappa}(p_m)|^2\frac{d\sigma^{\gamma\pi}}{d|t|}. \tag{2.28}$$

When FSI are included, the above derivation is no longer possible due to the presence of $\mathscr{F}_{\text{FSI}}(\vec{r})$ in ϕ_α^D. We define a distorted momentum distribution along the lines of Ref. [83]

$$\rho_D(\vec{p}_m)=\frac{1}{(2\pi)^3}\sum_{m_s,m}|\bar{u}(\vec{p}_m,m_s)\phi_{\alpha_1}^D(\vec{p}_m)|^2. \tag{2.29}$$

When FSI and negative-energy contributions to $\phi_{\alpha_1}^D$ are neglected, Eq. (2.29) reduces to $\frac{2j+1}{4\pi}\frac{E_{N_i}(p_m)+m_{N_i}}{2m_{N_i}}|\alpha_{n\kappa}(p_m)|^2$. Based on this analogy, we write the differential cross section with FSI as

$$\left(\frac{d^5\sigma}{dE_\pi d\Omega_\pi d\Omega_N}\right)_D \approx \frac{M_{A-1}p_\pi p_N(s-m_{N_i}^2)^2}{4\pi m_{N_i}qE_A} f_{rec}^{-1}\rho_D(\vec{p}_m)\frac{d\sigma^{\gamma\pi}}{d|t|}. \tag{2.30}$$

2.1.2 Pion Electroproduction: The $A(e,e'\pi N)$ Cross Section

We use the same conventions and notations as in subsec. 2.1.1 in the derivation of the pion electroproduction cross section. The four-momentum of the virtual photon γ^* is $q^\mu(\omega,\vec{q})$ and the z axis lies along $\vec{q}$. The incoming [scattered] electron has four-momentum

$p_e^\mu(E_e,\vec{p}_e)$ $[p_{e'}^\mu(E_{e'},\vec{p}_{e'})]$ and spin s $[s']$, θ_e denotes the electron scattering angle. With these additional notations and conventions, the differential cross section in the laboratory frame reads [76]

$$\frac{d^8\sigma}{d\Omega_{e'}dE_{e'}dE_\pi d\Omega_\pi d\Omega_N} = \frac{m_e^2 p_{e'}}{(2\pi)^3 p_e}\frac{M_{A-1}m_N p_\pi p_N}{2(2\pi)^5 E_A} f_{rec}^{-1}\overline{\sum_{fi}}\left|\mathscr{M}_{fi}^{(e,e'N\pi)}\right|^2, \tag{2.31}$$

with the recoil factor f_{rec} as in Eq. (2.2) and $\overline{\sum}_{fi}$ representing the averaging over initial electron spins and summing over the spins of the final particles. The invariant matrix element $\mathscr{M}_{fi}^{(e,e'N\pi)}$ can be written as

$$\mathscr{M}_{fi}^{(e,e'N\pi)} = \langle P_\pi^\mu, P_N^\mu m_s, P_{A-1}^\mu J_R M_R | j_\mu \frac{e}{Q^2} J^\mu | P_A^\mu 0^+\rangle, \tag{2.32}$$

with the electron current

$$j_\mu = \bar{u}(\vec{p}_{e'},s')\gamma_\mu u(\vec{p}_e,s), \tag{2.33}$$

$Q^2 = -q_\mu q^\mu$ and the hadron current J^μ. By defining an auxiliary current

$$a_\mu \equiv j_\mu - \frac{j_0}{\omega}q_\mu \tag{2.34}$$

and using current conservation, the following identity can readily be proved:

$$j_\mu J^\mu = -a_i J_i = -a_i\delta_{ij}J_j = -\sum_{\lambda=(x,y,z)} a_i e_i(\lambda)e_j(\lambda)J_j, \tag{2.35}$$

where $\vec{e}(\lambda)$ is the unit vector along the axis $\lambda = (x,y,z)$. After defining the electron density matrix

$$\rho_{\lambda\lambda'} = \sum_{ss'}\left[\vec{e}(\lambda)\cdot\vec{a}\right]^\dagger\left[\vec{e}(\lambda')\cdot\vec{a}\right] \tag{2.36}$$

and the hadronic matrix elements

$$w_\lambda = \langle P_\pi^\mu, P_N^\mu m_s, P_{A-1}^\mu J_R M_R | \vec{e}(\lambda)\cdot\vec{J} | P_A^\mu 0^+\rangle, \tag{2.37}$$

we can write for the matrix element

$$\sum_{ss'}\left|\mathscr{M}_{fi}^{(e,e'N\pi)}\right|^2 = \frac{e^2}{Q^4}\sum_{\lambda\lambda'} w_\lambda^\dagger \rho_{\lambda\lambda'} w_{\lambda'}. \tag{2.38}$$

With the degree of transverse polarization defined as

$$\epsilon = \left(1 + \frac{2q^2}{Q^2}\tan^2\frac{\theta_e}{2}\right)^{-1}, \tag{2.39}$$

the electron density matrix becomes [84]

$$\rho_{\lambda\lambda'} = \frac{Q^2}{m_e^2}\frac{1}{1-\epsilon}\begin{pmatrix} \frac{1}{2}(1+\epsilon) & 0 & -\frac{1}{2}\sqrt{2\frac{Q^2}{\omega^2}\epsilon(1+\epsilon)} \\ 0 & \frac{1}{2}(1-\epsilon) & 0 \\ -\frac{1}{2}\sqrt{2\frac{Q^2}{\omega^2}\epsilon(1+\epsilon)} & 0 & \frac{Q^2}{\omega^2}\epsilon \end{pmatrix}. \tag{2.40}$$

After substituting Eq. (2.40) in Eq. (2.38), one can factor out a part containing all the variables related to the electrons in the differential cross section:

$$\frac{d^8\sigma}{d\Omega_{e'}dE_{e'}dE_\pi d\Omega_\pi d\Omega_N} = \Gamma\frac{d^5\sigma_v}{dE_\pi d\Omega_\pi d\Omega_N} \equiv \Gamma\mathscr{D}\overline{\sum}_{fi}|M_{fi}^{(\gamma^*,N\pi)}|^2. \tag{2.41}$$

Here, $\mathscr{M}_{fi}^{(\gamma^*,N\pi)} = \langle P_\pi^\mu, P_N^\mu m_s, P_{A-1}^\mu J_R M_R|\hat{\mathcal{O}}|q^\mu, P_A^\mu 0^+\rangle$, $\mathscr{D} = \frac{M_{A-1}m_N p_\pi p_N}{4(2\pi)^5 E_\gamma^* E_A} f_{\text{rec}}^{-1}$ and $\Gamma = \frac{\alpha}{2\pi^2}\frac{E_{e'}}{E_e}\frac{E_\gamma^*}{Q^2}\frac{1}{1-\epsilon}$ is the electron flux factor, with the virtual photon equivalent energy $E_\gamma^* = \frac{s-M_A^2}{2M_A}$, the fine-structure constant α, and $s = (q^\mu + P_A^\mu)^2$ one of the Mandelstam variables of the virtual photoproduction process. The five-fold differential cross section of Eq. (2.41) can be cast in the following form

$$\begin{aligned}\frac{d^5\sigma_v}{dE_\pi d\Omega_\pi d\Omega_N} \equiv \frac{d^5\sigma_T}{dE_\pi d\Omega_\pi d\Omega_N} + \epsilon\frac{d^5\sigma_L}{dE_\pi d\Omega_\pi d\Omega_N} \\ + \epsilon\frac{d^5\sigma_{TT}}{dE_\pi d\Omega_\pi d\Omega_N} + \sqrt{\epsilon(\epsilon+1)}\frac{d^5\sigma_{TL}}{dE_\pi d\Omega_\pi d\Omega_N},\end{aligned} \tag{2.42}$$

with

$$\begin{aligned}\frac{d^5\sigma_T}{dE_\pi d\Omega_\pi d\Omega_N} &= \frac{\mathscr{D}}{2}\sum_{m_s M_R}\left[|J_x|^2 + |J_y|^2\right], \\ \frac{d^5\sigma_L}{dE_\pi d\Omega_\pi d\Omega_N} &= \mathscr{D}\frac{Q^2}{\omega^2}\sum_{m_s M_R}|J_z|^2, \\ \frac{d^5\sigma_{TT}}{dE_\pi d\Omega_\pi d\Omega_N} &= \frac{\mathscr{D}}{2}\sum_{m_s M_R}\left[|J_x|^2 - |J_y|^2\right], \\ \frac{d^5\sigma_{TL}}{dE_\pi d\Omega_\pi d\Omega_N} &= -\frac{\mathscr{D}}{2}\sqrt{\frac{2Q^2}{\omega^2}}\sum_{m_s M_R}\left[J_x^* J_z + J_z^* J_x\right].\end{aligned} \tag{2.43}$$

As for the photoproduction case, we wish to establish a relation between the invariant matrix element for virtual-photon pion production on a nucleus ($\mathscr{M}_{fi}^{(\gamma^*,N\pi)}$) and on a free nucleon ($\mathscr{M}_{fi,\text{free}}^{(\gamma^*,N\pi)}$). In comparison with the real photoproduction process, the virtual photon has an extra degree of polarization and $Q^2 \neq 0$. This does not alter the derivation presented in the previous subsection and after neglecting negative energy contributions, one arrives at

$$\mathscr{M}_{fi}^{(\gamma^*,N\pi)} \approx \sum_{m_{s'}}(\mathscr{M}_{fi,\text{free}}^{(\gamma^*,N\pi)})_{\lambda,m_s,m_{s'}}\bar{u}(\vec{p}_m, m_{s'})\phi_\alpha^D(\vec{p}_m). \tag{2.44}$$

The matrix element $\mathscr{M}_{fi,\text{free}}^{(\gamma^*,N\pi)}$ is related to the free electroproduction process by

$$\frac{d^5\sigma^{eN}}{dE_{e'}d\Omega_{e'}d\phi_\pi^* d|t'|} = \Gamma' \frac{m_N^2}{2(2\pi)^2(s'-m_N^2)^2}\overline{\sum}_{fi}|\mathscr{M}_{fi,\text{free}}^{(\gamma^*,N\pi)}|^2, \tag{2.45}$$

where $\Gamma' = \frac{\alpha}{2\pi^2}\frac{E_{e'}}{E_e}\frac{K}{Q^2}\frac{1}{1-\epsilon}$ is the electron flux factor, with the virtual photon equivalent energy $K = \frac{s'-m_N^2}{2m_N}$. Further, $s' = (p_N^\mu + p_\pi^\mu)^2$ and $t' = (q^\mu - p_\pi^\mu)^2$ are the Mandelstam variables for the free process. Starred variables denote center-of-mass values.

With ρ_D defined in Eq. (2.29) and by making use of Eqs. (2.44) and (2.45), we arrive at the factorized form for the differential $A(e,e'N\pi)$ cross section:

$$\left(\frac{d^8\sigma}{d\Omega_{e'}dE_{e'}dE_\pi d\Omega_\pi d\Omega_N}\right)_\text{D} = \frac{\Gamma}{\Gamma'}\frac{M_{A-1}p_N p_\pi (s'-m_N^2)^2}{2m_N E_\gamma E_A} f_{rec}^{-1}\rho_\text{D}\frac{d^5\sigma^{eN}}{dE_{e'}d\Omega_{e'}d|t|d\phi_\pi^*}. \tag{2.46}$$

We wish to stress that the assumptions made to arrive at this expression, are essentially identical to those made for the real photon case discussed in the previous section.

2.1.3 Two-nucleon Knockout: The $A(\gamma,N_1N_2)$ Cross Section

The two ejected nucleons N_1 and N_2 have four-momentum $K_i^\mu(E_{k_i},\vec{k}_i)$, mass m_{N_i} and spin m_{s_i}, with $i=1,2$. The four-momentum of the residual nucleus is $P_{A-2}^\mu(E_{A-2},\vec{p}_{A-2})$ and it has quantum numbers J_R, M_R and mass M_{A-2}. Missing momentum is defined as $\vec{P}_m = \vec{k}_1+\vec{k}_2-\vec{q}$. The fivefold differential cross section reads

$$\frac{d^5\sigma}{dE_{k_1}d\Omega_{N_1}d\Omega_{N_2}} = \frac{M_{A-2}m_{N_1}m_{N_2}k_1k_2}{2(2\pi)^5 qE_A} f_\text{rec}'^{-1}\overline{\sum_{if}}|\mathscr{M}_{if}^{(\gamma,N_1N_2)}|^2, \tag{2.47}$$

with the recoil factor f_rec' and invariant matrix element $\mathscr{M}_{if}^{(\gamma,N_1N_2)}$ given by

$$f_{rec}' = \frac{E_{A-2}}{E_A}\left|1+\frac{E_{k_2}}{E_{A-2}}\left(1+\frac{(\vec{k}_1-\vec{q})\cdot\vec{k}_2}{k_2^2}\right)\right|, \tag{2.48}$$

$$\mathscr{M}_{if}^{(\gamma,N_1N_2)} = \langle K_1^\mu m_{s_1}, K_2^\mu m_{s_2}, P_{A-2}^\mu J_R M_R|\hat{\mathscr{O}}|q^\mu, P_A^\mu 0^+\rangle. \tag{2.49}$$

The wave functions of the ejected nucleons are written as

$$|k_1^\mu m_{s_1}\rangle \equiv \Psi_{\vec{k}_1,m_{s_1}}^{(+)}(\vec{r}_j) = \hat{\mathscr{S}}_{K_1N}^\dagger(\vec{r}_j;\vec{r}_1,\ldots,\vec{r}_{m\neq j,k},\ldots,\vec{r}_A)u(\vec{k}_1,m_{s_1})e^{i\vec{k}_1\cdot\vec{r}_j} \tag{2.50}$$

$$|k_2^\mu m_{s_2}\rangle \equiv \Psi_{\vec{k}_2,m_{s_2}}^{(+)}(\vec{r}_k) = \hat{\mathscr{S}}_{K_2N}^\dagger(\vec{r}_k;\vec{r}_1,\ldots,\vec{r}_{m\neq k,j},\ldots,\vec{r}_A)u(\vec{k}_2,m_{s_2})e^{i\vec{k}_2\cdot\vec{r}_k}, \tag{2.51}$$

with $\hat{\mathscr{S}}_{K_iN}$ an operator that accounts for the FSI with the residual nucleons. The FSI between the two ejected nucleons is not included in the above approach. We neglect these FSI, as the

kinematics in the experiments we compare to are chosen so that the two ejected nucleons move back-to-back in the c.m. frame. The final A-nucleon wave function is constructed by antisymmetrizing $\Psi^{(+)}_{\vec{k}_1,m_{s_1}}$ and $\Psi^{(+)}_{\vec{k}_2,m_{s_2}}$ with the wave function for the residual nucleus Ψ^{J_R,m_R}_{A-2}:

$$|K_1^\mu m_{s_1}, K_2^\mu m_{s_2}, P^\mu_{A-2} J_R M_R\rangle \equiv \Psi_A^{\vec{k}_1 m_{s_1}, \vec{k}_2 m_{s_2}}(\vec{r}_1,\ldots,\vec{r}_A) = \hat{\mathscr{A}}\left[\hat{\mathscr{S}}^\dagger_{K_1N}(\vec{r}_1;\vec{r}_3,\ldots,\vec{r}_A)u(\vec{k}_1,m_{s_1})e^{i\vec{k}_1\cdot\vec{r}_1} \times \hat{\mathscr{S}}^\dagger_{K_2N}(\vec{r}_2;\vec{r}_3,\ldots,\vec{r}_A)u(\vec{k}_2,m_{s_2})e^{i\vec{k}_2\cdot\vec{r}_2}\Psi^{J_R,m_R}_{A-2}(\vec{r}_3,\ldots,\vec{r}_A)\right] . \quad (2.52)$$

The wave function of the impinging photon is again as in Eq. (2.5).

Knockout of a correlated pair

First we describe the one-step reaction process of Fig. 2.4 in which the photon interacts directly with a correlated pair. The two nucleons form a high density region in the nucleus, with high relative momentum and a small distance separating them. By interacting with one of the nucleons, the photon breaks up the pair. Due to the high relative momentum, the second nucleon can also be ejected from the nucleus and detected if the kinematics is carefully tuned.

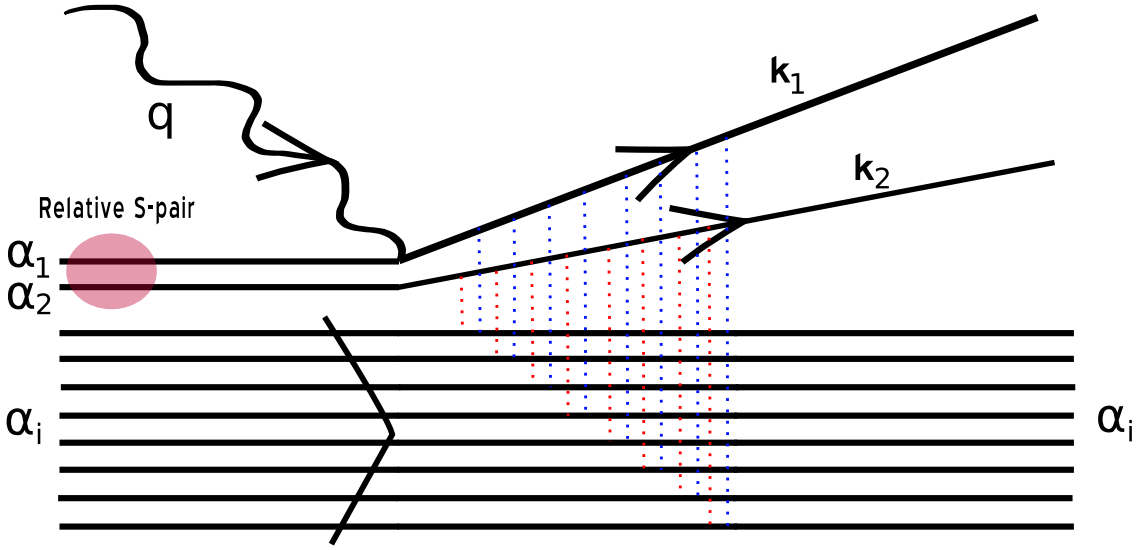

Figure 2.4 Diagram depicting the $A(\gamma, N_1N_2)$ reaction as the breakup of a correlated nucleon-nucleon pair. The photon interacts in a one-step process with one of the nucleons in the correlated pair and the two nucleons are subsequently ejected out of the nucleus. The dotted red and blue lines represent the FSI with the residual spectator nucleons.

After using the antisymmetrization of the incoming and outgoing wave functions and assuming spin independent, elastic and mildly inelastic FSI, we can write the invariant matrix element in lowest order as (with α_1 and α_2 the quantum numbers of the two nucleons

forming the initial pair):

$$\mathscr{M}_{if,\text{pair}}^{(\gamma,N_1N_2)} \approx \int d\vec{r} \int d\vec{r}_1 \int d\vec{r}_2 \left(u^\dagger(\vec{k}_1, m_{s_1}) u^\dagger(\vec{k}_2, m_{s_2}) e^{-i\vec{k}_1\cdot\vec{r}_1} e^{-i\vec{k}_2\cdot\vec{r}_2} - u^\dagger(\vec{k}_2, m_{s_2}) u^\dagger(\vec{k}_1, m_{s_1}) e^{-i\vec{k}_2\cdot\vec{r}_1} e^{-i\vec{k}_1\cdot\vec{r}_2} \right) (\delta(\vec{r}-\vec{r}_1) + \delta(\vec{r}-\vec{r}_2)) \times e^{i\vec{q}\cdot\vec{r}} \epsilon^\mu(\lambda) \gamma^0 J_\mu(\vec{r}) \phi_{\alpha_1}(\vec{r}_1) \phi_{\alpha_2}(\vec{r}_2) \mathscr{F}_{\text{FSI}}(\vec{r}_1, \vec{r}_2). \quad (2.53)$$

Here, J^μ represents the electromagnetic coupling of the photon to a bound nucleon, and the FSI factor $\mathscr{F}_{\text{FSI}}(\vec{r}_1, \vec{r}_2)$ is defined as

$$\mathscr{F}_{\text{FSI}}(\vec{r}_1, \vec{r}_2) = \int d\vec{r}_3 \ldots \int d\vec{r}_A |\phi_{\alpha_3}(\vec{r}_3)|^2 \ldots |\phi_{\alpha_A}(\vec{r}_A)|^2 \times \hat{\mathscr{S}}_{K_1N}(\vec{r}_1; \vec{r}_3, \ldots, \vec{r}_A) \hat{\mathscr{S}}_{K_2N}(\vec{r}_2; \vec{r}_3, \ldots, \vec{r}_A). \quad (2.54)$$

We now introduce the c.m. and relative coordinates ($\vec{R} = \frac{\vec{r}_1+\vec{r}_2}{2}$, $\vec{r}_{12} = \vec{r}_1 - \vec{r}_2$) of the pair and assume

$$\mathscr{F}_{\text{FSI}}(\vec{R} + \frac{\vec{r}_{12}}{2}, \vec{R} - \frac{\vec{r}_{12}}{2}) \approx \mathscr{F}_{\text{FSI}}(\vec{R}, \vec{R}) \equiv \mathscr{F}_{\text{FSI}}(\vec{R}) \quad (2.55)$$

$$\phi_{\alpha_1}(\vec{R} + \frac{\vec{r}_{12}}{2}) \phi_{\alpha_2}(\vec{R} - \frac{\vec{r}_{12}}{2}) \approx \phi_{\alpha_1}(\vec{R}) \phi_{\alpha_2}(\vec{R}) \quad (2.56)$$

$$J_\mu(\vec{R} \pm \frac{\vec{r}_{12}}{2}) \approx \Xi_\mu(\vec{R}) g(\vec{r}_{12}) \approx \Xi_\mu g(\vec{r}_{12}). \quad (2.57)$$

In Eq. (2.57) we have factorized the photon-pair coupling into a product of the photon-nucleon coupling and a correlation function. As we have set $\vec{r}_{12} \approx 0$, Eq. (2.56) requires that the two correlated nucleons reside in a relative S state [85]. This is a reasonable approximation as investigations of the ^{16}O$(e, e'pp)$ reaction at the electron accelerators in Mainz [86, 87] and Amsterdam [88–90] have clearly shown that pairs of protons are solely subject to short-range correlations when they reside in a relative S state under conditions corresponding with relatively small c.m. momenta P (or, the initial protons are very close and moving back-to-back).

For the transition to the ^{14}C ground state in the ^{16}O$(e, e'pp)$ reaction, the $L = 0$ component of the c.m. motion of the pair is associated with a relative ^1S wave function. For transitions to the ground state and 1^+ excitation, the $L = 1$ component is associated with a relative ^1P wave function. Consequently, one can determine the quantum numbers of the relative wave function of the pair from the p_m (which is equal to the pair c.m. momentum in the plane-wave limit) dependence of the differential cross section. In Fig. 2.5, data from MAMI [87] and calculations by the Ghent group [86] for these transitions are shown. Calculations for the reaction whereby the final nucleus is create d in the 1^+ state show the

dominance of the two-body currents for a P-wave pair, while the one-body currents associated with SRC contribute only marginally. For the transition to the ground state, the c.m. momentum dependence shows the dominance of relative S-pairs for low c.m. momenta. The one-body currents clearly form the biggest contribution for these S-pairs. At higher c.m. momenta, the relative P-pairs dominate, and two-body currents form the dominating contribution. In Fig. 2.6, data for the ground state transition measured at NIKHEF [90] and calculations in the Ghent [91] and Pavia [92] model are shown that confirm these findings.

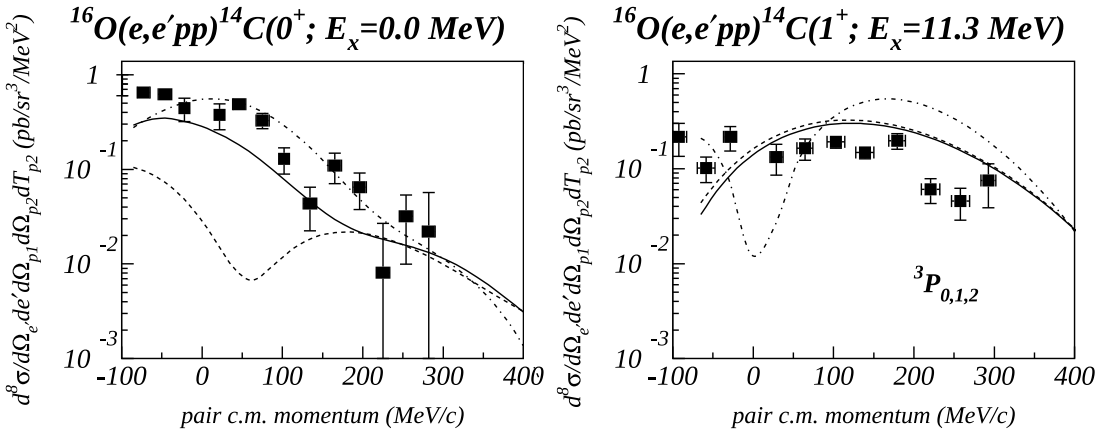

Figure 2.5 Cross section for transition to the ground state (left panel) and 1^+ excitation (right panel) of ^{14}C as a function of missing pair momentum, for the reaction $^{16}\mathrm{O}(e,e'pp)$. In the left panel, the dashed curve shows the results of a distorted-wave calculation with only two-body currents. The solid (dot-dashed) curve is the result of a distorted-wave (plane-wave) calculation that includes both one- and two-body currents. In the left panel, the dashed curve shows a calculation that only includes two-body currents. The solid (dot-dashed) curve shows a distorted-wave (plain-wave) calculation that accounts for both one- and two-body currents. Data from [87]. Figure taken from Ref. [86].

After defining

$$\eta^D_{\alpha_1,\alpha_2}(\vec{P}) = \int d\vec{R} e^{-i\vec{P}\cdot\vec{R}} \mathscr{F}_{\mathrm{FSI}}(\vec{R}) \phi_{\alpha_1}(\vec{R}) \phi_{\alpha_2}(\vec{R}) \tag{2.58}$$

$$g(\vec{p}) = \int d\vec{r} e^{-i\vec{p}\cdot\vec{r}} g(\vec{r}), \tag{2.59}$$

we can write the matrix element as

$$\begin{aligned} \mathscr{M}^{(\gamma,N_1N_2)}_{if,\mathrm{pair}} \approx & \left(u^\dagger(\vec{k}_1,m_{s_1})u^\dagger(\vec{k}_2,m_{s_2}) - u^\dagger(\vec{k}_2,m_{s_2})u^\dagger(\vec{k}_1,m_{s_1})\right) \\ & \times \left(g(\frac{\vec{k}_1-\vec{k}_2-\vec{q}}{2})\gamma^0 \Xi^{\alpha_1}_\mu + g(\frac{\vec{k}_1-\vec{k}_2+\vec{q}}{2})\gamma^0 \Xi^{\alpha_2}_\mu \right) \epsilon^\mu(\lambda) \eta^D_{\alpha_1,\alpha_2}(\vec{P}_m). \end{aligned} \tag{2.60}$$

The superscript α_i in $\Xi^{\alpha_i}_\mu$ denotes the quantum numbers of the nucleon that absorbs the photon. After the choice of the appropriate Ξ_μ and $g(\vec{r})$ functions we have all the ingredients to compute Eq. (2.60) readily available. For Ξ^μ, we use the CC2 form of Ref. [93] and

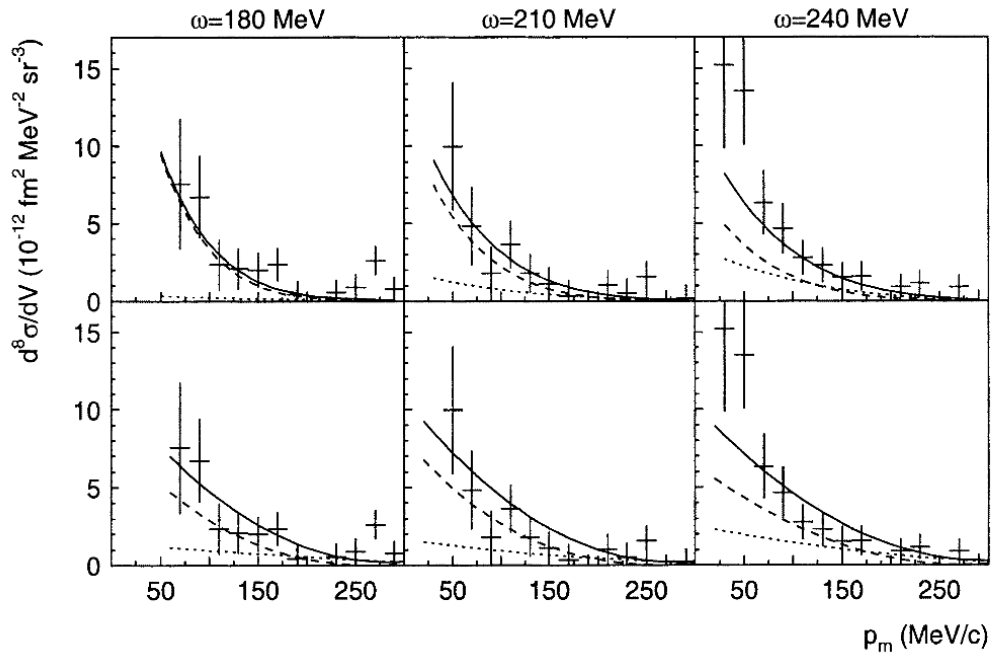

Figure 2.6 Cross sections for the transition to the ground state of ^{14}C as a function of the missing pair momentum, for the reaction ^{16}O$(e,e'pp)$ at three values of ω. Curves are obtained in the Pavia model (top) [92] and Ghent model (bottom panels) [91]. Solid curves include one- and two-body currents. Dashed (dotted) curves represent the contribution of one-body (two-body) currents. Figure taken from Ref. [90].

we impose the Coulomb gauge. For $g(r)$, the correlation function of Ref. [94] is used. The motivation of this choice will be presented in subsec 2.4.

Hard Rescattering Process

Besides the direct knockout of a correlated pair discussed above, the $A(\gamma,N_1N_2)$ process receives contributions from a two-step reaction mechanism sketched in Fig. 2.7. A nucleon obtains high momentum by absorption of the photon and propagates through the nucleus. On its way out of the nucleus a hard rescattering with one of the residual nucleons occurs (besides the soft FSI) and the two nucleons are both ejected from the nucleus. We employ the same notations as in the previous subsections. In addition, we define the nucleon propagator in the medium whereby we account for soft FSI mechanisms

$$D^D_{\mathcal{N}}(\vec{r}_0-\vec{r}_j)=\hat{\mathscr{S}}_{\mathcal{N}N}(\vec{r}_j,\vec{r}_0;\vec{r}_1,\ldots,\vec{r}_{m\neq j,k},\ldots,\vec{r}_A)D_N(\vec{r}_0-\vec{r}_j)\,, \tag{2.61}$$

and a two-body operator describing the hard rescattering process

$$\mathscr{O}^{(2)}=\sum_{k\neq j}\hat{O}(\vec{r}_0,\vec{r}_k)\,. \tag{2.62}$$

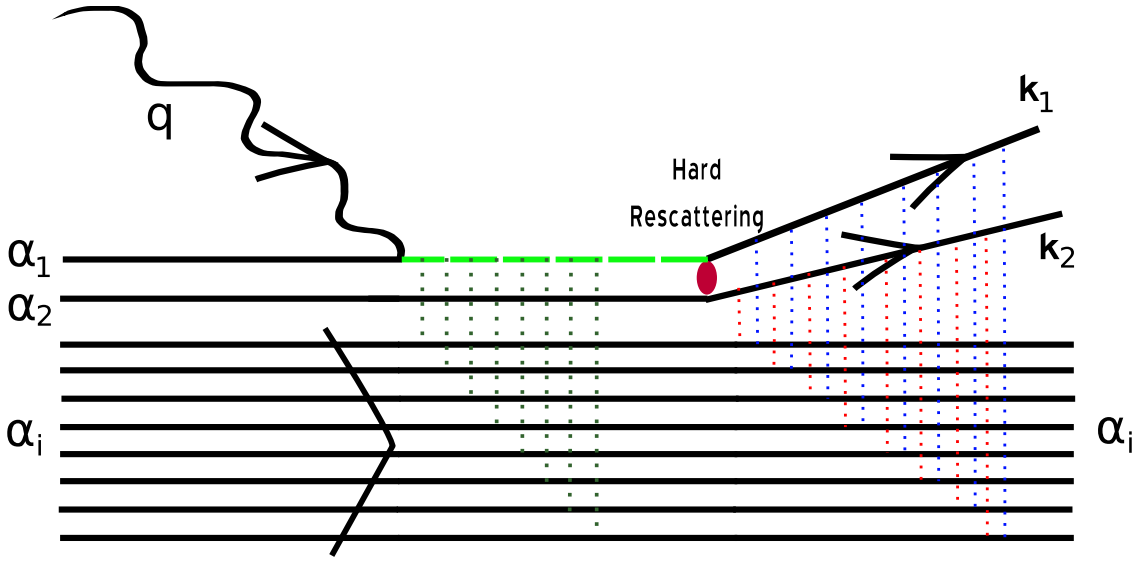

Figure 2.7 Diagram representing the $A(\gamma, N_1N_2)$ as a two-step hard rescattering process. The red, blue and black dotted lines represent the FSI with the residual spectator nucleons. The dashed green line is the nucleon propagator between the photon interaction and the hard rescattering process.

In the above two equations $\vec{r}_j$ is the vertex of the photon interaction. Further, $(\vec{r}_0, \vec{r}_k)$ determine the spatial coordinates of the hard rescattering process. In Eq. (2.61) we ignore medium modifications to the $D_N(\vec{r}_0 - \vec{r}_j)$ propagator, and put the pole of the propagator on the free nucleon mass shell . With these notations, the matrix element (2.49) reads:

$$\mathscr{M}^{(\gamma,N_1N_2)}_{if,\mathrm{HRM}} = \int d\vec{r}_0 \dots d\vec{r}_A \left(\Psi_A^{\vec{k}_1 m_{s_1}, \vec{k}_2 m_{s_2}}(\vec{r}_0, \vec{r}_2, \dots, \vec{r}_A)\right)^\dagger \sum_{k\neq j} \hat{O}(\vec{r}_0, \vec{r}_k) \times \sum_j D^D_{\mathscr{N}}(\vec{r}_0 - \vec{r}_j)\Gamma^\mu(\vec{r}_j)\epsilon_\mu(\lambda) e^{i\vec{q}\cdot\vec{r}_k} \Psi_A^{\mathrm{g.s.}}(\vec{r}_1, \dots, \vec{r}_A). \quad (2.63)$$

Due to antisymmetrization, we can take one term in the sum of both operators and multiply Eq. (2.63) with A for the photon coupling vertex and $(A-1)$ for the hard rescattering operator. If we take α_1 and α_2 for the quantum numbers of the ejected nucleons and again assume spin independent, elastic and mildly inelastic FSI, we obtain (with Dirac indices written out explicitly to avoid confusion)

$$\begin{aligned}
\mathscr{M}^{(\gamma,N_1N_2)}_{if,\mathrm{HRM}} \approx \frac{A(A-1)(A-2)!}{A!} \int d\vec{r}_0 d\vec{r}_1 \cdots d\vec{r}_A |\phi_{\alpha_3}(\vec{r}_3)|^2 \dots |\phi_{\alpha_A}(\vec{r}_A)|^2 \\
\times \Big[u_a^\dagger(\vec{k}_1, m_{s_1}) e^{-i\vec{k}_1\cdot\vec{r}_0} u_b^\dagger(\vec{k}_2, m_{s_2}) e^{-i\vec{k}_2\cdot\vec{r}_2} \hat{\mathscr{S}}_{K_1N}(\vec{r}_0; \vec{r}_3, \dots, \vec{r}_A) \hat{\mathscr{S}}_{K_2N}(\vec{r}_2; \vec{r}_3, \dots, \vec{r}_A) \\
- u_a^\dagger(\vec{k}_2, m_{s_2}) e^{-i\vec{k}_2\cdot\vec{r}_0} u_b^\dagger(\vec{k}_1, m_{s_1}) e^{-i\vec{k}_1\cdot\vec{r}_2} \hat{\mathscr{S}}_{K_1N}(\vec{r}_2; \vec{r}_3, \dots, \vec{r}_A) \hat{\mathscr{S}}_{K_2N}(\vec{r}_0; \vec{r}_3, \dots, \vec{r}_A) \Big] \\
\times \hat{O}_{ab;cd}(\vec{r}_0, \vec{r}_2) \hat{\mathscr{S}}_{\mathscr{N}N}(\vec{r}_0, \vec{r}_1; \vec{r}_3, \dots, \vec{r}_A) \left(D_N(\vec{r}_0 - \vec{r}_1)\right)_{ce} \left(\Gamma^\mu(\vec{r}_1)\right)_{ef} \epsilon_\mu(\lambda) e^{i\vec{q}\cdot\vec{r}_1} \\
\times \Big[\left(\phi_{\alpha_1}(\vec{r}_1)\right)_f \left(\phi_{\alpha_2}(\vec{r}_2)\right)_d - \left(\phi_{\alpha_2}(\vec{r}_1)\right)_f \left(\phi_{\alpha_1}(\vec{r}_2)\right)_d \Big]. \quad (2.64)
\end{aligned}$$

To further simplify Eq. (2.64), we define the FSI factor

$$\mathscr{F}_{\mathrm{FSI}}(\vec{r}_0,\vec{r}_1,\vec{r}_2) = \int d\vec{r}_3 \ldots \int d\vec{r}_A |\phi_{\alpha_3}(\vec{r}_3)|^2 \ldots |\phi_{\alpha_A}(\vec{r}_A)|^2 \times \hat{\mathscr{S}}_{K_1N}(\vec{r}_0;\vec{r}_3,\ldots,\vec{r}_A)\hat{\mathscr{S}}_{K_2N}(\vec{r}_2;\vec{r}_3,\ldots,\vec{r}_A)\hat{\mathscr{S}}_{\mathscr{N}N}(\vec{r}_0,\vec{r}_1;\vec{r}_3,\ldots,\vec{r}_A). \quad (2.65)$$

We adopt the zero-range approximation for the hard nucleon-nucleon rescattering allowing us to replace the two coordinates $\vec{r}_0$ and $\vec{r}_2$ of the two interacting protons with one collision point. Applying this to Eq. (2.65):

$$\mathscr{F}_{\mathrm{FSI}}(\vec{r}_0,\vec{r}_1,\vec{r}_2) \approx \mathscr{F}_{\mathrm{FSI}}(\vec{r}_2,\vec{r}_1,\vec{r}_2) \equiv \mathscr{F}_{\mathrm{FSI}}(\vec{r}_1,\vec{r}_2) \quad (2.66)$$

We now write the free nucleon propagator and hard rescattering operator in momentum space

$$D_N(\vec{r}_0-\vec{r}_1) = \int \frac{d\vec{P}}{(2\pi)^3} e^{i\vec{P}\cdot(\vec{r}_0-\vec{r}_1)} D_N(\vec{P}), \quad (2.67)$$

$$\hat{O}(\vec{r}_0,\vec{r}_2) = \int \frac{d\vec{p}}{(2\pi)^3} e^{i\vec{p}\cdot(\vec{r}_2-\vec{r}_0)} \hat{O}(\vec{p}). \quad (2.68)$$

After eliminating the $\vec{r}_0$ integration and with $\vec{p}_{m_1} \equiv \vec{P}-\vec{q}$ and $\vec{p}_{m_2} \equiv \vec{k}_1+\vec{k}_2-\vec{P}$, the matrix element reads

$$\mathscr{M}^{(\gamma,N_1N_2)}_{if,\mathrm{HRM}} \approx \int d\vec{r}_1 \int d\vec{r}_2 \int \frac{d\vec{P}}{(2\pi)^3} \Big(u_a^\dagger(\vec{k}_1,m_{s_1}) u_b^\dagger(\vec{k}_2,m_{s_2}) \hat{O}_{ab;cd}(\vec{P}-\vec{k}_1) - u_a^\dagger(\vec{k}_2,m_{s_2}) u_b^\dagger(\vec{k}_1,m_{s_1}) \hat{O}_{ab;cd}(\vec{P}-\vec{k}_2) \Big) \Big(D_N(\vec{P})\Big)_{ce} \Big(\Gamma^\mu(\vec{r}_1)\Big)_{ef} \epsilon_\mu(\lambda) \times e^{-i\vec{p}_{m_1}\cdot\vec{r}_1} e^{-i\vec{p}_{m_2}\cdot\vec{r}_2} \Big[\Big(\phi_{\alpha_1}(\vec{r}_1)\Big)_f \Big(\phi_{\alpha_2}(\vec{r}_2)\Big)_d - \Big(\phi_{\alpha_2}(\vec{r}_1)\Big)_f \Big(\phi_{\alpha_1}(\vec{r}_2)\Big)_d \Big] \times \mathscr{F}_{\mathrm{FSI}}(\vec{r}_1,\vec{r}_2). \quad (2.69)$$

One of the terms entering in Eq. (2.69) is shown in Fig. 2.8.

As a last step we neglect the negative-energy projections in the free nucleon propagator. The energy in their denominator P^0+E_P (with $P^0 = q+\sqrt{m_N^2+p_{m_1}^2}$ and $E_P = \sqrt{m_N^2+P^2}$) will be large compared to the one of the positive energy projections:

$$D_N(\vec{P}) = -\frac{m_N}{E_N} \sum_{s_P} \left(\frac{u(\vec{P},s_P)\bar{u}(\vec{P},s_P)}{P^0-E_P+i\eta} + \frac{v(\vec{P},s_P)\bar{v}(\vec{P},s_P)}{P^0+E_P-i\eta} \right) \approx -\frac{m_N}{E_N} \frac{\sum_{s_P} u(\vec{P},s_P)\bar{u}(\vec{P},s_P)}{P^0-E_P+i\eta}. \quad (2.70)$$

Finally, we insert a complete set $\sum_{s_m} \Big[u(\vec{p}_{m_2},s_m)\bar{u}(\vec{p}_{m_2},s_m) - v(\vec{p}_{m_2},s_m)\bar{v}(\vec{p}_{m_2},s_m)\Big]$ in Eq. (2.69). After neglecting the negative energy contributions of this complete set, the matrix

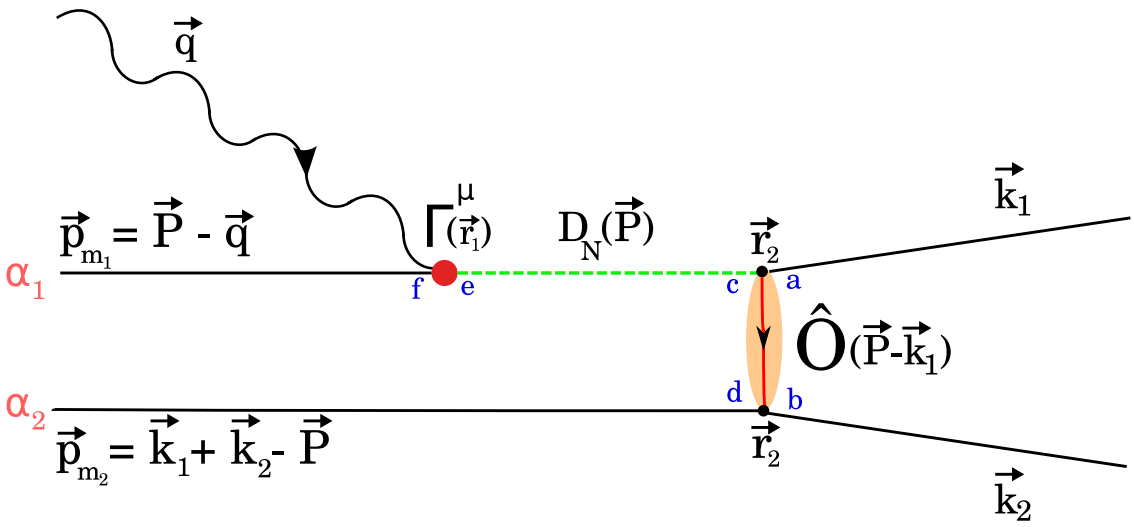

Figure 2.8 Schematic representation of one of the terms entering in Eq. (2.69). Dirac indices are shown in blue. The other three terms are obtained by interchanging $\alpha_1 \leftrightarrow \alpha_2$ and $\vec{k}_1 \leftrightarrow \vec{k}_2$.

element of Eq. (2.69) can be written as

$$\mathscr{M}^{(\gamma,N_1N_2)}_{if,\mathrm{HRM}} \approx -\sum_{s_m,s_P}\int \frac{d\vec{P}}{(2\pi)^3}\frac{m_N}{E_N}\Big(u^\dagger_a(\vec{k}_1,m_{s_1})u^\dagger_b(\vec{k}_2,m_{s_2})\hat{O}_{ab;cd}(\vec{P}-\vec{k}_1)$$
$$-u^\dagger_a(\vec{k}_2,m_{s_2})u^\dagger_b(\vec{k}_1,m_{s_1})\hat{O}_{ab;cd}(\vec{P}-\vec{k}_2)\Big)\times u_c(\vec{P},s_P)u_d(\vec{p}_{m_2},s_m)$$
$$\times\frac{1}{P^0-E_P+i\eta}\Big[<J^D_{\alpha_1,\alpha_2}(\vec{p}_{m_1},\vec{p}_{m_2},\lambda)> - <J^D_{\alpha_2,\alpha_1}(\vec{p}_{m_1},\vec{p}_{m_2},\lambda)>\Big]. \quad (2.71)$$

In this last equation

$$<J^D_{\alpha_1,\alpha_2}(\vec{p}_{m_1},\vec{p}_{m_2},\lambda)>=\epsilon_\mu(\lambda)\int d\vec{r}_1\int d\vec{r}_2 e^{-i\vec{p}_{m_1}\cdot\vec{r}_1}e^{-i\vec{p}_{m_2}\cdot\vec{r}_2}$$
$$\times[\bar{u}(\vec{P},s_P)\Gamma^\mu(\vec{r}_1)\phi_{\alpha_1}(\vec{r}_1)][\bar{u}(\vec{p}_{m_2},s_m)\phi_{\alpha_2}(\vec{r}_2)]\mathscr{F}_{\mathrm{FSI}}(\vec{r}_1,\vec{r}_2). \quad (2.72)$$

For a real incoming photon, the denominator of the propagator in Eq. (2.70) can never reach on-the-mass-shell conditions and the integration poses no problem. For a virtual photon the denominator of the propagator can be spit into two parts, one for the on-shell contribution (yielding a delta function) and one for the off-shell contribution (yielding a principal value integration) [95]:

$$\frac{1}{P^0-E_P+i\eta}=-i\pi\delta(P^0-E_P)+\mathscr{P}\left(\frac{1}{P^0-E_P}\right). \quad (2.73)$$

We can also relate the hard rescattering operator to the free NN scattering amplitude $\mathscr{M}^{NN}$:

$$\mathscr{M}^{NN}=\bar{u}_a(\vec{k}_1,m_{s_1})\bar{u}_b(\vec{k}_2,m_{s_2})\mathscr{D}^{NN}_{ab;cd}u_c(\vec{k}_3,m_{s_3})u_d(\vec{k}_4,m_{s_4})$$
$$\approx u^\dagger_a(\vec{k}_1,m_{s_1})u^\dagger_b(\vec{k}_2,m_{s_2})\gamma^0_{ae}\gamma^0_{bf}\hat{O}_{ab;cd}u_c(\vec{k}_3,m_{s_3})u_d(\vec{k}_4,m_{s_4}), \quad (2.74)$$

were we neglected medium effects in the last step. If all four legs of the NN scattering amplitude are on-shell, the amplitude can be parametrized in terms of five Fermi invariants as [96]

$$\mathscr{D}^{NN}_{ab;cd} = \mathscr{F}_S(s,t)\delta_{ac}\delta_{bd} + \mathscr{F}_V(s,t)\gamma_{ac}\cdot\gamma_{bd} + \mathscr{F}_T(s,t)\sigma^{\mu\nu}_{ac}(\sigma_{\mu\nu})_{bd} + \mathscr{F}_P(s,t)\gamma^5_{ac}\gamma^5_{bd} + \mathscr{F}_A(s,t)(\gamma^5\gamma)_{ac}\cdot(\gamma^5\gamma)_{bd}\,, \quad (2.75)$$

with s and t the Mandelstam variables. The Fermi invariants in Eq. (2.75) can be calculated from five helicity amplitudes as is covered in Appendix D. For the calculations in this thesis we use the helicity amplitudes available from SAID [97, 98], in function of s and $\cos\theta_{\text{c.m.}}$.

For the nucleon-nucleon rescattering shown in Fig. 2.7, both the incoming nucleons are off-the-mass-shell. For the second bound nucleon, the insertion of positive energy projections in Eq. (2.71) has put this incoming nucleon line on the positive-energy mass shell. The positive-energy contributions of the nucleon propagator, however, still include off-shell behavior. A dynamical model describing the off-shell behaviour of the scattering amplitudes in the energy range accessible at JLab is currently not available. To estimate these effects we use the prescription for the off-shell behavior of the amplitude proposed in [95]. The form of Eq. (2.75) is kept, although additional invariants are possible with an off-shell nucleon. The center of mass angle can be derived from the three Mandelstam variables:

$$\cos\theta_{\text{c.m.}} = \frac{t-u}{\sqrt{s-4m^2}\sqrt{\frac{(4m^2-t-u)^2}{s}-4m^2}}\,. \quad (2.76)$$

The Fermi invariants become

$$\mathscr{F}_i(s,t) \to \mathscr{F}_i(s,t,u)F_N(s+t+u-3m^2) \quad \text{for } i \equiv S,V,T,P\text{and } A, \quad (2.77)$$

where

$$F_N(p^2) = \frac{(\Lambda_N^2-m^2)^2}{(p^2-m^2)^2+(\Lambda_N^2-m^2)^2}\,. \quad (2.78)$$

is an off-shell nucleon form factor with a cutoff mass $\Lambda_N = 1.675$ GeV. With all these ingredients, we can numerically compute the matrix element of Eq. (2.71).

2.2 Final-State Interactions

2.2.1 Relativistic Multiple-Scattering Glauber Approximation

The Glauber approach can be justified when the wavelength of the outgoing hadron is sufficiently small in comparison to the typical interaction length with the residual nucleons.

In the context of $A(e,e'p)$ reactions [73] it was shown that the Glauber model represents a realistic approach to FSI for proton kinetic energies down to about 300 MeV. This corresponds to proton de Broglie wavelengths of the order of 1.5 fm. For pions comparable wavelengths are reached for kinetic energies of the order of 700 MeV.

A relativistic extension of the Glauber model, dubbed the relativistic multiple-scattering Glauber approximation (RMSGA), was introduced in Ref. [72]. In the RMSGA, the wave function for the ejected nucleon and pion is a convolution of a relativistic plane wave and a Glauber eikonal phase operator that accounts for FSI mechanisms. In Glauber theory the assumption is made that a fast-moving particle interacts through elastic or mildly inelastic collisions with *frozen* point scatterers in a target. Scattering angles are assumed small and each of the point scatterers adds a phase to the wave function (EA). This added phase is directly related to nucleon-nucleon or pion-nucleon scattering data through the introduction of a profile function.

As a starting point in the derivation of the RMSGA FSI-factor in Eqs. (2.6) and (2.7), we consider the scattering amplitude of a Dirac particle subject to a Lorentz scalar $[V_s(r)]$ and vector $[V_v(r)]$ potential in the EA [99]:

$$F_{m_s,m_s'}(\vec{k}_i,\vec{k}_f,E) = -\frac{m_N}{2\pi}\langle\psi^{(+)}_{\vec{k}_f,m_s'} \mid (\beta V_s + V_v) \mid \Phi_{\vec{k}_i,m_s}\rangle\,, \tag{2.79}$$

with $\psi^{(+)}_{\vec{k}_f,m_s'}$ the relativistic scattered state in the EA and $\Phi_{\vec{k}_i,m_s}$ a Dirac plane wave. After some algebraic manipulations, Eq. (2.79) can be transformed into [99]

$$F_{m_s,m_s'}(\vec{k}_i,\vec{k}_f,E) = \langle m_s' \mid \frac{K}{2\pi i}\int d\vec{b}\; e^{i\vec{\Delta}\cdot\vec{b}}\Gamma_{N'N}(\vec{b}) \mid m_s\rangle\,, \tag{2.80}$$

with

$$\vec{K} = \frac{1}{2}(\vec{k}_i + \vec{k}_f)\,, \tag{2.81}$$

$$\vec{\Delta} = \vec{k}_i - \vec{k}_f\,. \tag{2.82}$$

$\vec{K}$ lies along the z-axis and the impact parameter vector $\vec{b}$ is perpendicular to it. In Eq. (2.80), we introduced the profile function $\Gamma_{N'N}(\vec{b})$. The profile function is related to the eikonal phase $\chi(\vec{b})$ occurring in the scattered wave function via

$$\Gamma_{N'N}(\vec{b}) = 1 - e^{i\chi(\vec{b})}\,. \tag{2.83}$$

The eikonal phase depends on the scalar and vector potentials and their derivatives [99]. In the Glauber approximation, the profile function is related to the nucleon-nucleon scattering parameters and no knowledge about the scalar and vector optical potentials is required. For

relativistic pion-nucleon scattering an analogous expression to Eq. (2.80),

$$F(\vec{k}_i,\vec{k}_f,E)=\frac{K}{2\pi i}\int d\vec{b}e^{i(\vec{k}_i-\vec{k}_f)\cdot\vec{b}}\Gamma_{\pi N}(\vec{b}), \tag{2.84}$$

can be derived in a straightforward manner as is shown in App. C. Thus, by applying the following derivation to pion-nucleon scattering, one will arrive at the same conclusion for the pion FSI.

The most general form of the NN-scattering amplitude, assuming parity conservation, time-reversal invariance, the Pauli principle and isospin invariance, can be written as the sum of five invariant amplitudes [100]:

$$\begin{aligned}\mathscr{M}^{NN}=&A(\vec{\Delta})+B(\vec{\Delta})(\vec{\sigma}_1+\vec{\sigma}_2)\cdot\hat{n}+C(\vec{\Delta})(\vec{\sigma}_1\cdot\hat{n})(\vec{\sigma}_2\cdot\hat{n})\\&+D(\vec{\Delta})(\vec{\sigma}_1\cdot\hat{m})(\vec{\sigma}_2\cdot\hat{m})+E(\vec{\Delta})(\vec{\sigma}_1\cdot\hat{l})(\vec{\sigma}_2\cdot\hat{l}).\end{aligned} \tag{2.85}$$

In this last equation, $\hat{n}=\frac{\vec{k}_i\times\vec{k}_f}{|\vec{k}_i\times\vec{k}_f|}$, $\hat{m}=\frac{\vec{k}_i-\vec{k}_f}{|\vec{k}_i-\vec{k}_f|}$, $\hat{l}=\frac{\vec{k}_i+\vec{k}_f}{|\vec{k}_i+\vec{k}_f|}$ and $\vec{\sigma}_1$, $\vec{\sigma}_2$ are the nucleon spin operators. As one can infer from Eq. (2.85), the amplitude consists of a central term ($A(\vec{\Delta})$), a spin-orbit term ($B(\vec{\Delta})$) and another three spin-dependent terms. The five invariants of Eq. (2.85) can be related to the Fermi invariants of Eq. (2.75), and a transformation between the two is straightforward [96]. In theory, a complete phase-shift analysis of the NN scattering data can determine all five amplitudes entering in Eq. (2.85). In the analysis of proton-nucleus scattering with proton momenta of 1 GeV/c, the spinless approximation to Eq. (2.85) - whereby only the $A(\vec{\Delta})$ term is kept - was very successful [100]. We apply this approximation and parametrize the scattering amplitude as

$$F(\vec{\Delta})\approx A(\vec{\Delta}=0)e^{-\frac{\beta_{N'N}^2\Delta^2}{2}}, \tag{2.86}$$

with $\beta_{N'N}$ the slope parameter. This Gaussian parametrization is based on the diffractive nature of the elastic cross section for high energy nucleon-nucleon scattering. At GeV momenta, the elastic cross section is extremely forward peaked and drops exponentially over many orders. By employing the optical theorem $Im\,F(\theta=0,\phi=0)=\frac{k\sigma^{\text{tot}}}{4\pi}$, we can write

$$F(\vec{\Delta})\approx\frac{k\sigma_{N'N}^{\text{tot}}}{4\pi}(\epsilon_{N'N}+i)e^{-\frac{\beta_{N'N}^2\Delta^2}{2}}, \tag{2.87}$$

with $\sigma_{N'N}^{\text{tot}}$ the total cross section and $\epsilon_{N'N}$ the ration of the real to imaginary part of the amplitude. We can now obtain an expression for the profile functions by inverting the Fourier transform of Eqs. (2.80) and (2.84):

$$\Gamma_{iN}(\vec{b})=\frac{\sigma_{iN}^{\text{tot}}(1-i\epsilon_{iN})}{4\pi\beta_{iN}^2}\exp\left(-\frac{\vec{b}^2}{2\beta_{iN}^2}\right)\ (\text{with } i=\pi \text{ or } N'). \tag{2.88}$$

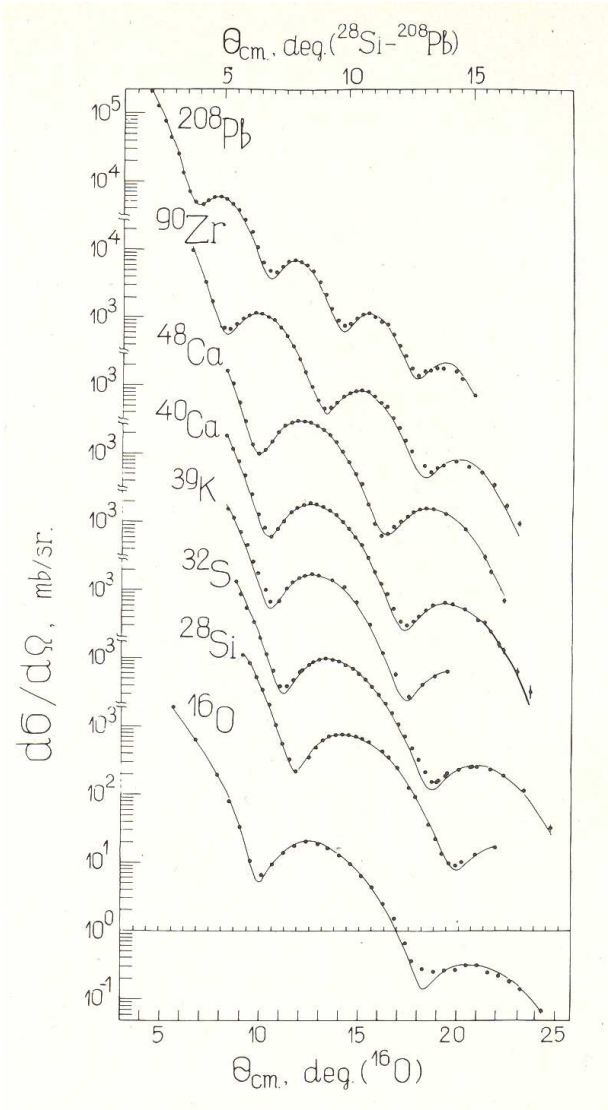

Figure 2.9 Differential cross sections for elastic proton-nucleus scattering at 1 GeV. Figure taken from Ref. [101].

To extend this formalism to the multiple-scattering case, we consider the soft interactions of a fast particle with a composite target. In Fig. 2.9, we show differential cross section data for the elastic scattering of 1 GeV protons with several nuclei. In Fig. 2.10, we show similar results for the elastic scattering of 800 MeV pions with ^{12}C and ^{40}Ca. These figures clearly illustrate that these cross sections are extremely forward peaked. The cross section drops a few orders before reaching $\theta_{\text{c.m.}} = 10^o$, corresponding with lab angles between 9 and 10 degrees for the nuclei considered. Therefore, it seems plausible to assume that the soft interactions of the fast ejected particle will only cause small-angle changes in the trajectory of the fast particle. The high-momentum scattered particle is assumed to traverse the target in a very short time. This allows us to neglect the motion of the target

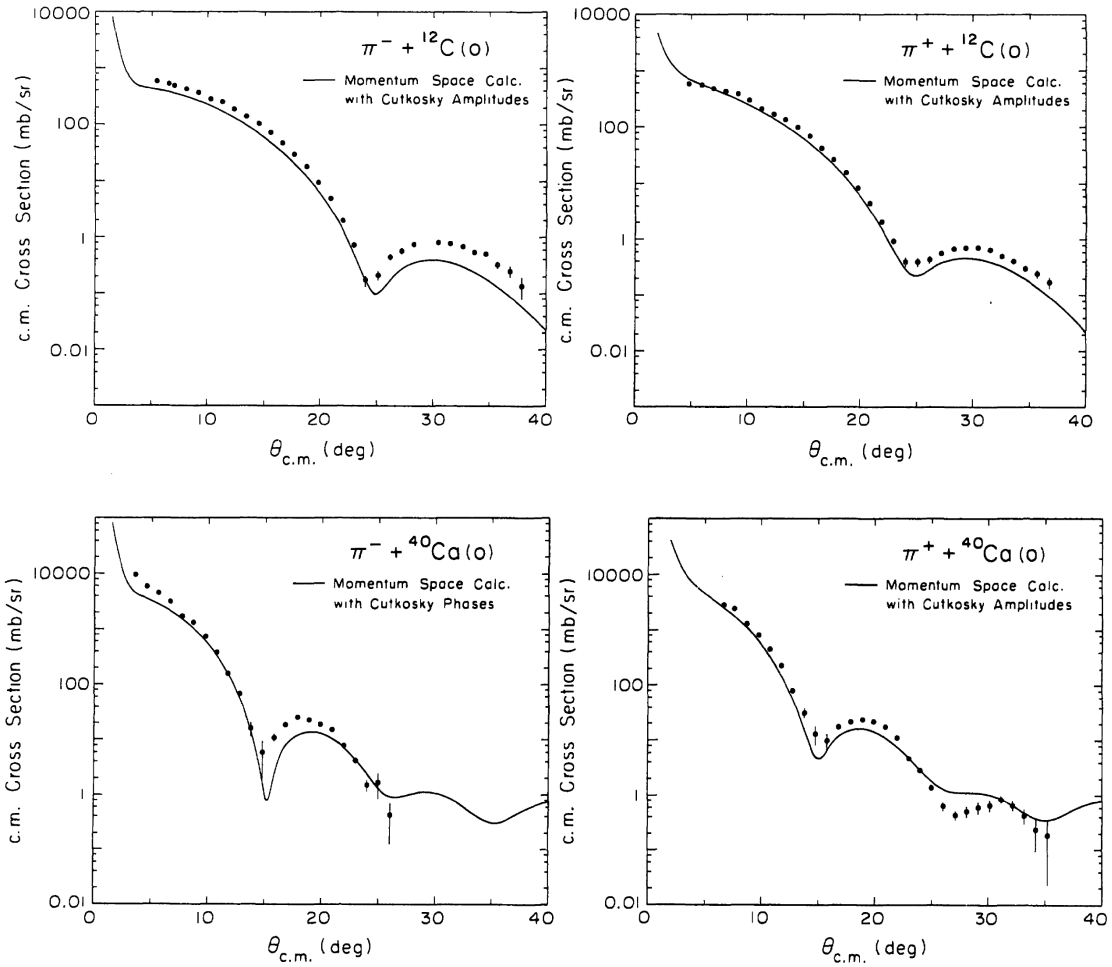

Figure 2.10 Differential cross sections for elastic pion-nucleus scattering at 800 MeV with ^{12}C and ^{40}Ca nuclei. Figure taken from Ref. [102].

particles, the so-called frozen approximation. The interactions with the scattering centers are supposed to occur through two-body spin-independent interactions as we described before. Charge exchange effects between the fast ejectile and the target constituents are also neglected. The one-dimensional nature of the relative motion, together with the frozen approximation, neglect of three-body forces and longitudinal momentum transfer, allows us to add the eikonal phases of all the individual scattering centers along the trajectory of the fast particle. This yields the following expression for the Glauber amplitude of a multiple-scattering event from a $A-1$-particle target with initial state $|\, i\rangle$ to a final state $|\, f\rangle$ [103]:

$$F(\vec{\Delta}) = \frac{iK}{2\pi}\int d\vec{b}\; e^{i\vec{b}\cdot\vec{\Delta}}\langle f \mid \Gamma_{iN}^{\rm tot}(\vec{b},\vec{b}_2,\ldots,\vec{b}_A)\mid i\rangle\,, \;\; (\text{with } i=\pi \text{ or } N') \tag{2.89}$$

with $\vec{b}$ the impact parameter of the ejectile and $\vec{b}_j$ those of the scattering targets. The total

profile function is defined as

$$\Gamma_{iN}^{\rm tot}(\vec{b},\vec{b}_2,\ldots,\vec{b}_A) = 1 - e^{i\chi^{\rm tot}(\vec{b},\vec{b}_2,\ldots,\vec{b}_A)} = \\ 1 - e^{i\sum_{j=2}^{A}\chi^j(\vec{b}-\vec{b}_j)} = 1 - \prod_{j=2}^{A}(1-\Gamma_{iN}^j(\vec{b}-\vec{b}_j)\,,\ (\text{with } i=\pi \text{ or } N') \quad (2.90)$$

whereby the last step requires the principle of phase-shift additivity. This results in the following expression for the Glauber multiple-scattering eikonal phase for the FSI in the $(A-1)$ residual nucleus:

$$\widehat{\mathscr{S}_{iN}}(\vec{r},\vec{r}_2,\ldots,\vec{r}_A) = \prod_{j=2}^{A}\left[1-\Gamma_{iN}(\vec{b}-\vec{b}_j)\theta(z_j-z)\right]\ (\text{with } i=\pi \text{ or } N')\,. \quad (2.91)$$

Here, $\vec{r}_j(\vec{b}_j,z_j)$ are the coordinates of the residual nucleons and $\vec{r}(\vec{b},z)$ specifies the interaction point with the (virtual) photon. In Eq. (2.91), the z axis lies along the path of the ejected particle i (the proton or pion) and $\vec{b}$ is perpendicular to this path. The Heaviside step function θ guarantees that only nucleons in the forward path of the outgoing particle contribute to the eikonal phase.

The parameters $\sigma_{iN}^{\rm tot}$, β_{iN} and ϵ_{iN} used in the parametrization of the profile functions depend on the momentum of the outgoing nucleon or pion i. For $i=N'$, we determined the parameters by performing a fit [72] to the $N'N \longrightarrow N'N$ databases from the Particle Data Group (PDG) [104]. For the pion, $\sigma_{\pi N}^{\rm tot}$ was fitted to data collected by PDG [104]. The analysis of the slope parameter in Ref. [105] was used for the $\beta_{\pi N}$ fits. Fits provided by SAID [106, 107] and data from PDG [104] were used in constructing the fits for $\epsilon_{\pi N}$. The fits for $\sigma_{iN}^{\rm tot}, \beta_{iN}$, and ϵ_{iN} of Figs. 2.11, 2.12, and 2.13 are the result of a χ^2 minimization of the data against a a n-th degree polynomial (with $n \leq 10$). An alternative way of determining $\beta_{\pi N}$, is via the relation

$$\beta_{\pi N}^2 = \frac{(\sigma_{\pi N}^{\rm tot})^2(1+\epsilon_{\pi N}^2)}{16\pi\sigma_{\pi N}^{\rm el}}\,, \quad (2.92)$$

with $\sigma_{\pi N}^{\rm el}$ the elastic cross section. Fits for $\sigma_{\pi N}^{\rm el}$ to data from PDG [104] are also presented in Fig. 2.11. The two sets for the $\beta_{\pi N}$ parameter in Fig. 2.12 do not produce significantly different results for the numerical calculations presented here. We use the χ^2 fit for $\beta_{\pi N}$ in all calculations presented in this work.

The Glauber operator of Eq. (2.91) is an A-body operator. As a consequence, it requires integrations over all spectator nucleon coordinates in Eqs. (2.12), (2.54), and (2.65) which is computationally very demanding, in particular for heavy target nuclei. In computing the $A(\gamma^{(*)},N\pi)$ amplitude and the single-step contribution to $A(\gamma,N_1N_2)$ (Fig. 2.4), a product of

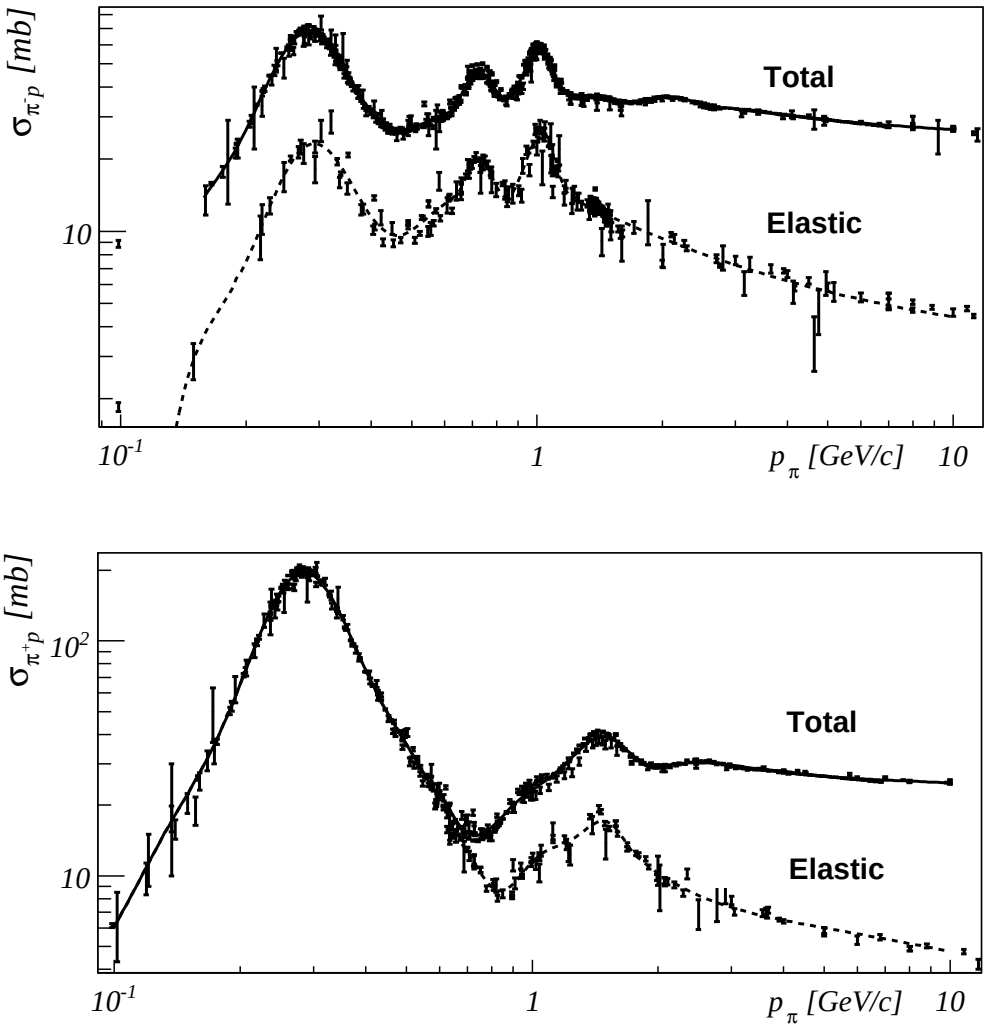

Figure 2.11 The pion lab-momentum dependence of the data [104] and adopted fits for the total and elastic cross section for π^--p (upper panel) and π^+-p (lower panel) scattering.

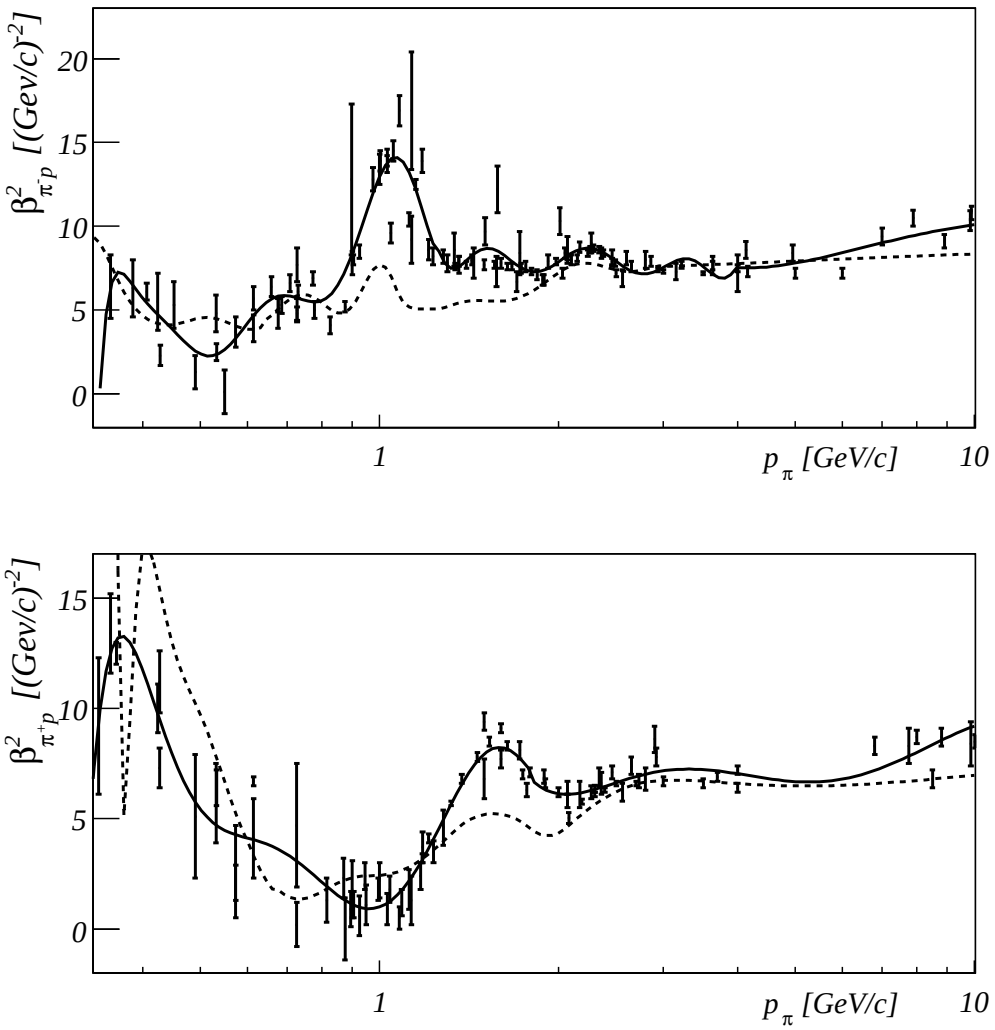

Figure 2.12 The pion lab-momentum dependence of the data [105] and fits for the $\beta^2_{p\pi}$ parameter for π^--p (upper panel) and π^+-p (lower panel) scattering. Full curves are a χ^2 fit to the data, whereas the dashed curves result from Eq. (2.92).

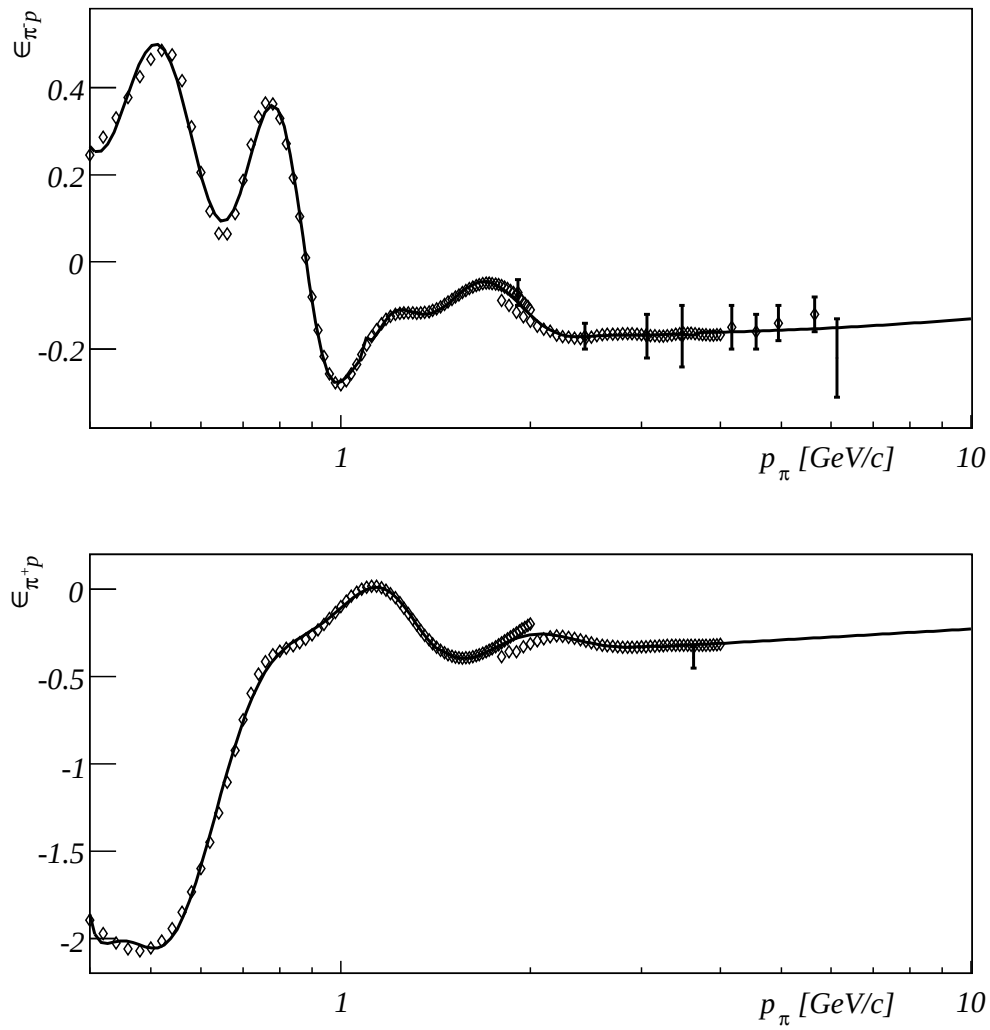

Figure 2.13 The pion lab-momentum dependence of the ratio of the real to imaginary part of the π^--p (upper panel) and π^+-p (lower panel) amplitudes. The diamonds represent an analysis of the data by the George Washington University group [106, 107], whereas the solid circles are from PDG [104]. The solid line is the fit to the data that are used in the numerical calculations.

two Glauber phases is involved. Accordingly, the cylindrical symmetry is lost. This increases the computational cost an order of magnitude compared to single hadron knockout of e.g. the $A(e,e'p)$ type. The HRM contribution to the $A(\gamma,N_1N_2)$ process, via the intermediate nucleon propagator, adds three extra spatial degrees of freedom and a third Glauber phase to the problem. The computation time for these calculations soars to new heights. A Romberg algorithm is used to perform the integrations over the spatial coordinates in the FSI factors.

2.2.2 Relativistic Optical Model Eikonal Approximation

For nucleons with a kinetic energy lower than about 300 MeV, the assumptions underlying the Glauber formalism are no longer justified, and an alternative method to model FSI is required. Under those circumstances our framework provides the flexibility to adopt the relativistic optical model eikonal approximation (ROMEA) [74]. In the ROMEA approach, the wave function $\psi^{(+)}_{\vec{p}_N,m_s}$ of a nucleon with asymptotic energy $E=\sqrt{p_N^2+m_N^2}$ after scattering in a scalar $[V_s(r)]$ and vector $[V_v(r)]$ spherical potential is a solution of the Dirac equation:

$$\mathscr{H}\psi^{(+)}_{\vec{p}_N,m_s}(\vec{r})=\left[\vec{\alpha}\cdot\hat{\vec{p}}+\beta(M_N+V_s(r))\right]\psi^{(+)}_{\vec{p}_N,m_s}(\vec{r})=(E-V_v(r))\psi^{(+)}_{\vec{p}_N,m_s}(\vec{r}), \tag{2.93}$$

with $\hat{\vec{p}}$ the momentum operator. In the relativistic distorted wave impulse approximation (RDWIA), the scattering wave function $\psi^{(+)}_{\vec{p}_N,m_s}(\vec{r})$ is expanded in partial waves and solved numerically. At higher energies, the partial-wave procedure gets cumbersome and the eikonal approximation is the by far the most economical way of calculating things. In the EA, we can readily apply the small angle approximation and the following approximation for the momentum operator is made [71]:

$$\hat{p}^2=[(\hat{\vec{p}}-\vec{K})+\vec{K}]^2\approx 2\vec{K}\cdot\hat{\vec{p}}-K^2, \tag{2.94}$$

with $\vec{K}=\frac{1}{2}(\vec{k}_i+\vec{k}_f)$ the average of the initial and final momentum of the scattered particle. In the small angle approximation, $\vec{K}\approx\vec{p}_N$ and points along the z axis. By using Eq. (2.94), the differential equation for the upper component of the scattering wave function is transformed into a first order one. After adopting the eikonal ansatz for the upper component (with N a normalization factor)

$$u^{(+)}_{\vec{p}_N,m_s}(\vec{r})\equiv Ne^{i\vec{p}_N\cdot\vec{r}}e^{i\mathscr{J}_{N'N}(\vec{r})}\chi_{\frac{1}{2}m_s}, \tag{2.95}$$

the scattering wave function adopts the following form [99]

$$\psi^{(+)}_{\vec{p}_N,m_s}(\vec{r})=\sqrt{\frac{E+m_N}{2m_N}}\begin{bmatrix}1\\ \frac{1}{E+m_N+V_s(r)-V_v(r)}\vec{\sigma}\cdot\hat{\vec{p}}\end{bmatrix}e^{i\vec{p}_N\cdot\vec{r}}e^{i\mathscr{J}_{N'N}(\vec{r})}\chi_{\frac{1}{2}m_s}, \tag{2.96}$$

with the eikonal phase determined by

$$i\hat{\mathscr{S}}_{N'N}(\vec{b},z) = -i\frac{m_N}{K}\int_{-\infty}^{z} dz'\left\{V_c(\vec{b},z') + V_{so}(\vec{b},z')\left[\vec{\sigma}\cdot(\vec{b}\times\vec{K}) - iKz'\right]\right\}. \tag{2.97}$$

Eq. (2.96) differs from a plane-wave solution in two ways. The eikonal phase $e^{i\hat{\mathscr{S}}_{N'N}(\vec{r})}$ includes the interaction of the nucleon with the nucleus via potential scattering and the lower component of the Dirac spinor is dynamically enhanced due to the combination of the scalar and vector potentials $V_s - V_v < 0$. The central and spin-orbit potentials V_c and V_{so} are functions of V_s and V_v and their derivatives:

$$\begin{aligned} V_c(r) &= V_r(r) + \frac{E}{m_N}V_v(r) + \frac{V_s^2(r) - V_v^2(r)}{2M_N}, \\ V_{so}(r) &= \frac{1}{2M_N\left[E + M_N + V_s(r) - V_v(r)\right]}\frac{1}{r}\frac{d}{dr}\left[V_v(r) - V_s(r)\right]. \end{aligned} \tag{2.98}$$

For protons in the intermediate energy range ($T_p \approx 500$ MeV), calculations with the EA are in very good agreement with exact partial wave solutions [99]. The ROMEA has been successfully applied to $A(e,e'p)$ [108, 109] and $A(p,2p)$ [74] reactions.

In the practical implementation of the ROMEA model we have made a few additional assumptions. The dynamical enhancement of the lower components of the scattering wave function (2.96) constitutes a rather small effect. Indeed, at low momenta the lower components are small compared to the upper components due to the presence of $\hat{\vec{p}}$ in $\vec{\sigma}\cdot\vec{p}$. At higher momenta, $(V_s - V_v)$ is small in comparison to $(E + m_N)$. In the ROMEA calculations presented in this work, this enhancement is neglected, though it is straightforward to include it (at the cost of increasing the computing time). The operator $\hat{\vec{p}}$ was substituted by the asymptotic value $\vec{p}_N$. Finally, as collisions were assumed spin independent in Eq. (2.10), the spin-orbit potential V_{so} in Eq. (2.97) is neglected. This yields the following phase factor entering in Eq. (2.12):

$$\hat{\mathscr{S}}^{\text{ROMEA}}_{N'N}(\vec{r}) = e^{-i\frac{m_N}{p_N}\int_{z_N}^{+\infty} dz V_c(\vec{b}_{p_N},z)}, \tag{2.99}$$

where the integration over z lies along the outgoing momentum $\vec{p}_N$.

In contrast to the Glauber eikonal phase, the optical potential eikonal phase of Eq. (2.99) depends solely on the coordinate $\vec{r}$ that defines the interaction point. As a consequence, it can be taken out of all the integrations in Eq. (2.12) and the cylindrical symmetry of the pion Glauber eikonal factor is retained, hereby considerably reducing the cost of computing the total FSI factor $\mathscr{F}_{\text{FSI}}$. For the numerical evaluation of the ROMEA phase factor, we made use of the proton-^{4}He optical potential of van Oers *et al.* [110]. The optical potential contains a Coulomb term, a central and l-dependent term with a Wood-Saxon form

factor and a spin-orbit term with a Thomas form factor. The $p-^4$He optical potential of Ref. [110] contains a total of 14 adjustable parameters that are determined by fitting ^{4}He(p,p) data for $85 \leq T_p \leq 580$ MeV. For heavier nuclei, we use the pA optical potentials as they were determined in the so-called global $(S-V)$ parametrization of Cooper *et al.* [79]. It uses the scalar-vector model of Eq. (2.93) with complex potentials containing a volume and a surface term. It serves proton energies from 20 to 1040 MeV for targets ^{12}C, ^{16}O. ^{40}Ca, ^{90}Zr and ^{208}Pb.

2.3 Color Transparency

We implement color transparency effects in the usual fashion by replacing the total cross sections σ_{iN}^{tot} in the profile functions of Eq. (2.88) with effective ones proposed by Farrar *et al.* [111]. The latter induce some reduced pion-nucleon and nucleon-nucleon interaction over a typical length scale l_h corresponding with the hadron formation length. As suggested by pQCD [112], the cross section is assumed to be scaled by the ratio of the transverse size of the quark system to the average size of the hadron $< b >$ ($i = \pi$ or N')

$$\sigma_{iN}^{\text{eff}} = \frac{b^2(\mathscr{Z})}{< b^2 >}\sigma_{iN}^{\text{tot}} \quad \text{for } z \leq l_h\,, \tag{2.100}$$

with $\mathscr{Z}$ the distance from the interaction point. At the point of interaction, the hadron is supposed to have a transverse area of $\frac{n^2<k_t^2>}{\mathscr{H}}$, where n is the number of elementary fields (2 for the pion, 3 for the nucleon), $k_t = 0.350$ GeV/c is the average transverse momentum of a quark inside a hadron, and $\mathscr{H}$ is the hard-scale parameter (or virtuality) that governs the CT effect. $\mathscr{H}$ equals the momentum transfer $t = (q^\mu - p_\pi^\mu)^2$ (pion CT) or $u = (q^\mu - p_N^\mu)^2$ (nucleon CT) for pion photoproduction (see Fig. 2.14) and Q^2 for pion electroproduction. To describe the expansion along the formation length l_h, two models are described in the work of Ref. [111]. The first is a naive model using partons with a relative velocity approaching the velocity of light. This gives us $b(\mathscr{Z}) \sim t \sim (E/m)^{-1}\mathscr{Z}$, with $(E/m)^{-1}$ the time-dilatation factor for the lab-frame. Based on semi-classical arguments, the formation length becomes $l_h = (E/m)^{-1}(\sigma_{iN}^{\text{tot}}/\pi)^{1/2}$. Inspired by pQCD, an alternate prescription to determine l_h is proposed stemming from a behaviour called *quantum diffusion*. It is theoretically justified for small times, when the transverse area of the system is small enough to apply the leading-logarithmic approximation to pQCD [23, 24]. Taking into account the asymptotically most important energy denominator in this leading-logarithmic approximation leads to $b^2 \sim \mathscr{Z}$. The formation length is determined by the time τ associated with the quantum fluctuation of the PLC to the normal hadron:

$$l_h \approx \tau \approx < \frac{1}{E_{\text{PLC}} - E_i} > \approx 2p/\Delta M^2\,, \tag{2.101}$$

with p the momentum of the final hadron and ΔM^2 the mass squared difference between the intermediate prehadron and the final hadron state. The value of ΔM^2 is an undetermined parameter and in itself a simplification of the process, as a process with high momentum transfer will produce a set of configurations of different masses. Theoretical arguments do not yield a consistent value for ΔM^2, but a lower limit can be placed e.g. for the nucleon by taking $m_N + m_\pi$ for the mass of the intermediate prehadron. This yields a value of $\Delta M^2 = 0.93$ GeV^2. In this work, we adopt the values $\Delta M^2 = 1$ GeV^2 for the proton and $\Delta M^2 = 0.7$ GeV^2 for the pion. Despite the fact that the order of magnitude of these values can be founded on very general principles, their precise values should be interpreted as educated guesses and their precise determination is awaiting experimental information, like nuclear transparency measurements.

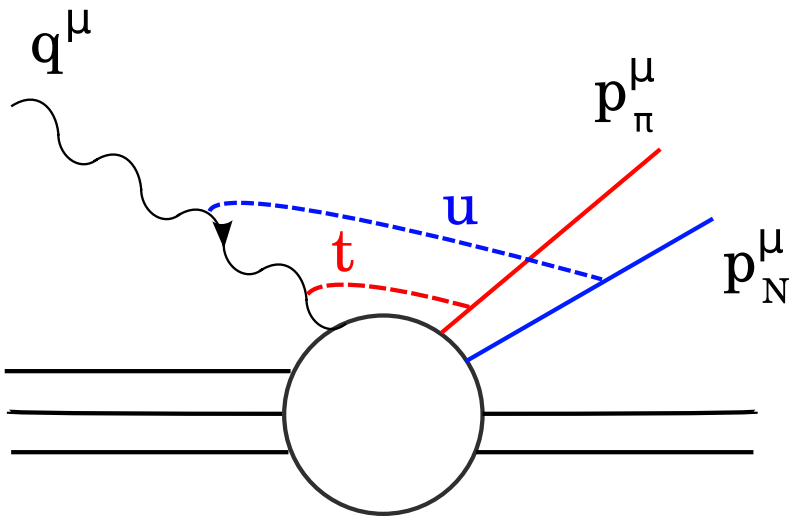

Figure 2.14 The virtuality that determines the formation length for the ejected nucleon (blue) and pion (red) in $A(\gamma, N\pi)$.

The arguments outlined above, lead us to the following formula for the effective cross sections used in the model:

$$\frac{\sigma_{iN}^{\text{eff}}}{\sigma_{iN}^{\text{tot}}} = \left\{ \left[\left(\frac{\mathscr{Z}}{l_h} \right)^{\tau} + \frac{< n^2 k_t^2 >}{\mathscr{H}} \left(1 - \left(\frac{\mathscr{Z}}{l_h} \right)^{\tau} \right) \right] \theta(l_h - \mathscr{Z}) + \theta(\mathscr{Z} - l_h) \right\} . \tag{2.102}$$

$\tau = 1$ corresponds to the quantum diffusion model, $\tau = 2$ to the naive parton model. Figure 2.15 illustrates the predicted difference of the CT effect on the pion-nucleon and nucleon-nucleon effective interaction. Reflecting its mesonic nature, the pion has a longer formation length and during its formation its interaction cross section with the residual nucleons is more strongly reduced than for a nucleon.

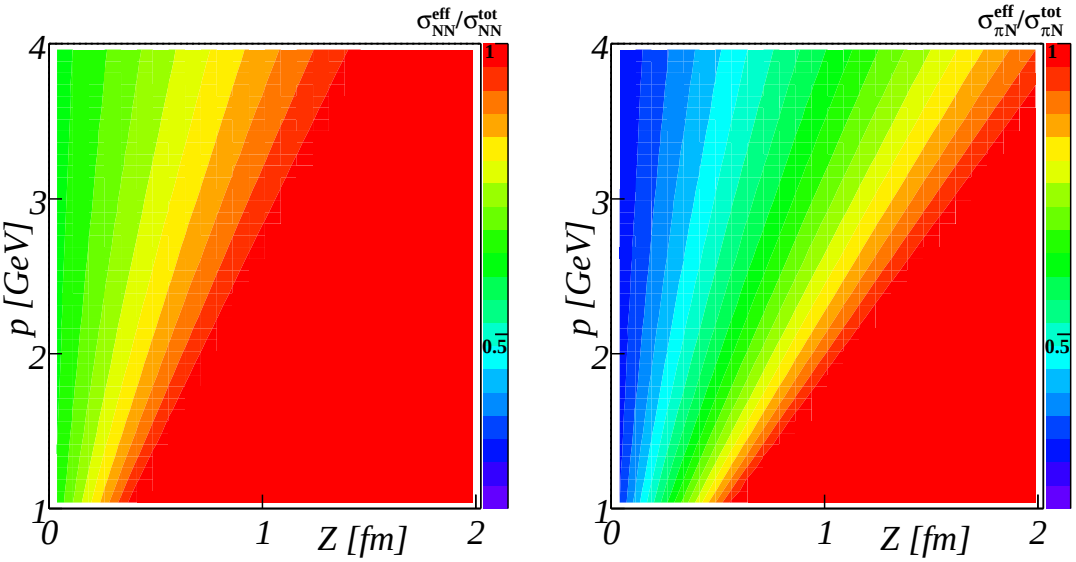

Figure 2.15 Comparison of the CT effect on the total effective cross section $\sigma^{\rm eff}_{iN}$ for nucleon-nucleon (left panel) and pion-nucleon (right panel) interactions. We consider the situations whereby the ejectile possesses a lab momentum from 1 to 4 GeV/c. For the hard-scale parameter we adopt $\mathscr{H} = 1.8$ (GeV/c)^2.

Another recipe for the effective cross section $\sigma^{\rm eff}_{NN}$, proposed by Jennings and Miller [113, 114], is based on a hadronic basis and computes the relevant matrix elements of $\sigma(b^2)$ in a harmonic oscillator basis. The PLC is considered as a superposition of the nucleon ground state and a resonance, and the effective cross section is given by

$$\sigma^{\rm eff}_{NN}(\mathscr{Z}) = \sigma^{\rm tot}_{NN}(1 - e^{-i\mathscr{Z}/\tau}), \tag{2.103}$$

with τ determined with Eq. (2.101), and ΔM taken from the mass difference with the lowest radial excitation of the ground state in the harmonic oscillator basis. This model was later extended with a sum-rule approach to expand the PLC in a complete set of intermediate states [115, 116]. It uses measured matrix elements for deep-inelastic scattering and diffractive dissociation to represent the hard and soft scattering operator needed in the evaluation of $\sigma^{\rm eff}_{NN}$, respectively. In this approach, the effective cross section becomes

$$\sigma^{\rm eff}_{NN}(\mathscr{Z}) = \int_{(m_N+m_\pi)^2}^{\infty} dM_X^2 \rho(M_X^2, Q^2) \left(1 - e^{-i(M_X^2 - m_N^2)\mathscr{Z}/2p}\right), \tag{2.104}$$

with ρ representing the product of the above-mentioned measured matrix elements. For small values of $\mathscr{Z}$, Eq. (2.104) is approximately linear in $\mathscr{Z}$. For electroproduction of vector mesons on nuclei, work has been done in a model based on a light-cone QCD Green's function formalism [117–119] and calculations have been done for ϕ and ρ production [120–123].

For the calculations reported in this thesis, we have adopted the quantum diffusion model of Farrar *et al*.

2.4 Short-Range Correlations

We now proceed with introducing a method that allows us to implement the effect of SRC in the relativistic Glauber calculations. The proposed method adopts the thickness approximation as a starting point. In the thickness approximation, the density $\left|\phi_{\alpha_i}(\vec{r}_i)\right|^2$ of the individual nucleons in Eq. (2.12) is replaced by an averaged density $\rho_A^{[1]}(\vec{r})$ defined as

$$\rho_A^{[1]}(\vec{r}) = A \int d\vec{r}_2 \ldots \int d\vec{r}_A \left(\Psi_A^{\text{g.s.}}(\vec{r},\vec{r}_2,\ldots,\vec{r}_A)\right)^\dagger \Psi_A^{\text{g.s.}}(\vec{r},\vec{r}_2,\ldots,\vec{r}_A). \tag{2.105}$$

In terms of $\rho_A^{[1]}(\vec{r})$ the FSI factor of Eq. (2.12) can be approximated by

$$\mathscr{F}_{\text{FSI}}^{\text{thick}}(\vec{r}) = \frac{1}{A^{A-1}} \int d\vec{r}_2 \ldots \int d\vec{r}_A \rho_A^{[1]}(\vec{r}_2)\rho_A^{[1]}(\vec{r}_3)\ldots\rho_A^{[1]}(\vec{r}_A) \hat{\mathscr{S}}_{\pi N}(\vec{r};\vec{r}_2,\ldots,\vec{r}_A)\hat{\mathscr{S}}_{N'N}(\vec{r};\vec{r}_2,\ldots,\vec{r}_A) \tag{2.106}$$

In combination with the operators of Eq. (2.91) the expression can be further simplified to

$$\begin{aligned}\mathscr{F}_{\text{FSI}}^{\text{thick}}(\vec{r}) = &\left(\int d\vec{r}_2 \frac{\rho_A^{[1]}(\vec{r}_2)}{A}\left[1-\Gamma_{N'p}(\vec{b}_{N'}-\vec{b}_{N'2})\theta(z_{N'2}-z_{N'})\right]\right.\\ &\left.\left[1-\Gamma_{\pi p}(\vec{b}_\pi-\vec{b}_{\pi 2})\theta(z_{\pi 2}-z_\pi)\right]\right)^{Z-\frac{\tau_z+1}{2}}\\ &\times\left(\int d\vec{r}_3 \frac{\rho_A^{[1]}(\vec{r}_3)}{A}\left[1-\Gamma_{N'n}(\vec{b}_{N'}-\vec{b}_{N'3})\theta(z_{N'3}-z_{N'})\right]\right.\\ &\left.\left[1-\Gamma_{\pi n}(\vec{b}_\pi-\vec{b}_{\pi 3})\theta(z_{\pi 3}-z_\pi)\right]\right)^{N+\frac{\tau_z-1}{2}},\end{aligned} \tag{2.107}$$

where τ_z is the isospin (1 for protons and -1 for neutrons) of the nucleon on which the initial absorption took place. The $z_{N'}$ (z_π) axis lies along the ejected nucleon (pion). The above expression is derived within the context of the IPM. It is clear that the nucleus has a fluid nature and that the IPM can only be considered as a first-order approximation. In computing the FSI effects by means of the Eq. (2.107) one fails to give proper attention to one important piece of information: namely that one considers the density distribution of nucleons given that there is one present at the photo-interaction point $\vec{r}$.

The two-body density $\rho_A^{[2]}(\vec{r}_1,\vec{r}_2)$ is related to the probability to find a nucleon at position $\vec{r}_2$ given that there is one at a position $\vec{r}_1$. We adopt the following normalization

convention for $\rho_A^{[2]}$

$$\int d\vec{r}_1 \int d\vec{r}_2 \rho_A^{[2]}(\vec{r}_1,\vec{r}_2) = A(A-1)\,. \tag{2.108}$$

In the IPM on has $\left[\rho_A^{[2]}(\vec{r}_1,\vec{r}_2)\right]_{\rm IPM} \equiv \frac{A-1}{A}\rho_A^{[1]}(\vec{r}_1)\rho_A^{[1]}(\vec{r}_2)$. The nucleus has a granular structure as the nucleons have a finite size. This gives rise to strong nucleon-nucleon repulsions at short internucleon distances that reflect themselves in SRC at the nuclear scale. One can correct $\left[\rho_A^{[2]}(\vec{r}_1,\vec{r}_2)\right]$ for the presence of the SRC by adopting the following functional form [124]

$$\rho_A^{[2]}(\vec{r}_1,\vec{r}_2) \equiv \gamma(\vec{r}_1)\left(\rho_A^{[2]}(\vec{r}_1,\vec{r}_2)\right)_{\rm IPM}\gamma(\vec{r}_2)g(r_{12}) = \frac{A-1}{A}\gamma(\vec{r}_1)\rho_A^{[1]}(\vec{r}_1)\rho_A^{[1]}(\vec{r}_2)\gamma(\vec{r}_2)g(r_{12}), \tag{2.109}$$

with $g(r_{12})$ the so-called Jastrow correlation function and $\gamma(\vec{r})$ a function that imposes the normalization condition of Eq. (2.108) on $\rho_A^{[2]}(\vec{r}_1,\vec{r}_2)$. The function $\gamma(\vec{r})$ is a solution to the following integral equation

$$\gamma(\vec{r}_1)\int d\vec{r}_2\rho_A^{[1]}(\vec{r}_2)g(r_{12})\gamma(\vec{r}_2) = A, \tag{2.110}$$

which can be solved numerically. The Glauber phase factor of Eq. (2.107) can now be corrected for SRC through the following substitution

$$\rho_A^{[1]}(\vec{r}_2) \to \frac{A}{A-1}\frac{\rho_A^{[2]}(\vec{r}_2,\vec{r})}{\rho_A^{[1]}(\vec{r})} = \gamma(\vec{r}_2)\rho_A^{[1]}(\vec{r}_2)\gamma(\vec{r})g(|\vec{r}_2-\vec{r}|) \equiv \rho_A^{\rm eff}(\vec{r}_2,\vec{r})\,, \tag{2.111}$$

whereby $\rho_A^{[2]}(\vec{r}_2,\vec{r})$ adopts the expression (2.109). These manipulations amount to the following final expression for the Glauber FSI factor including SRC:

$$\begin{aligned}\mathscr{F}_{\rm FSI}^{\rm SRC}(\vec{r}) = &\left(\int d\vec{r}_2 \frac{\gamma(\vec{r}_2)\rho_A^{[1]}(\vec{r}_2)\gamma(\vec{r})g(|\vec{r}_2-\vec{r}|)}{A}\right.\\ &\left.\times\left[1-\Gamma_{N'p}(\vec{b}_{N'}-\vec{b}_{N'2})\theta(z_{N'2}-z_{N'})\right]\left[1-\Gamma_{\pi p}(\vec{b}_\pi-\vec{b}_{\pi 2})\theta(z_{\pi 2}-z_\pi)\right]\right)^{Z-\frac{\tau_z+1}{2}}\\ &\times\left(\int d\vec{r}_3\frac{\gamma(\vec{r}_3)\rho_A^{[1]}(\vec{r}_3)\gamma(\vec{r})g(|\vec{r}_3-\vec{r}|)}{A}\left[1-\Gamma_{N'n}(\vec{b}_{N'}-\vec{b}_{N'3})\theta(z_{N'3}-z_{N'})\right]\right.\\ &\left.\times\left[1-\Gamma_{\pi n}(\vec{b}_\pi-\vec{b}_{\pi 3})\theta(z_{\pi 3}-z_\pi)\right]\right)^{N+\frac{\tau_z-1}{2}}.\end{aligned} \tag{2.112}$$

The effective density of Eq. (2.111) accounts for the fact that the motion of each nucleon does depend on the presence of the other ones. In fig. 2.16 we display the effective nuclear

density as it would be observed by a nucleon or a pion created after photoabsorption on a nucleon at the center of the nucleus. The figure shows the density for Fe as computed in the IPM $[\rho_A^{[1]}(x,y,z\equiv 0)]$ and with the expression based on the substitution of Eq. (2.111)

$$\gamma(x,y,z\equiv 0)\rho_A^{[1]}(x,y,z\equiv 0)\gamma(x\equiv 0,y\equiv 0,z\equiv 0)g(|\vec{r}|)\,.$$

In Fig. 2.16 and all forthcoming numerical calculations we use a correlation function $g(|\vec{r}|)$ from Ref. [94]. It is characterized by a (Gaussian) hard core of about 0.8 fm and a second bump that extends to internucleon distances r of about 2 fm and reaches its maximum for $r_{12}\approx 1.3$ fm. This correlation function provided a fair description of the SRC contributions to ^{12}C$(e,e'pp)$ [125] and ^{16}O$(e,e'pp)$ [86] (Fig. 2.5). It is clear that the SRC lead to a local reduction - with size of the nucleon radius - of the density around the nucleon struck by the (virtual) photon. To preserve the proper normalization, this reduction amounts to some enhanced density at distances of about twice the nucleon radius. With regard to the intranuclear attenuation, the reduction of the density in the proximity of the struck nucleon will result in some enhanced transparency close to the photointeraction point $\vec{r}$. The enhanced density at positions of about twice the nucleon radius from the struck nucleon, can be expected to have the opposite effect.

At the moment the model does not include tensor correlations, believed to be the main source of the difference in abundance of observed $p-p$ and $n-p$ pairs. If we take a look at the values of the slope parameter β_{iN}, we observe that a typical value of β_{iN} for a particle in the GeV momentum range is smaller than 0.5 fm. As this parameter provides a measure of the transverse range of the attenuation by the nuclear medium, we anticipate the effects of including tensor correlations (who operate at larger distances) in the Glauber model will be a lot smaller than those caused by SRC.

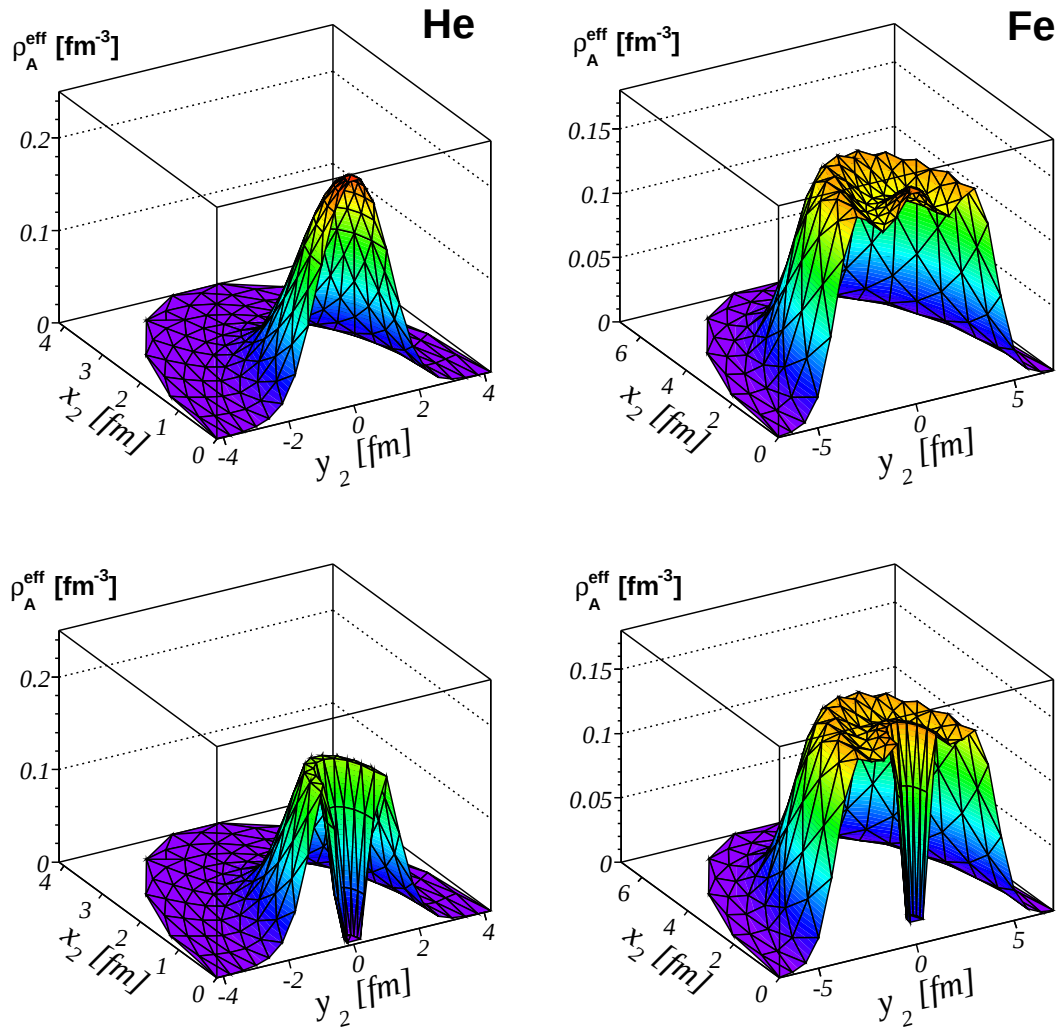

Figure 2.16 The effective nuclear density $\rho_A^{\rm eff}(\vec{r}_2, \vec{r})$ at $z_2 = 0$ for He (left) and Fe (right) before (upper) and after (lower panel) the inclusion of SRC effects. The effective nuclear densities here refer to the situation whereby the (virtual) photon is absorbed at the origin $(x = 0, y = 0, z = 0)$.

Chapter 3

Numerical Results

This chapter presents the results of the numerical calculations using the model outlined in chapter 2. We start with an analysis of the FSI factor of a reaction with two ejected particles and show the effects of the attenuation mechanisms on the momentum distributions for pion-nucleon and two nucleon removal reactions in several nuclei. Sec. 3.3 presents transparency calculations for pion photo- and electroproduction and two nucleon knockout reactions. The influence of adding short-range correlations and color transparency to the transparency calculations is investigated and the hard-scale dependence of the two effects is determined. For the pion removal reaction, comparisons are made with data taken at Jefferson Lab and other models, both semiclassical and quantummechanical. We also take a closer look at the A-dependence of the pion electroproduction reaction. Subsequently, transparency calculations for the $A(\gamma, pp)$ reaction gives us an opportunity to compare the competing reaction mechanisms outlined in sec. 2.1.3. We conclude the chapter by comparing the density dependences of removal reactions involving one, two and three nucleons.

3.1 The FSI factor

In this subsection we present a selected number of results of the numerical calculations of the RMSGA FSI factor of Eq. (2.12). We consider the $^{12}\mathrm{C}(\gamma, p\pi^-)$ reaction in a reference frame with the z axis along the momentum $\vec{p}_N$ of the ejected nucleon and the y axis along $\vec{p}_\pi \times \vec{p}_N$ (with $\vec{p}_\pi$ in the lower hemisphere). In what follows, $\theta_{N\pi}$ stands for the angle of the pion relative to the nucleon. It has a negative value in all calculations considered in this section. The coordinate $\vec{r}$ denotes the interaction point with the external photon. A sketch of this situation is presented in Fig. 3.1. We present the FSI factor versus the spherical coordinates in this frame. The general conclusions and the trends of this discussion can be straightforwardly generalized to the situation of two hadrons in the final state (either two

nucleons, two pions or a nucleon and a pion).

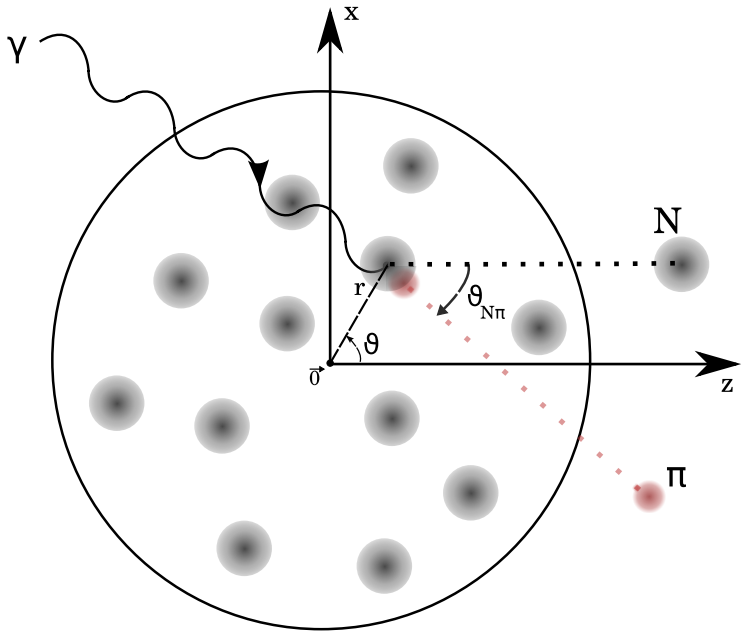

Figure 3.1 Sketch of the coordinates, choice of axes and $\theta_{N\pi}$ for the presentation of the $^{12}C(\gamma, p\pi^-)$ FSI factor. r denotes the distance of the interaction point to the center of the nucleus and $theta$ the angle with the z axis, taken parallel to the momentum of the ejected nucleon.

In fig. 3.2, we present the calculated norm and phase of the FSI factor in the scattering plane ($\phi = 0$) for $p_N \approx 2.6$ GeV and $p_\pi \approx 2.3$ GeV, which are conditions for which Jefferson Lab collected data [47]. We present the FSI factor for the proton and the pion separately as well as the combined effect when the two are detected in coincidence.

When looking at the θ dependence, it becomes clear from Fig. 3.2 that the norm is smallest in the direction opposite the momentum of the particle (being 180° for the nucleon and $180° + \theta_{N\pi}$ for the pion). For these directions and large r, the nucleon or pion is created close to the surface of the nucleus on the opposite side of its asymptotic direction and has to travel through a thick layer of nuclear medium before it reaches the detectors. As for the r dependence, we see for the nucleon a reduction of the FSI effects for rising r at angles in the neighborhood of $\theta = 0°$, and respectively an increment for rising r at $\theta = 180°$. This is again due to the fact that the outgoing nucleon traverses less, respectively more nuclear matter on its way out of the nucleus. The same observations apply for the pion, albeit at the angles $\theta_{N\pi}$ and $180° + \theta_{N\pi}$. The total FSI factor combines the intranuclear attenuation effects on the nucleon and pion. Hence, the norm shows the largest reduction at θ around 180° and $180° + \theta_{N\pi}$. The phase of the FSI factor exhibits similar behavior, with the largest phase shifts occurring at the discussed angles.

Figure 3.3 teaches us a couple things about the ϕ dependence of the FSI factor. As

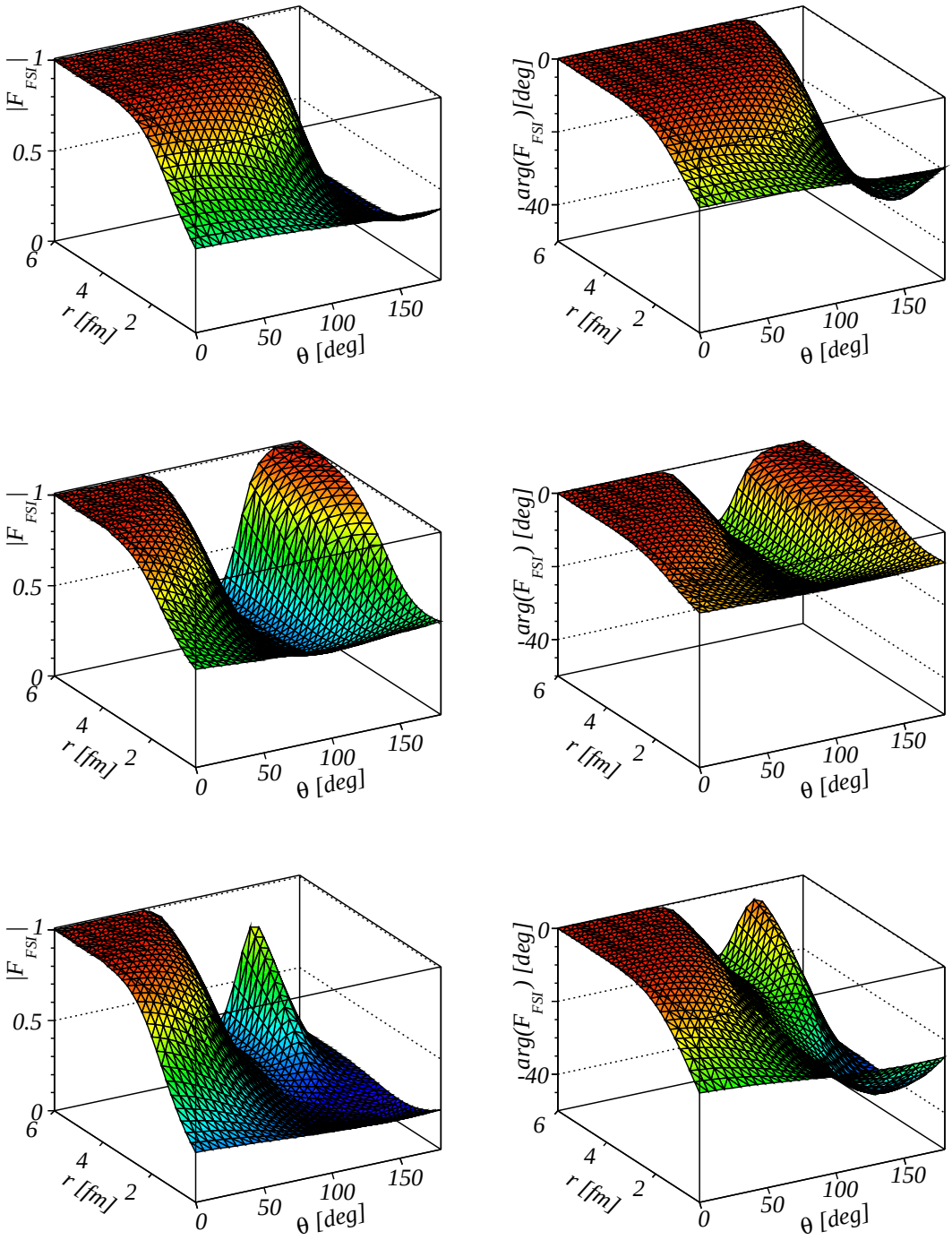

Figure 3.2 Radial and polar-angle dependence of the norm (left) and phase (right) of the FSI factor $\mathcal{F}_{\rm FSI}$ in the scattering plane ($\phi = 0°$) for the ^{12}C$(\gamma, p\pi^-)$ reaction from the $1s_{1/2}$ level. For the upper (middle) panels, solely the FSI effects on the ejected proton (pion) are considered. The lower panels include the net effect of both the pion and nucleon FSI effect. The results are obtained for $p_N = 2638$ MeV, $p_\pi = 2291$ MeV, $\theta_{N\pi} = -65.19°$.

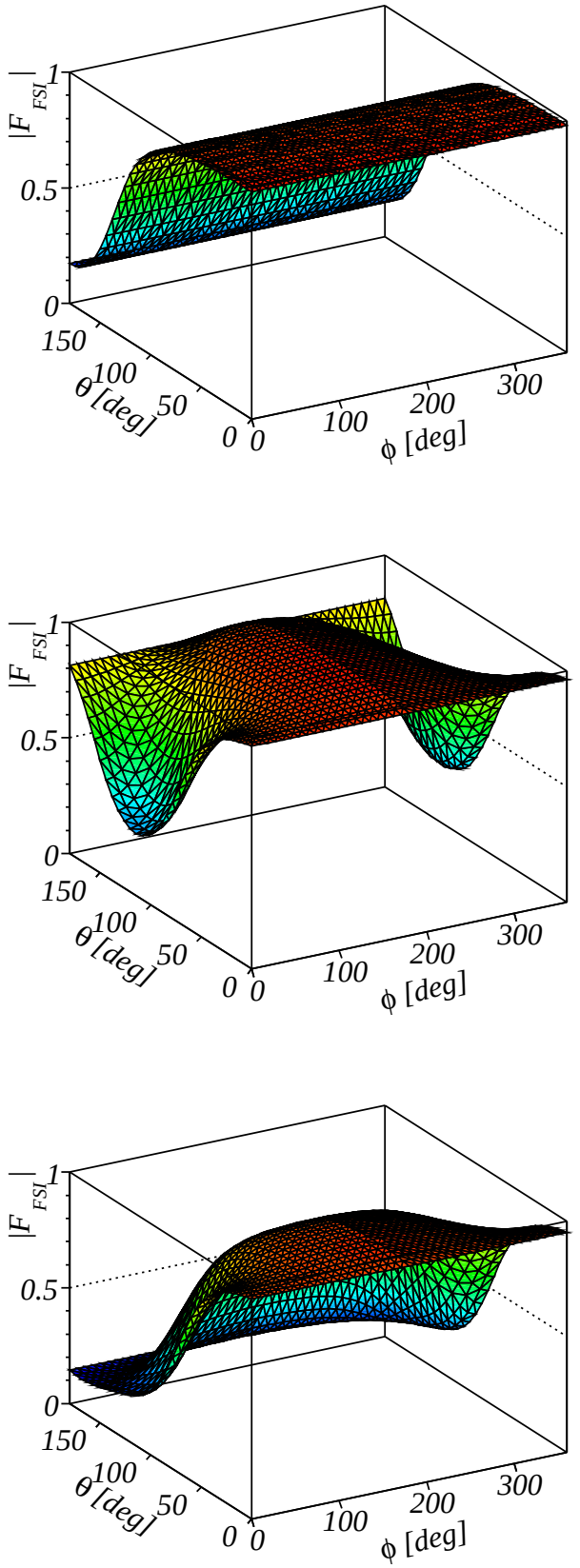

Figure 3.3 Polar- and azimuthal-angle dependence of the norm of the FSI factor $\mathscr{F}_{\rm FSI}$ at a distance $r = 3$ fm from the center of the nucleus for the ^{12}C$(\gamma, p\pi^-)$ reaction from the $1s_{1/2}$ level. Separate contributions from the nucleon (upper panel) and the pion (middle panel), as well as their combined effect (bottom panel), are shown. Kinematics as in Fig. 3.2.

the outgoing nucleon lies along the z axis there is no dependence on the azimuthal angle because of the cylindrical symmetry. Again, we can see that the absorption is largest when large amounts of nuclear matter need to be traversed (i.e., large θ). Looking at the pion we see the largest attenuation occurs in the upper hemisphere ($\cos\phi \geq 0$) as a pion that is created in this region has to traverse the inner core of the nucleus. The combined effect of the pion and nucleon contributions is contained in the bottom panel. As the reaction takes place in the xz plane, the total FSI factor retains the following symmetry: $\mathcal{F}_{\rm FSI}(r,\theta,\phi) = \mathcal{F}_{\rm FSI}(r,\theta,2\pi-\phi)$.

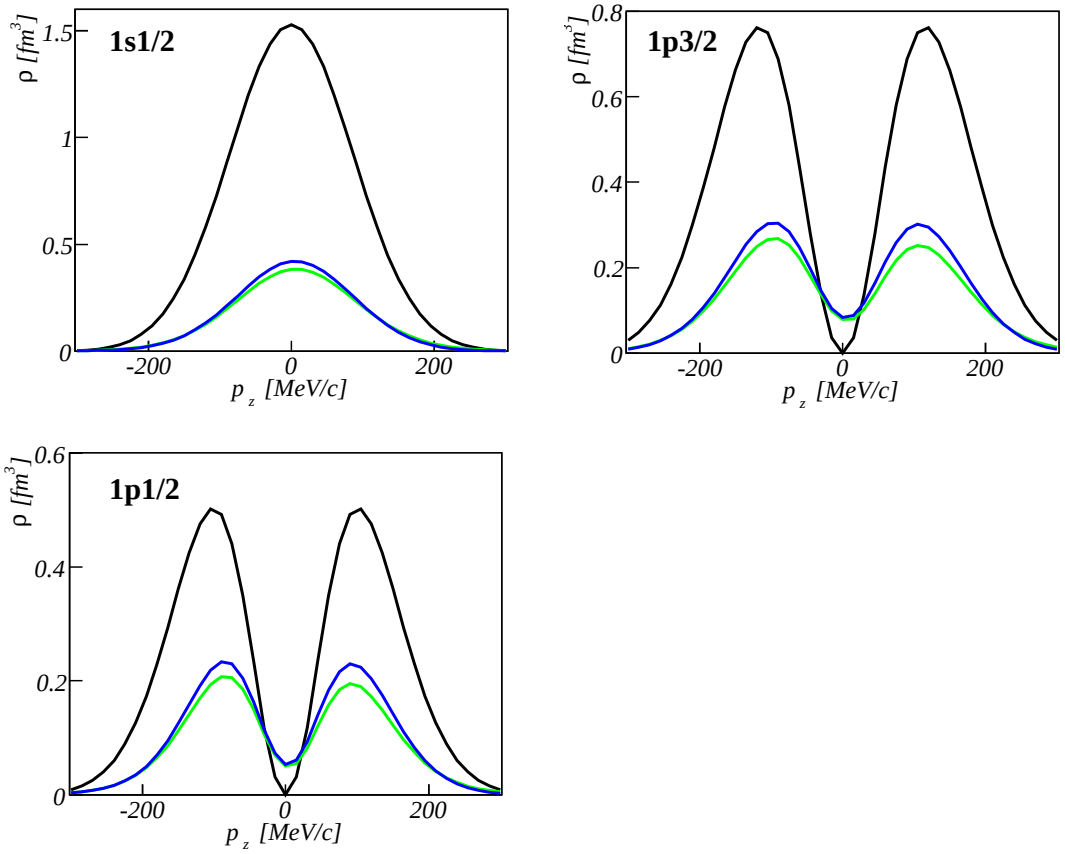

Figure 3.4 Momentum distributions for neutron knockout from the $1s1/2$ (left), $1p3/2$ (middle) and $1p1/2$ shell (right panel) in the ^{16}O$(\gamma, p\pi^-)$ reaction with an incident photon energy of 3 GeV and the pion c.m. angle $\theta^{\pi}_{\rm c.m.} = 90°$. Black curves are RPWIA calculations, blue includes Glauber FSI and green curves include CT effects to the Glauber FSI.

3.2 Momentum Distributions

The attenuation mechanisms of the nuclear medium reflect themselves in distortions of the momentum distributions which translates to the inclusion of the FSI factor in Eq. (2.29).

In Fig. 3.4, we have plotted the momentum distributions with and without FSI and CT for the ^{16}O$(\gamma, p\pi^-)$ reaction with an incident photon energy of 3 GeV and the pion c.m. angle $\theta^{\pi}_{\text{c.m.}} = 90°$. The strength of the distorted momentum distribution without CT is reduced by the largest amount in the respective maxima of the distributions and evaluates to 25 % for the $1s1/2$, 32 % for the $1p3/2$, and 40 % for the $1p1/2$ shell. The shell dependence of the transparency is caused by the differences in density distribution for the different shells. The density distribution of the $1s1/2$ shell is largest in the center of the nucleus. Hence nucleons knocked out from this shell will on average have to transverse more nuclear matter than their counterparts in the $1p3/2$ and $1p1/2$ shells. The FSI also shift the minimum at $p = 0$ for the p-shells to higher values in the distorted momentum distributions.

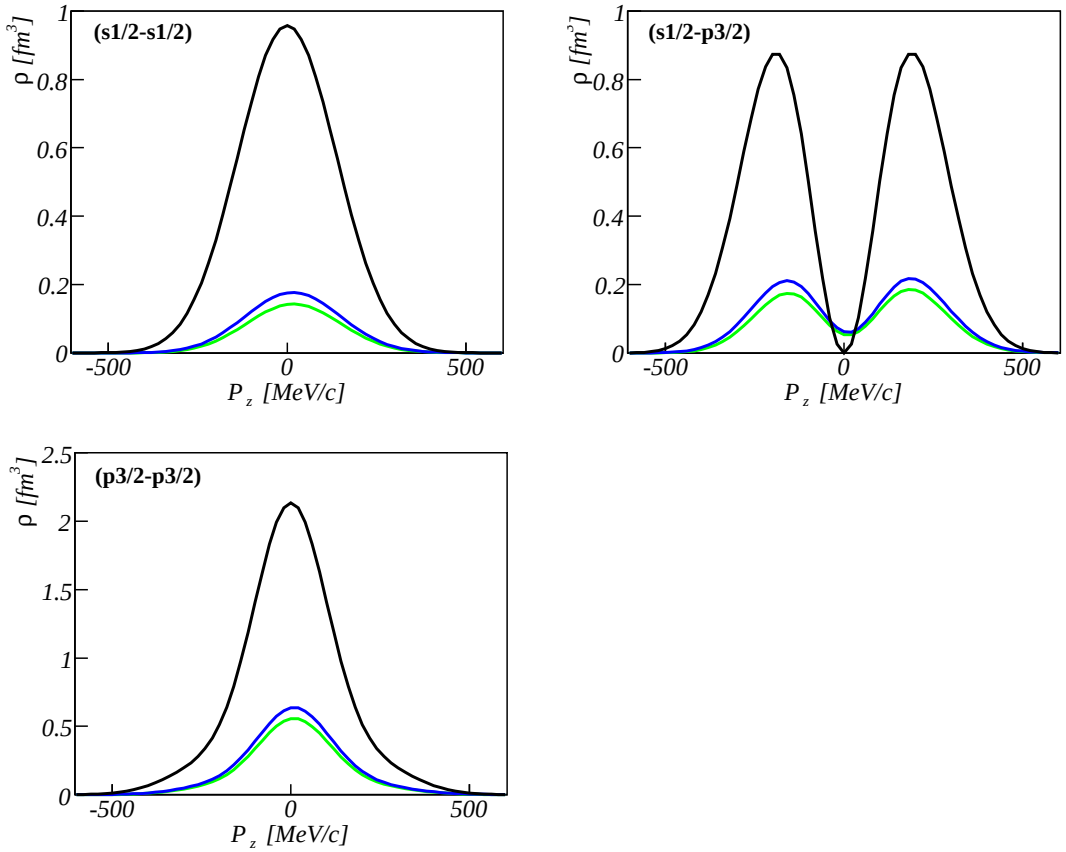

Figure 3.5 Momentum distributions for double proton knockout from the $(1s1/2 - 1s1/2)$- (left), $(1s1/2 - 1p3/2)$- (middle) and $(1p3/2 - 1p3/2)$-orbits (right panel) in the ^{12}C(γ, pp) reaction with an incident photon energy of 3 GeV and coplanar symmetric kinematics (situation shown in Fig. 3.7). Black curves are RPWIA calculations, green includes Glauber FSI and blue curves include CT effects to the Glauber FSI.

We can also formulate a momentum distribution related to Eq. (2.29) for the nucleon-

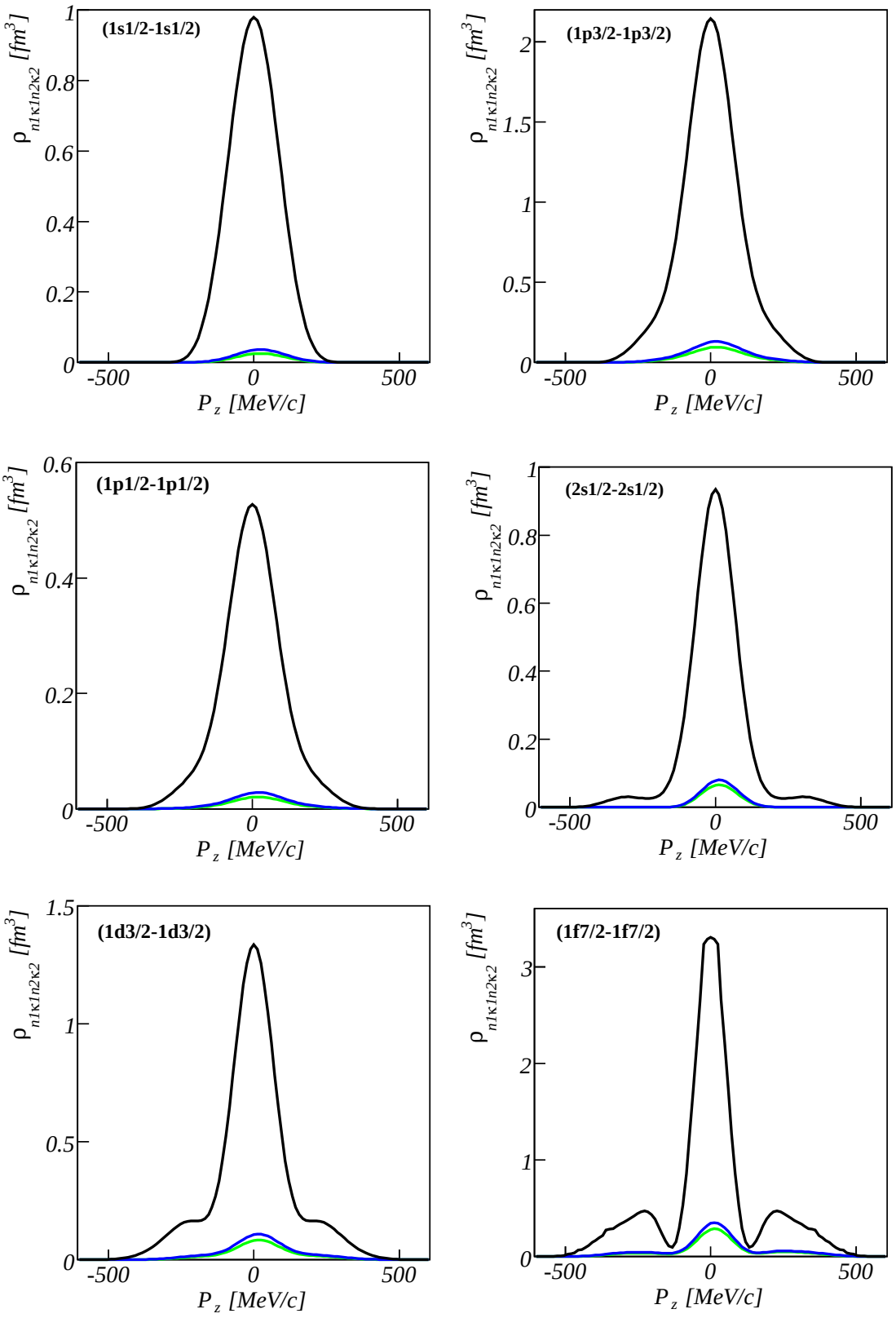

Figure 3.6 Momentum distributions for double proton knockout from a selection of shell combinations in the ^{56}Fe(γ, pp) reaction with an incident photon energy of 4 GeV and coplanar symmetric kinematics for the outgoing protons. Black curves are RPWIA calculations, green includes Glauber FSI and blue curves include CT effects to the Glauber FSI.

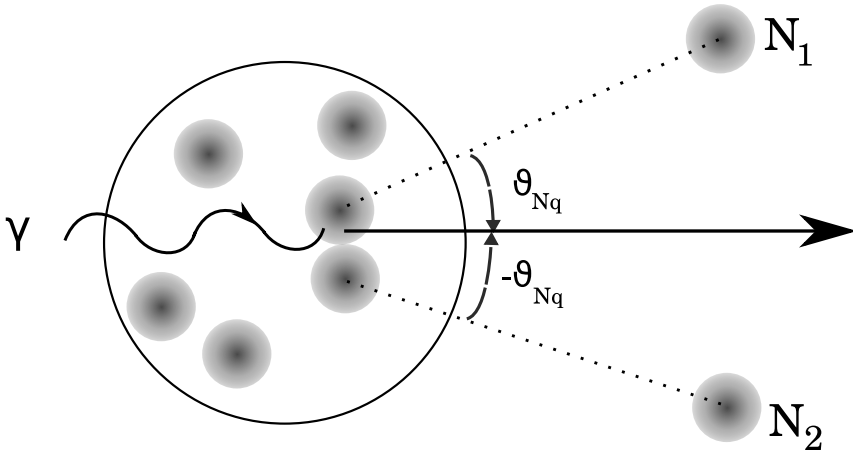

Figure 3.7 The $A(\gamma, N_1N_2)$ reaction in coplanar and symmetric kinematics. The two escaping nucleons N_1 and N_2 have the same energy and polar angle θ_{Nq}, but escape from the opposite side of $\vec{q}$.

nucleon pair in a relative S-state of sec. 2.1.3:

$$\rho^D_{n_1\kappa_1 n_2\kappa_2}(\vec{P},\vec{p}) = \frac{1}{(2\pi)^6}\sum_{s_1,s_2,m_1,m_2}\left|\int d\vec{R}e^{-i\vec{P}\cdot\vec{R}}\int d\vec{r}e^{-i\vec{p}\cdot\vec{r}}g(\vec{r})\right.$$
$$\left.\times\bar{u}(\frac{\vec{P}}{2}+\vec{p},s_1)\phi_{n_1\kappa_1 m_1}(\vec{R})\bar{u}(\frac{\vec{P}}{2}-\vec{p},s_2)\phi_{n_2\kappa_2 m_2}(\vec{R})\mathcal{F}_{\rm FSI}(\vec{R})\right|^2, \quad (3.1)$$

with notations as in sec. 2.1.3. $\mathcal{F}_{\rm FSI}(\vec{R})$ is the FSI factor of Eqs. (2.54) and (2.55), and $(n_i\kappa_i m_i)$ denote the quantum numbers of the ejected nucleons. By neglecting the lower components of the positive-energy projections in Eq. (3.1), we can separate $\rho^D_{n_1\kappa_1 n_2\kappa_2}(\vec{P},\vec{p})$ in a part containing the relative pair momentum and a part containing the c.m. motion. With the notations of Eqs. (2.58) and (2.59):

$$\rho^D_{n_1\kappa_1 n_2\kappa_2}(\vec{P},\vec{p}) \approx g(\vec{p})\frac{1}{(2\pi)^6}\sum_{s_1,s_2,m_1,m_2}\left|\eta^D_{n_1\kappa_1 m_1 n_2\kappa_2 m_2}(\vec{P})\right|^2 \equiv g(\vec{p})\rho^D_{n_1\kappa_1 n_2\kappa_2}(\vec{P}) \quad (3.2)$$

Fig. 3.5 shows the c.m. momentum distribution $\rho^D_{n_1\kappa_1 n_2\kappa_2}(\vec{P})$ for all possible shell combinations in the ^{12}C(γ,pp) reaction for a photon energy of 4 GeV and coplanar symmetric kinematics. The strength is reduced at the distribution maxima to 15% for the $(1s1/2-1s1/2)$-orbits, 21% for the $(1s1/2-1p3/2)$-orbits, and 26% for the $(1p3/2-1p3/2)$-orbits. Fig. 3.6 also depicts momentum distributions for a selection of shell combinations in the ^{56}Fe(γ,pp) reaction highlighting the big reduction of the distributions in a large nucleus.

3.3 Transparencies

3.3.1 Pion Photoproduction

The experiment E94-104 at Jefferson Lab extracted nuclear transparencies for the process $\gamma + {}^4\text{He} \rightarrow p + \pi^- + {}^3\text{He}$. The measurements were performed for photon energies $1.6 \leq q \leq 4.2$ GeV and for $\theta^{\pi}_{\text{c.m.}} = 70°$ and $90°$, with $\theta^{\pi}_{\text{c.m.}}$ the center-of-mass angle between the photon and pion. In total, the nuclear transparencies were measured for eight kinematical settings. In a proposal for a follow-up experiment, seven additional kinematics are suggested for measurements at higher photon energies and $\theta^{\pi}_{\text{c.m.}} = 90°$ [126]. We have performed calculations for the completed and planned experiments. Table 3.1 provides a list of the kinematics.

q [MeV]	$\theta^{\pi}_{\text{c.m.}}$ [deg]	p_N [MeV]	θ_N [deg]	p_π [MeV]	θ_π [deg]
1648	70°	989	47.39°	1238	−36.02°
1648	90°	1277	37.37°	1015	−47.73°
2486	70°	1322	44.37°	1794	−31.02°
2486	90°	1740	34.45°	1438	−43.18°
3324	70°	1642	41.74°	2363	−27.56°
3324	90°	2195	32.01°	1866	−38.57°
4157	70°	1949	39.51°	2929	−25.05°
4157	90°	2638	30.01°	2291	−35.18°
4327	70°	2011	39.1°	3044	−24.6°
4327	90°	2727	29.6°	2377	−34.6°
5160	70°	2307	37.3°	3606	−22.8°
5160	90°	3161	28.0°	2797	−32.1°
6059	70°	2622	35.6°	4211	−21.2°
6059	90°	3625	26.6°	3250	−29.9°
7025	70°	2956	33.9°	4861	−19.8°
7025	90°	4120	25.2°	3735	−28.0°
8057	70°	3309	32.4°	5555	−18.6°
8057	90°	4646	24.0°	4253	−26.3°
9156	70°	3683	31.0°	6294	−17.6°
9156	90°	5204	22.8°	4805	−24.8°
10322	70°	4077	29.7°	7077	−16.6°
10322	90°	5794	21.8°	5389	−23.5°

Table 3.1 Kinematics used in the completed and planned pion photoproduction transparency experiments. Central values for the photon energy (MeV), proton momentum p_N (MeV), proton angle θ_N, pion momentum p_π (MeV) and pion angle θ_π for $\theta^{\pi}_{\text{c.m.}} = 70°, 90°$. Angles are measured relative to the incoming photon momentum.

We aim at performing calculations that match the kinematic conditions of the experi-

ment as closely as possible. We use the following definition for the transparency:

$$T = \frac{\sum_\alpha \int dq Y(q) \int d\vec{p}_m \left(\frac{d^5\sigma}{dE_\pi d\Omega_\pi d\Omega_N}\right)_{\text{RMSGA}}}{\sum_\alpha \int dq Y(q) \int d\vec{p}_m \left(\frac{d^5\sigma}{dE_\pi d\Omega_\pi d\Omega_N}\right)_{\text{RPWIA}}} \ . \tag{3.3}$$

The integrations $\int dq \int d\vec{p}_m$ in Eq. (3.3) were evaluated with a Monte-Carlo integration algorithm. To this end, random events within the photon beam energy range, detector acceptances and applied cuts for each data point were generated for the calculation of the transparency until convergence of the order of 5% was reached. Typically, this involves about 1000 events for each data point. In Eq. (3.3), $\sum_\alpha$ extends over all occupied single-particle states in the target nucleus. All cross sections are computed in the laboratory frame. $Y(q)$ provides the weight factor for the generated events. It includes the yield of the reconstructed experimental photon beam spectrum [47] for the photon energy of the generated event. We assume that the elementary $\gamma + n \to \pi^- + p$ cross section $\frac{d\sigma^{\gamma\pi}}{d|t|}$ in Eqs. (2.28) and (2.30) remains constant over the kinematical ranges $\int dq \int d\vec{p}_m$ that define a particular data point. With this assumption the cross section $\frac{d\sigma^{\gamma\pi}}{d|t|}$ cancels out of the ratio (3.3). For all kinematic conditions of Table 3.1, the pion and nucleon momenta are sufficiently high for the RMSGA method to be a valid approach for describing the FSI mechanism.

In Fig. 3.8, we present the results of transparency calculations for ^{4}He together with the experimental data and the predictions of the semiclassical model of Ref. [127]. The computed RMSGA nuclear transparencies are systematically about 10% larger than the ones obtained in the semiclassical model. As can be appreciated from Fig. 3.8, the RMSGA calculations predict comparable CT effects as the semiclassical calculations shape. We have to stress though that the calculations with CT are normalized to the calculations without CT for the data point with the lowest $|t|$ in the semiclassical model. We did not perform this normalization for our calculations. Our results without color transparency are in better agreement with the experimental results than those with CT effects included. This is in disagreement with the semiclassical model whose results with CT effects are in better agreement with the experimental data. We also have to point out that, although the calculations with CT effects overestimate the experimental results for all data points, the slope of this curve shows better agreement with the slope of the data than the slope of the curves without CT effects.

As can be seen in Fig. 3.8, our model predicts a rise in the transparency for $|t| \leq 1.2$ GeV^2. In Fig. 3.9 the separated transparencies of the outgoing proton and pion are displayed next to the full result for the kinematics that data were taken for. It is clear from this figure that the rise of the transparency at low $|t|$ can be attributed to the proton

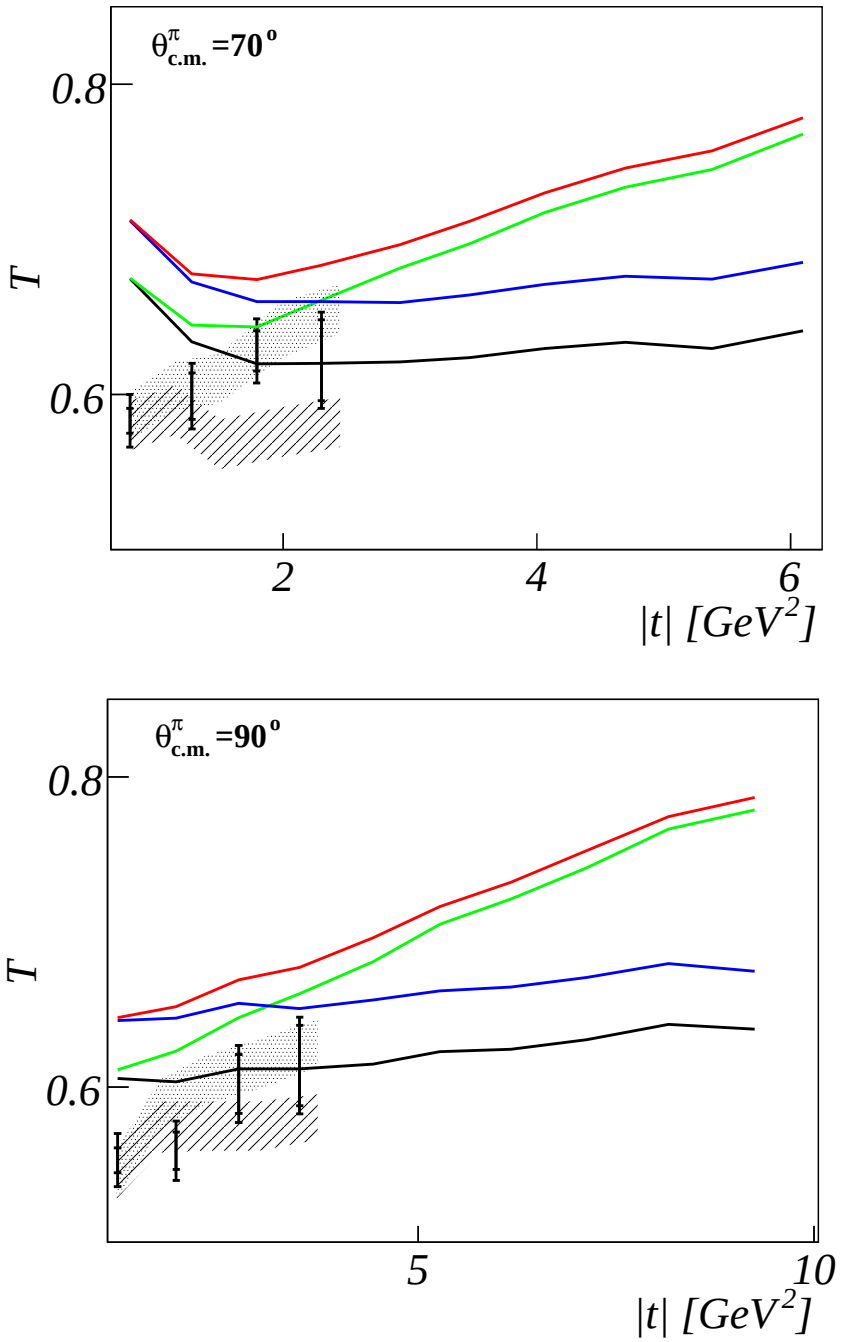

Figure 3.8 The nuclear transparency extracted from ^{4}He$(\gamma, p\pi^-)$ versus the squared momentum transfer $|t|$ at $\theta^{\pi}_{\text{c.m.}} = 70°$ (upper panel) and $\theta^{\pi}_{\text{c.m.}} = 90°$ (lower panel). The black and green curves are RMSGA and RMSGA+CT calculations respectively. The blue and red line are RMSGA+SRC and RMSGA+SRC+CT results. Table 3.1 lists the kinematics of the calculated points. The semiclassical model [127] results are presented by the shaded areas: the hatched (dotted) area is a calculation without (with) CT. Data from [47].

contribution. This phenomenon can be attributed to the behavior of the proton-proton and (to a lesser extent) proton-neutron cross section for proton momenta of about 1 GeV. As can be appreciated from Fig. 3.10, a drop from $\sim$ 40 mb to about 20-30 mb occurs as one approaches 1 GeV from higher momenta.

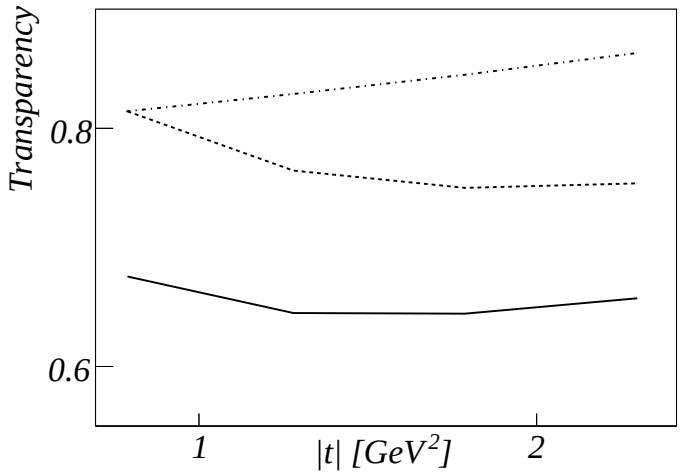

Figure 3.9 Contributions of the pion (dashed-dotted) and nucleon (dashed) to the total nuclear transparency (full) extracted from ^{4}He$(\gamma, p\pi^-)$ versus $|t|$ at $\theta^{\pi}_{\text{c.m.}} = 70°$. All calculations include CT.

Figure 3.9 also shows that the ^{4}He nucleus is more transparent for pion emission than for proton emission. This can be partially attributed to the lower pion total cross sections. As pointed out in Fig. 2.15 the larger formation length, and corresponding bigger reduction of the effective cross section make that the CT effect is larger for pions than for protons. In Fig. 3.11 the computed increase in the nuclear transparency caused by CT and SRC mechanisms is shown as a function of $|t|$. One observes that SRC mechanisms increase the nuclear transparency by about 5%. As there is no direct dependence on the hard-scale, the increase is almost independent of $|t|$. Inclusion of CT effects tends to increase the predicted transparency at a rate which depends on a hard-scale parameter. Here, that role is played by the momentum-transfer $|t|$. The CT phenomenon shows a linear rise from almost 0 to over 20% at the largest values of $|t|$. For $|t| \leq 2.5$ GeV^2 the predicted effect of SRC is larger than the increase induced by the CT mechanism. The SRC decrease the slope in the $|t|$ dependence of the CT phenomenon. Indeed, the SRC induces holes in the nuclear density in the direct neighborhood of the interaction point (see Fig. 2.16) where the CT effects are largest. At high $|t|$ the short-range correlations have a modest impact on the magnitude of the CT effects. Our investigations show that by studying the hard-scale dependence of the transparency the CT-related mechanisms can be clearly separated from the SRC ones.

In the search of phenomena like CT in transparency studies, it is of the utmost impor-

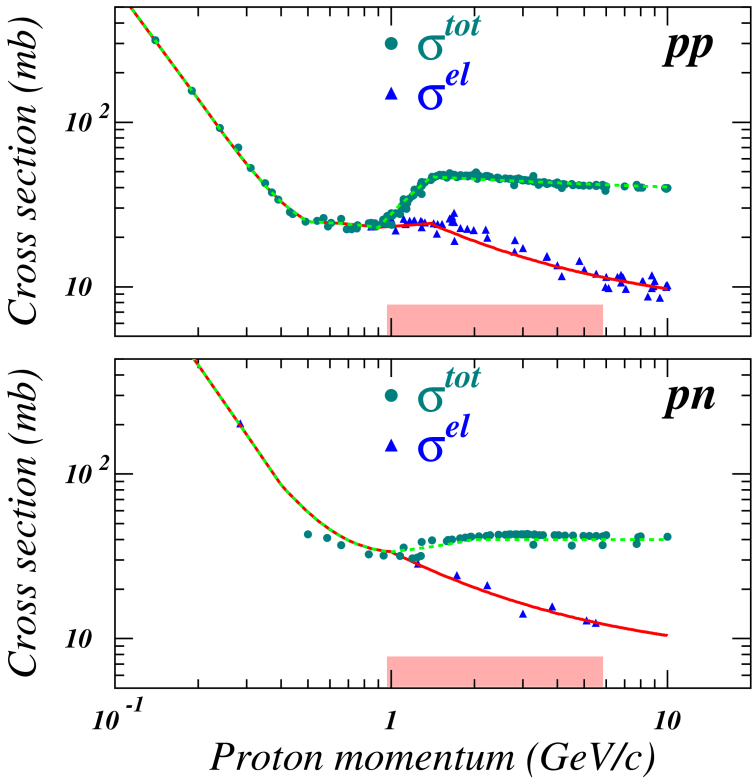

Figure 3.10 Total and elastic cross sections for proton-proton (upper) proton-neutron (lower panel) scattering as a function of proton lab momentum. Data are from Ref. [104]. Solid and dashed curves show global fits used in our calculations from Ref. [72]. The pink box indicates the momenta of the ejected nucleon covered in our calculations.

tance to have robust and advanced calculations based on concepts from traditional nuclear physics. Thereby, one of the major sources of uncertainty stem from the description of FSI mechanisms. In our eikonal model, we can either use optical potentials (ROMEA) or a Glauber framework (RMSGA). In kinematic regions of moderate hadron momenta both approaches can be used [73]. As they adopt very different underlying assumptions, we consider a comparison between the predictions of the two approaches as a profound test of the trustworthiness of either approach. We computed the transparency of the ^{4}He$(\gamma, p\pi^-)$ reaction for kinematics at $\theta^{\pi}_{\text{c.m.}} = 70^\circ$ and 90° with ejected proton momenta ranging from 500 MeV/c to 1 GeV/c, listed in Table 3.2. As can be appreciated from Fig. 3.12, both descriptions yield a similar shape, but the RMSGA calculations are consistently larger by about 5%. At higher nucleon momenta, however, the difference between the predictions for the transparencies in the two approaches shrinks to a few percent. The estimated model dependence in the computed transparencies is of the same order as the predicted role of

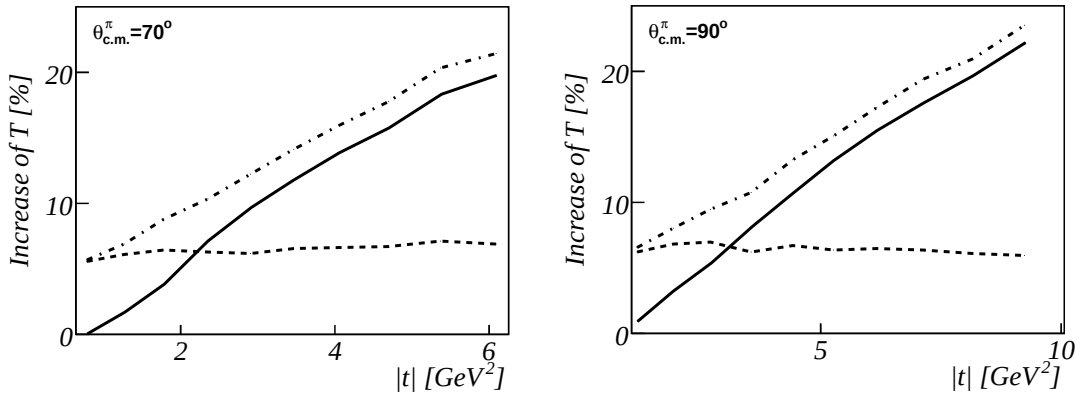

Figure 3.11 The $|t|$ dependence of the relative increase of the nuclear transparency due to SRC and CT effects. We consider the ^{4}He$(\gamma, p\pi^-)$ reaction at $\theta^{\pi}_{\text{c.m.}} = 70°$ (left panel) and 90° (right panel) and kinematic conditions from Table 3.1. The baseline result is the RMSGA calculation. The solid (dashed) curve includes the effect of CT (SRC). The dot-dashed line is the combined effect of CT+SRC.

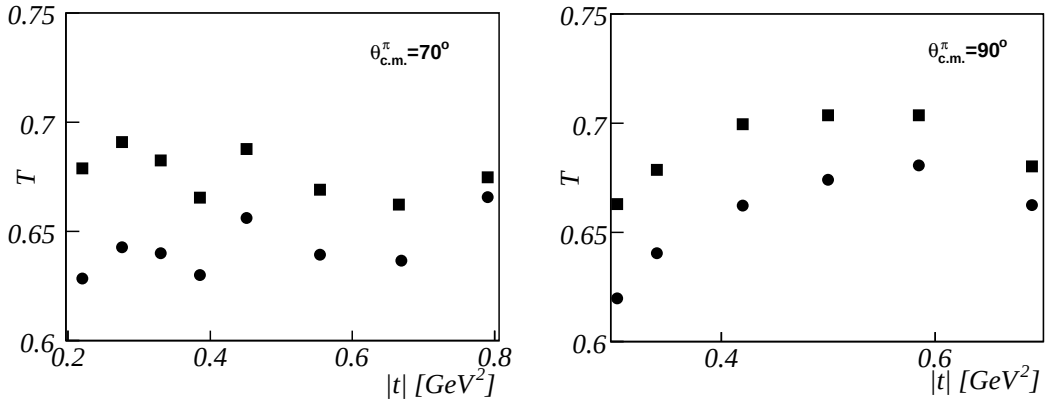

Figure 3.12 Comparison between the RMSGA (squares) and ROMEA (circles) description of the nucleon transparency of the ^{4}He$(\gamma, p\pi^-)$ reaction for kinematics at $\theta^{\pi}_{\text{c.m.}} = 70°$ (left panel) and 90° (right panel). Neither CT nor SRC effects were included in the calculations.

SRC mechanisms. From these observations, it is clear that pion and nuclear transparencies are not the optimum observables to study SRC mechanisms in nuclei. Indeed they bring about a relatively modest overall renormalization of about 5 %. Unlike the CT effects for example, their role does not grow with an increasing hard-scale, nor is there any sizable A-dependence in the SRC effects.

3.3.2 Pion Electroproduction

The E01-107 collaboration at Jefferson Lab measured the nuclear transparency for the pion electroproduction process on H, ^{12}C, ^{27}Al, ^{64}Cu and ^{197}Au. Measurements were done for the kinematics listed in Table 3.3. The virtual photon can fluctuate into a $q\bar{q}$-pair along a certain

q [MeV]	$\theta^{\pi}_{\text{c.m.}}$ [deg]	p_N [MeV]	θ_N [deg]	p_π [MeV]	θ_π [deg]
600	90°	573	41.61°	417	−65.74°
650	70°	489	51.20°	513	−47.91°
650	90°	611	41.50°	448	−64.64°
750	70°	546	51.01°	588	−46.23°
750	90°	686	41.20°	509	−62.59°
850	70°	601	50.72°	661	−44.70°
850	90°	757	40.83°	567	−60.72°
950	70°	653	50.37°	733	−43.31°
950	90°	825	40.43°	625	−58.99°
1069	70°	713	49.92°	818	−41.81°
1069	90°	905	39.90°	691	−57.11°
1250	70°	800	49.18°	946	−39.80°
1450	70°	892	48.36°	1086	−37.87°
1648	70°	989	47.39°	1238	−36.02°

Table 3.2 Central values for the photon energy (MeV), proton momentum p_N (MeV), proton angle θ_N, pion momentum p_π (MeV) and pion angle θ_π for $\theta^{\pi}_{\text{c.m.}} = 70°, 90°$, used in the low energy comparison between the RMSGA and ROMEA models. Angles are measured relative to the incoming photon momentum.

distance (its coherence length), and introduce initial-state interactions in this manner. It is important to minimize the influence of these competing energy-dependent reaction mechanisms on the transparency. In the kinematics of the experiment under consideration, the coherence length is of t he order $0.2 - 0.5$ fm, and smaller than the radius of a nucleus. In all the measurements the pion is detected in a relatively narrow cone about the momentum transfer. We have performed calculations for all target nuclei. The transparency is defined as

$$T = \frac{\sum_\alpha \int d\omega Y(\omega) \int_{\Delta^3 p_m} d\vec{p}_m \left(\frac{d^8\sigma}{d\Omega_{e'} dE_{e'} dE_\pi d\Omega_\pi d\Omega_N} \right)_{\text{RMSGA}}}{\sum_\alpha \int d\omega Y(\omega) \int_{\Delta^3 p_m} d\vec{p}_m \left(\frac{d^8\sigma}{d\Omega_{e'} dE_{e'} dE_\pi d\Omega_\pi d\Omega_N} \right)_{\text{RPWIA}}} . \tag{3.4}$$

The integration over ω takes into account the spread in energy of the virtual photon in the experiment and weighs each point with the reconstructed yield $Y(\omega)$ [128]. The quantity $\Delta^3 p_m$ specifies the phase space of the missing momentum and is determined by the condition $|p_m| \leq 300$ MeV/c, the experimental cuts and detector acceptances. An experimental cut of 100 MeV was placed on the missing mass of the final state. Accordingly, the undetected final neutron is an extremely slow one. The experimentally transparency is obtained by dividing the measured yield by a Monte-Carlo equivalent yield for the targets with nucleon number A and subsequently comparing it to the ratio of the yields for the ^{1}H target [50]:

Q^2 [GeV^2]	E_e [MeV]	θ_e [deg]	$E_{e'}$ [MeV]	p_π [MeV]	θ_π [deg]
1.10	4021	27.76°	1190	2793	10.58°
2.15	5012	28.85°	1730	3187	13.44°
3.00	5012	37.77°	1430	3418	12.74°
3.91	5767	40.38°	1423	4077	11.53°
4.69	5767	52.67°	1034	4412	9.09°

Table 3.3 Kinematics used in the experiment measuring the pion electroproduction transparency. Central values of Q^2 (GeV^2), incoming electron energy E_e(MeV), electron scattering angle θ_e (degrees), scattered electron energy $E_{e'}$ (MeV), ejected pion momentum p_π (MeV), and ejected pion angle (degrees) for the kinematics of the Jefferson Laboratory experiment E01-107. Angles are measured relative to the incoming electron beam.

$$T = \left(\bar{Y}_{\text{measured}}/\bar{Y}_{\text{MC}}\right)_A / \left(\bar{Y}_{\text{measured}}/\bar{Y}_{\text{MC}}\right)_{\text{H}} \tag{3.5}$$

As the Monte-Carlo simulation does not include the attenuation mechanisms on the detected pions, the measured transparency is a measure of these. We compute these intranuclear attenuation effects on the ejected pions in the RMSGA model. Thereby, we use a parametrization provided by the E01-107 collaboration for the free electroproduction in Eq. (2.46) [128, 129]. Details for this parametrization are provided in App. E.

Figure 3.13 presents the results from our transparency calculations for the electroproduction reaction together with the experimental data [50] and results from the semiclassical model of Ref. [130]. The RMSGA calculations display a modest increase over the Q^2 range. This behavior finds a simple explanation in the p_π dependence of the $\sigma^{\text{tot}}_{\pi^+ p}$ of Fig. 2.11. The results contained in Fig. 3.13 cover a range in pion momenta given by $2.8 \leq p_\pi \leq 4.4$ GeV. In this range, $\sigma^{\text{tot}}_{\pi^+ p}$ displays a soft decrease, which reflects itself in a soft increase of the nuclear transparency. The RMSGA+SRC transparencies are again about 5% larger than the RMSGA ones. The RMSGA+CT shows a strong Q^2 dependence with CT-related enhancements up to 20% at the highest energies. These calculations including CT are in very good agreement with the experimental data. The results overestimate the Au data somewhat, but the slope is in agreement with the data. If we compare the results to the semiclassical calculations, we see that the slopes of both calculations are in excellent agreement, reflecting the use of the same quantum diffusion parametrization for the CT effect. The absolute value differs, however, with the semiclassical results significantly larger for the ^{12}C calculations, but evolving to smaller for the ^{197}Au calculations. A third model developed by Kaskulov et al. [131] also finds excellent agreement between their calculations including CT and the data. It includes a model for the primary $p(e, e'\pi^+)n$

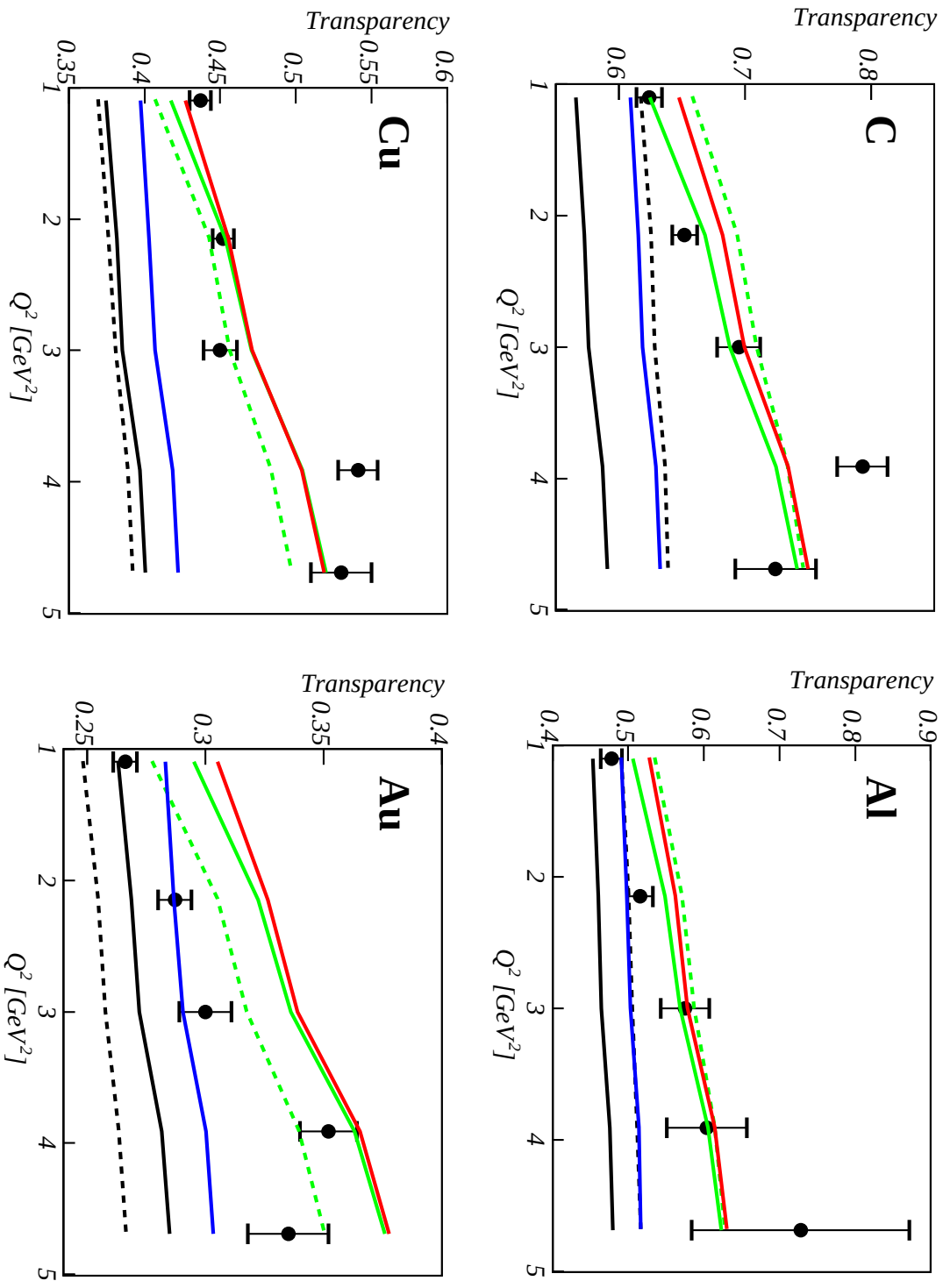

Figure 3.13 The Q^2 dependence of the nuclear transparency for the $A(e,e'\pi^+)$ process in ^{12}C, ^{27}Al, ^{63}Cu and ^{197}Au. The full black and green curves are RMSGA and RMSGA+CT calculations respectively. The blue and red line are RMSGA+SRC and RMSGA+SRC+CT results. The dashed curves are the results of the semiclassical model by Larson, Miller and Strikman [130] with (green) and without (black) CT. Data from Ref. [50].

reaction and offers different descriptions for the longitudinal and transverse parts of the cross section. The longitudinal part is described by a soft hadron exchange using Regge exchange trajectories, the transverse part combines the soft hadron exchange with a model describing the pion production as a hard partonic process. The FSI are modelled using the GiBUU model [132]. Color transparency is implemented with the quantum diffusion model outlined in sec. 2.3 with two different parametrizations. One with a formation time determined by the Lund model [133, 134], and one with the formation time as in sec. 2.3 with $\Delta M^2 = 1$ GeV^2 for the pion. The calculations for the second parametrization are shown in Fig. 3.14.

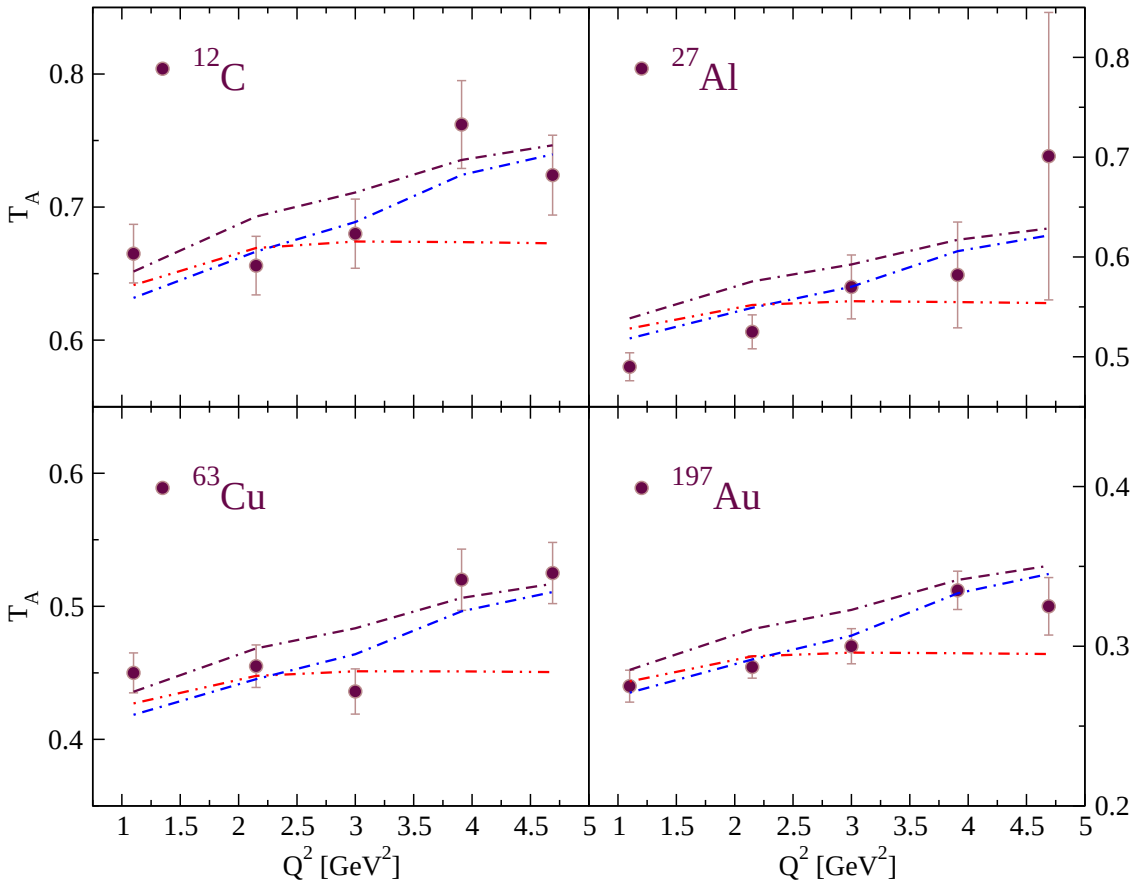

Figure 3.14 The Q^2 dependence of the nuclear transparency for the $A(e,e'\pi^+)$ process in ^{12}C, ^{27}Al, ^{63}Cu and ^{197}Au. The dash-dash dotted curves realize the CT effect in both the transverse and longitudinal part. The dash-dotted (dot-dot-dashed) curves only include the CT effect in the transverse (longitudinal) channel. Data from Ref. [50]. Figure taken from Ref. [131].

The evolution of the A dependence of the transparency is shown in Fig. 3.15. One observes that the addition of CT to the calculation adds more curvature and that this increases with higher Q^2. In Fig. 3.16 a fit of the A-dependence to the parametrization $T = A^{\alpha-1}$ is shown as a function of Q^2. Fits to the pion-nucleus scattering cross section have resulted in

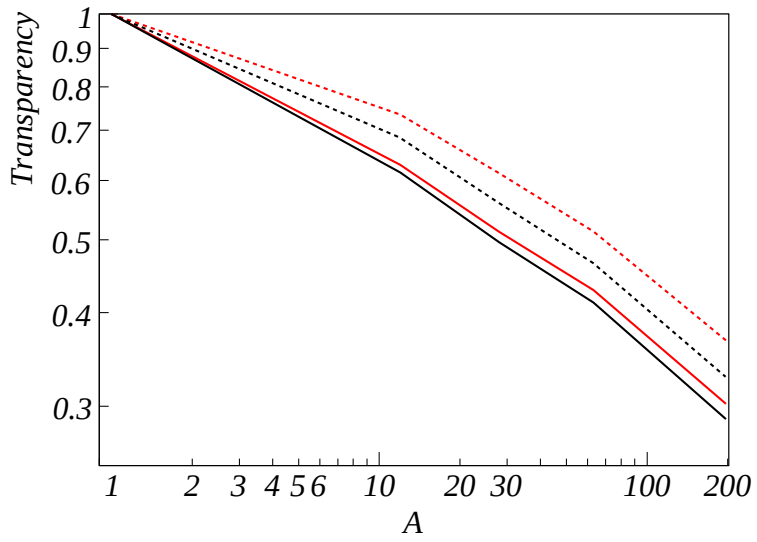

Figure 3.15 A dependence of the transparency for the $A(e,e'\pi^+)$ process at $Q^2 = 1.1\,\mathrm{GeV}^2$ (black) and $Q^2 = 4.69\,\mathrm{GeV}^2$ (red). The solid curves denote RMSGA+SRC results. The dashed lines are RMSGA+CT+SRC calculations.

$\alpha = 0.76 \pm 0.01$ [135]. Signatures of CT mechanisms can be extracted from an emerging Q^2 (or hard-scale) dependence of the extracted α's. As one can see, the fits to the data deviate significantly from the established value and are in nice agreement with both model calculations including CT, though the RMSGA+CT+SRC results consistently overestimate the data by a few percentages. Finally, in Fig. 3.17, we compare our model calculations for ^{1}2C with those from the semiclassical model of Ref. [130]. The transparency is plotted as function of the z component of $\vec{k} = \vec{p}_\pi - \vec{q}$. As previously observed for the photoproduction results (Fig. 3.12) and the electroproduction results (Fig. 3.13), our results again turn out to be higher by a few percentages.

3.3.3 Two Nucleon Knockout

The Hall A experiment E03-101 [48, 49] at Jefferson Lab has measured the transparency for the ^{3}He(γ,pp) and ^{12}C(γ,pp) reactions, and data analysis is currently under way [136]. Data are collected for proton c.m. angles $\theta_{c.m.} = 90°$ in coplanar and symmetric kinematics (Fig. 3.7). Table 3.5 lists the central values of the photon and nucleon momenta. Transparency is defined along the lines of Eqs. (3.3) and (3.4) as

$$T = \frac{\sum_{\alpha_1\alpha_2} \int dq Y(q) \int d\vec{P}_m \left(\frac{d^5\sigma}{dE_{k_1} d\Omega_{N_1} d\Omega_{N_2}} \right)_{\mathrm{RMSGA}}}{\sum_{\alpha_1\alpha_2} \int dq Y(q) \int d\vec{P}_m \left(\frac{d^5\sigma}{dE_{k_1} d\Omega_{N_1} d\Omega_{N_2}} \right)_{\mathrm{RPWIA}}} , \tag{3.6}$$

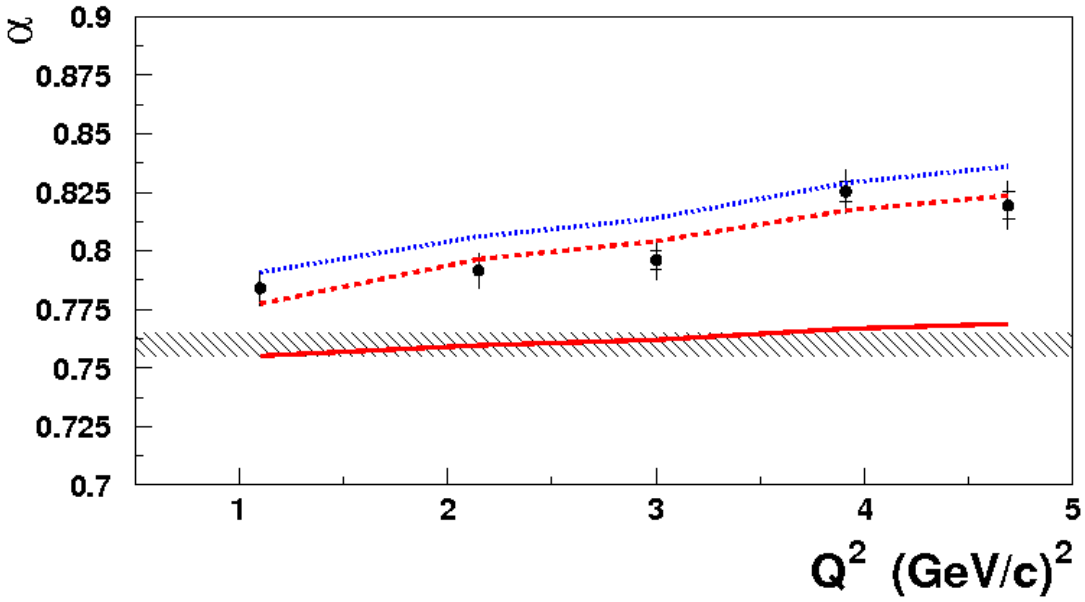

Figure 3.16 The α parameter in the parametrization of the A-dependence of the transparency $T = A^{\alpha-1}$ is shown as a function of Q^2. Inner error bars of the data show the statistic uncertainty, and the outer error bars are the quadrature sum of the statistical, systematic and model uncertainties [50]. The hatched band is the value of α extracted from pion-nucleus scattering data [135]. Red curves show fits to the calculations of Ref. [130] with (dashed) and without (solid) CT. The blue curve is a fit to the RMSGA+SRC+CT calculations. Figure taken from Ref. [50].

where $\sum_{\alpha_1\alpha_2}$ involves a sum over all possible shell combinations. The integrations $\int dq \int d\vec{P}_m$ are evaluated with a Monte-Carlo integration algorithm that takes into account experimental cuts and acceptances, and $Y(q)$ represents the weight of each generated event through the estimated reconstructed experimental photon beam spectrum [136]. The transparency is computed for knockout of a correlated pair in a relative S-state. Thereby we adopt a factorized approach, factorizing the matrix element of Eq. (2.47) into the momentum distribution of Eq. (3.1) and a part containing the primary (γ, pp) reaction. The latter part is again assumed to cancel out of the ration of Eq. (3.6).

Fig. 3.18 shows the results of the transparency calculations as a function of momentum transfer squared $|t| = (q^\mu - p^\mu_{N_1})$ for the (γ, pp) reaction in ^{3}He and ^{12}C as the knockout of a correlated pair. As for the pion photoproduction channel, the transparencies again rise for $|t| \leq 2$ (GeV/c^2). This phenomenon finds its origin in the local minimum of the total nucleon-nucleon cross section for momenta around 1 GeV/c. As with the previously studied reactions, the SRC mechanisms increase the transparency by 5%. The inclusion of CT on the other hand enhances the transparency up to over 20% for carbon at the highest energies. The most striking feature of these calculations, however, is the low values of the transparencies. If one takes the transparency value for the RSMGA calculations of

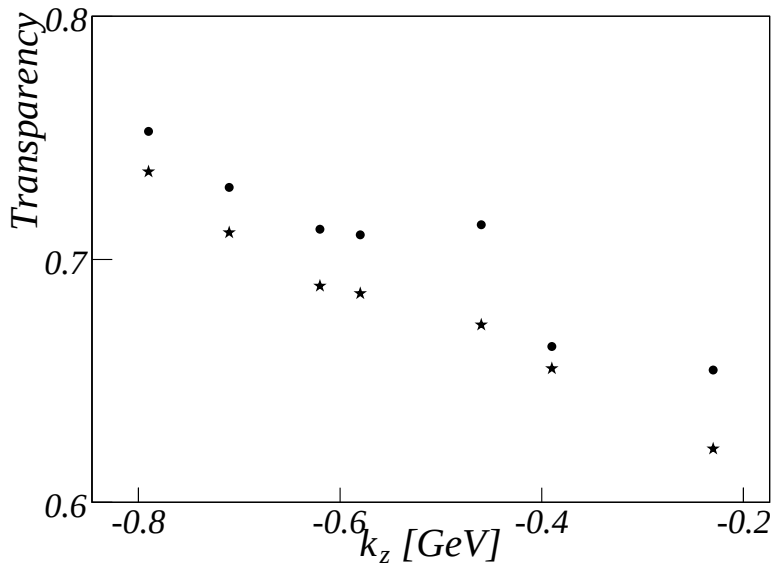

Figure 3.17 Nuclear transparency results for ^{12}C$(e,e'\pi^+)$ versus the z component of $\vec{k} = \vec{p}_\pi - \vec{q}$ for kinematics corresponding to data points of the JLab experiment of Ref. [50]. The circles are RMSGA+CT predictions, whereas the stars are from the semiclassical calculations of Ref. [130]. Kinematics are listed in Table 3.4

the ^{12}C$(e,e'p)$ reaction at these energies ($T \approx 0.6$ [73]) and naively squares this value to estimate the FSI, one obtains 0.36. This is significantly higher than the value of ~ 0.23 we obtain for the ^{12}C(γ,pp) transparency. As is shown in the next section, this is a consequence of the $A(\gamma,pp)$ reaction probing higher density regions of the nucleus then the $A(e,e'p)$ reaction. Higher densities mean more reduction, and hence a lower transparency.

Fig. 3.19 shows some results for the ^{3}He(γ,pp) process, with the reaction described as a hard rescattering process. To make these calculations numerical feasible, the FSI factor of Eq. (2.66) is approximated by factorizing it into a part containing the FSI of the ejected nucleons and a part containing the FSI of the propagator:

$$\begin{aligned}\mathscr{F}_{\rm FSI}(\vec{r}_1,\vec{r}_2) = &\int d\vec{r}_3 \ldots \int d\vec{r}_A |\phi_{\alpha_3}(\vec{r}_3)|^2 \ldots |\phi_{\alpha_A}(\vec{r}_A)|^2 \\ &\times \hat{\mathscr{S}}_{K_1N}(\vec{r}_2;\vec{r}_3,\ldots,\vec{r}_A)\hat{\mathscr{S}}_{K_2N}(\vec{r}_2;\vec{r}_3,\ldots,\vec{r}_A) \\ &\times \int d\vec{r}'_3 \ldots \int d\vec{r}'_A |\phi_{\alpha_3}(\vec{r}'_3)|^2 \ldots |\phi_{\alpha_A}(\vec{r}'_A)|^2 \hat{\mathscr{S}}_{\mathscr{N}N}(\vec{r}_2,\vec{r}_1;\vec{r}'_3,\ldots,\vec{r}'_A). \quad (3.7)\end{aligned}$$

With this approximation, we can take the factor containing the FSI of the ejected particles out of the innermost integrations, as they don't depend on the momentum vector of the propagator. The transparency is again calculated by using Eq. (3.6), but this time with the matrix element of Eq. (2.71) in the five-fold differential cross section. Calculations were done with all the FSI in Eq. (3.7) included and with the FSI of the propagator excluded.

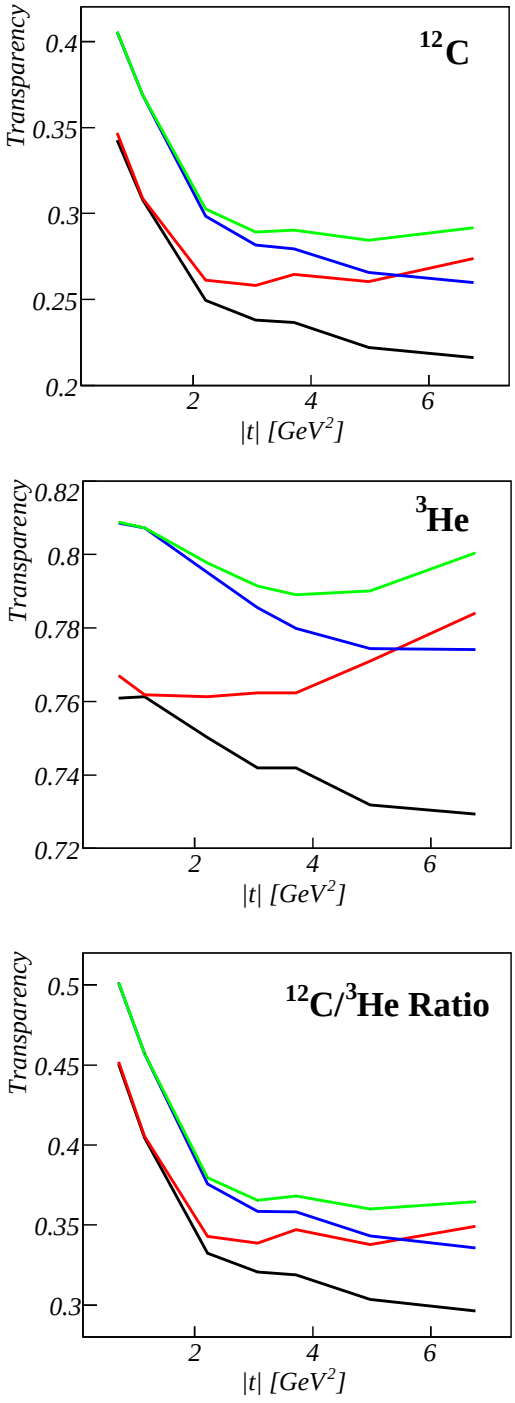

Figure 3.18 The nuclear transparency extracted from $^{12}C(\gamma, pp)$ (upper), $^{3}He(\gamma, pp)$ (middle) and their ratio (lower panel) versus the squared momentum transfer $|t|$. The black and red curves are RMSGA and RMSGA+CT calculations respectively. The blue and green line are RMSGA+SRC and RMSGA+SRC+CT results. Table 3.5 lists the kinematics of the calculated points. These calculations consider $^{3}He(\gamma, pp)$ as the breakup of a correlated pair.

Q^2 [GeV^2]	E_e [MeV]	θ_e [deg]	$E_{e'}$ [MeV]	p_π [MeV]	θ_π [deg]	k_z [GeV]
1.00	3540	29.00°	1126	2380	12.06°	-0.23
1.83	3540	53.46°	639	2823	9.23°	-0.39
2.15	5012	28.85°	1730	3187	13.44°	-0.46
3.00	4700	42.40°	1220	3315	12.20°	-0.58
3.00	5012	37.77°	1430	3418	12.74°	-0.62
4.00	5860	36.56°	1734	3897	13.02°	-0.71
5.00	5860	53.90°	1038	4540	9.08°	-0.79

Table 3.4 Kinematics used in the comparison between the RMSGA and semiclassical models for the $A(e,e'\pi^+)$ reaction. Central values of Q^2 (GeV^2), incoming electron energy E_e(MeV), electron scattering angle θ_e (degrees), scattered electron energy $E_{e'}$ (MeV), ejected pion momentum p_π (MeV), ejected pion angle (degrees), and z component of $\vec{k} = \vec{p}_\pi - \vec{q}$. Angles are measured relative to the incoming electron beam.

q [GeV]	p_{N_1} [MeV]	θ_{N_1} [deg]	p_{N_2} [MeV]	θ_{N_2} [deg]
0.849	943	65.32°	943	−65.32°
1.08	1095	62.62°	1095	−62.62°
1.65	1453	57.00°	1453	−57.00°
2.1	1711	53.69°	1711	−53.69°
2.45	1913	51.43°	1913	−51.43°
3.12	2276	47.98°	2276	−47.98°
4.07	2780	44.11°	2780	−44.11°

Table 3.5 Kinematics of the E03-101 experiment at Jefferson Lab. The experiment aims at measuring the transparency for double proton knockout reactions. Central values for the photon energy q (GeV), proton momenta p_{N_i} (MeV) and angles θ_{N_i} for $\theta_{\text{c.m.}} = 90°$. Angles are measured relative to the incoming photon momentum.

As can be seen in Fig. (3.19), the FSI of the propagator lower the transparency by about 5%. Both rescattering calculations result in transparencies with a similar $|t|$ dependence as the one-step process in Fig. 3.18. The calculations including the FSI of the propagator yield the lowest transparencies, indicating that the two-step two-nucleon knockout probes even higher densities than the correlated pair knockout. A detailed investigation of the $A(\gamma,NN)$ transparencies requires calculations with the two competing mechanisms summed at amplitude level. In this way, the size of the interference between the one- and two-step processes can also be determined.

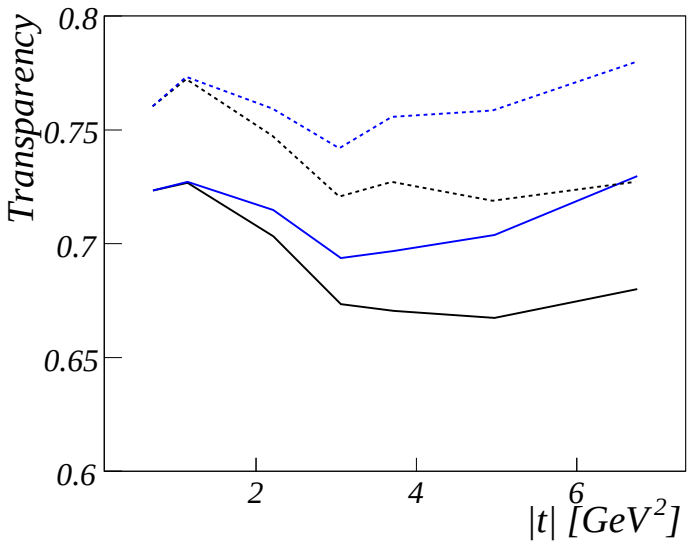

Figure 3.19 The nuclear transparency extracted from ^{3}He(γ, pp) (middle) versus the squared momentum transfer $|t|$. The black and blue curves are RMSGA and RMSGA+CT calculations respectively. Solid curves include all FSI, dashed curves do not include the FSI of the propagator. These calculations consider ^{3}He(γ, pp) as a hard-rescattering mechanism.

3.4 Density Dependence

Nucleon removal studies in quasi-free kinematics belong to the most powerful instruments for studying the structure of nuclei. Since the 1960's electroinduced single-nucleon knockout(or, $A(e,e'p)$) has provided a wealth of information about the merits and the limitations of the nuclear shell-model [137]. Quasi-free proton scattering from nuclei (i.e. $A(p,2p)$) has a somewhat longer history [138] and could in principle provide similar information than $A(e,e'p)$. With three protons subject to attenuation effects, in $A(p,2p)$ the description of the initial and final-state interactions, is a more challenging issue than in $A(e,e'p)$. More recent applications of the $A(p,2p)$ reaction involve the analyzing power (A_y) as an instrument for probing possible medium modifications of hadron properties and the density dependence of the nucleon-nucleon interaction [81, 139]. In inverse kinematics (i.e. the $p(A,2p)A-1$ reaction) the $(p,2p)$ process offers great opportunities for systematic studies of the density and isospin dependency of single-particle properties in unstable nuclei [140] at high-energy radioactive beam facilities [141]. Studies of that type have the potential to study the equation of state for nuclei far from equilibrium. With regard to quasi-free $A(e,e'p)$, a recent development includes the study of possible medium modifications of electromagnetic form factors through double polarization experiments of the type ^{4}He$(\vec{e},e'\vec{p})$ [142]. Another active line of current research with electrons is the two-nucleon removal reaction ($A(\gamma,pp)$ and $A(e,e'pp)$) in selected kinematics. This process is expected to pro-

vide a window on the short-range structure of nuclei when performed at sufficiently high values of the four-momentum transfer [64].

The development of an appropriate reaction theory is essential for reliably reliably extracting the physical information from the nucleon removal reactions. For nucleon kinetic energies up to about 1 GeV the distorted wave impulse approximation (DWIA) with appropriately constrained optical potentials, has enjoyed many successes in that it could reproduce fairly well a large amount of measurements [137]. Constraining the optical potentials heavily depends on the availability of elastic proton-nucleus scattering data. Moreover, the optical potentials exhibit a substantial kinetic-energy dependence. This energy dependence makes it difficult to make more general statements about e.g. the role of attenuation effects and the effective densities probed in the various reactions. At sufficiently high nucleon energies the Glauber approach provides a valid alternative for the DWIA framework. The Glauber approach has the advantage that the effect of initial and final-state interactions (ISIs and FSIs) can be computed from the knowledge of the elementary proton-proton and proton-neutron differential cross sections and a nuclear-structure model for the density of the target (residual) nucleus. Moreover, for nucleon momenta exceeding about 1 GeV the energy dependence of the parameters entering the Glauber calculations is relatively smooth. This results, for example, in nuclear $A(e,e'p)$ transparencies which exhibit little energy dependence at larger nucleon kinetic energies [73]. From the theoretical point of view, it allows one to make more universal statements about the predicted role of nuclear attenuations. Another advantage of the Glauber approach is that it is applicable to a wide range of reactions, including electromagnetic and hadronic probes, with stable and unstable nuclei [143, 144].

In this section we exploit the robustness of the Glauber approach to study the density dependence of quasi-free nucleon removal reactions for ejected protons with a kinetic energy of 1.5 GeV . Indeed, investigations into the medium dependence of nucleon properties and the study of the nuclear structure of unstable nuclei e.g., heavily rely on the possibility of effectively probing regions of sufficient density in the target nucleus. Nuclear attenuation effects on the impinging and ejected protons can make nucleon removal reactions to effectively probe regions of relatively small density near the surface of the target nucleus. With respect to the description of nuclear attenuation effects, which exhibit a certain degree of model dependence, we stress the importance of making cross checks over different fields (electromagnetic versus hadronic probes) and of studying varying numbers of hadrons that are subject to nuclear attenuation. Here, we compare the effective nuclear density that can be probed in reactions that have one nucleon ($A(e,e'p)$), two nucleons ($A(e,e'pp)$) and three nucleons ($A(p,2p)$) subject to nuclear attenuation effects.

In a factorized approach, the differential cross sections for the single-nucleon removal reactions considered here (i.e. $A(p,2p)$ and $A(e,e'p)$) are proportional to the distorted momentum distributions $\rho^D(\vec{p}_m)$ of Eq. (2.29)

$$\begin{aligned}\rho^D_{n\kappa}(\vec{p}_m) &= \frac{1}{(2\pi)^3}\sum_{s,m}\left|\int d\vec{r}\, e^{-i\vec{p}_m\cdot\vec{r}}\bar{u}(\vec{p}_m,s)\mathscr{F}_{\rm RMSGA}(\vec{r})\phi_{n\kappa m}(\vec{r})\right|^2 \\ &= \frac{1}{2(2\pi)^3}\int dr\int d\theta\left[\sum_{s,m}D(r,\theta)^\dagger\bar{u}(\vec{p}_m,s)\phi^D_{n\kappa m}\right. \\ &\left. + D(r,\theta)\left(\bar{u}(\vec{p}_m,s)\phi^D_{n\kappa m}\right)^\dagger\right] \equiv \int dr d\theta\,\delta(r,\theta) \\ &\equiv \int dr\,\delta(r)\,, \end{aligned} \tag{3.8}$$

where the quantum numbers (n,κ) determine the shell of the struck nucleon. The missing momentum $\vec{p}_m$ is determined by the difference between the asymptotic three-momentum $\vec{p}$ of the ejected nucleon and the three-momentum transfer $\vec{q}$. We define the z-axis along the $\vec{q}$ and the xz-plane as the reaction plane. The function $\delta(r)$ ($\delta(r,\theta)$) defined in Eq. (3.8) encodes the contribution from an infinitesimal interval around r (r and θ) to a single-nucleon removal cross section [139]. The function $D(r,\theta)$ which was introduced in (3.8) reads

$$D(r,\theta) = \int d\phi\,\sin\theta\, e^{-i\vec{p}_m\cdot\vec{r}}\bar{u}(\vec{p}_m,s)\mathscr{F}_{\rm RMSGA}(\vec{r})\phi_{n\kappa m}(\vec{r})\,. \tag{3.9}$$

The Glauber phase operator $\mathscr{F}_{\rm RMSGA}(\vec{r})$ encodes the combined effect of the initial and final-state interactions [72, 74]. Along the lines of Eq. (3.8), we can formulate a similar function $\delta(R,\theta)$ for the $A(\gamma,pp)$ and $A(e,e'pp)$ reactions describing the knockout of a correlated pair in a relative S-state, by departing from the distorted momentum distributions of Eq. (3.1):

$$\rho^D_{n_1\kappa_1 n_2\kappa_2}(\vec{P}_m) \equiv \int dR d\theta\,\delta(R,\theta) \equiv \int dR\delta(R)\,. \tag{3.10}$$

with $\vec{P}_m = \vec{k}_1 - \vec{k}_2 + \vec{q}$ (where $\vec{q}$ is the momentum of the incoming photon and $\vec{k}_i$ the asymptotic momenta of the ejected nucleons).

In Fig. 3.20 we display the function $\delta(r,\theta)$ defined in the Eq. (3.8) for proton knockout from the $1s1/2$ and $1p3/2$ shell from a ^{12}C target. We compare the $(p,2p)$ with the $(e,e'p)$ result for an energy transfer of 1.5 GeV and conditions probing the maximum of the undisturbed momentum distribution $\rho_{n\kappa}(\vec{p})$. The latter can be obtained by setting $\mathscr{F}_{\rm RMSGA} = 1$. In the considered kinematics, it is clear that in the absence of nuclear attenuation effects (RPWIA), the upper ($0^\circ \le \theta \le 90^\circ$) and lower hemisphere ($90^\circ \le \theta \le 180^\circ$) of the target

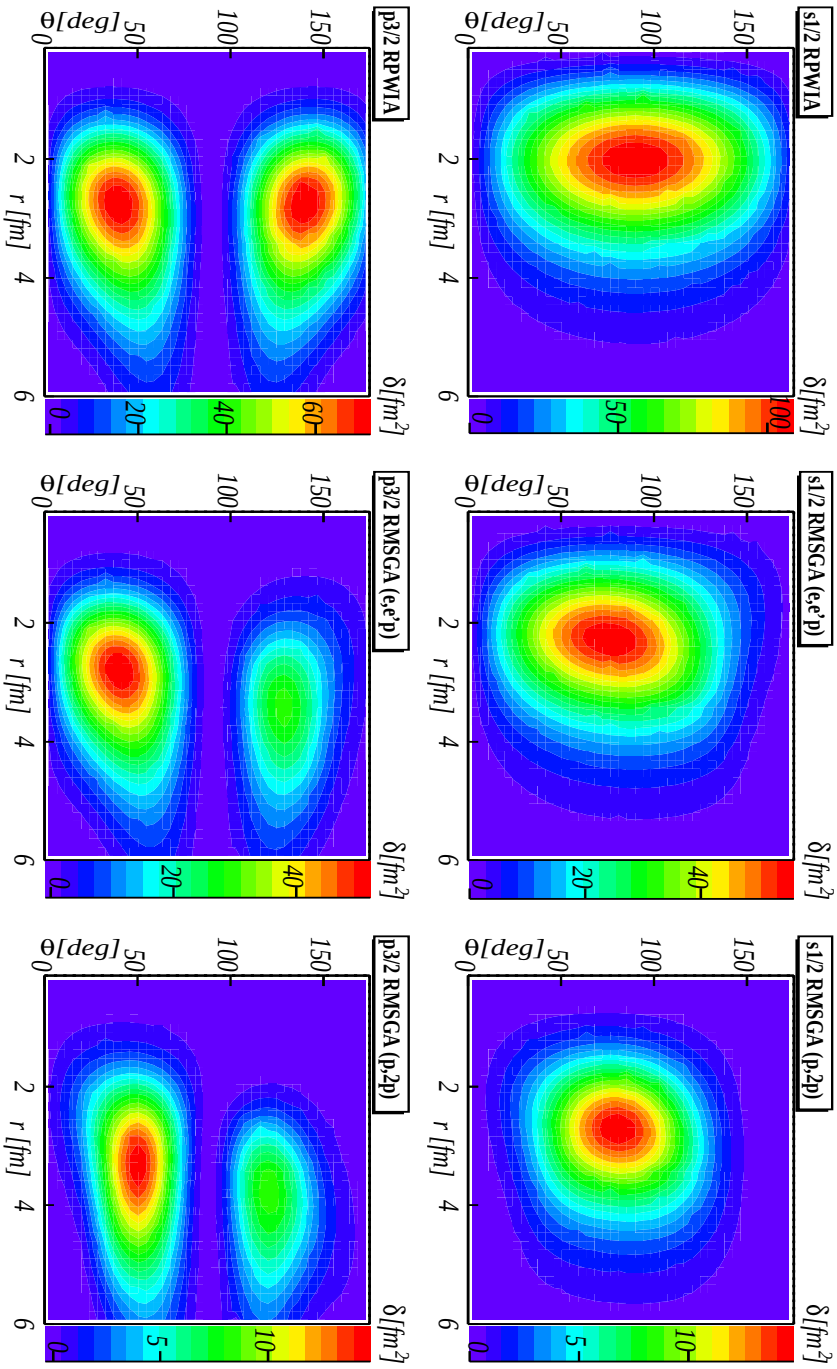

Figure 3.20 The function $\delta(r,\theta)$ for the ^{12}C$(e,e'p)$ and ^{12}C$(p,2p)$ reaction. For both types of reaction we consider an energy transfer of 1.5 GeV and a three-momentum transfer $\vec{q}$ which probes the maximum of the momentum distribution (i.e. p_m=0 MeV for knockout from the $1s1/2$-shell and p_m=115 MeV for removal from the $1p3/2$-shell). For the $(e,e'p)$ results, the proton is detected along the direction of the momentum transfer. For the $(p,2p)$, the incoming proton has a kinetic energy of about 3 GeV and the two ejected protons have a kinetic energy of 1.5 GeV. They are detected under an angle of about 32° but on opposite sides of the incoming beam. For the sake of reference, the proton rms radius in ^{12}C as determined from elastic electron scattering is $\left\langle r^2 \right\rangle^{1/2} = 2.464 \pm 0.012$fm [145].

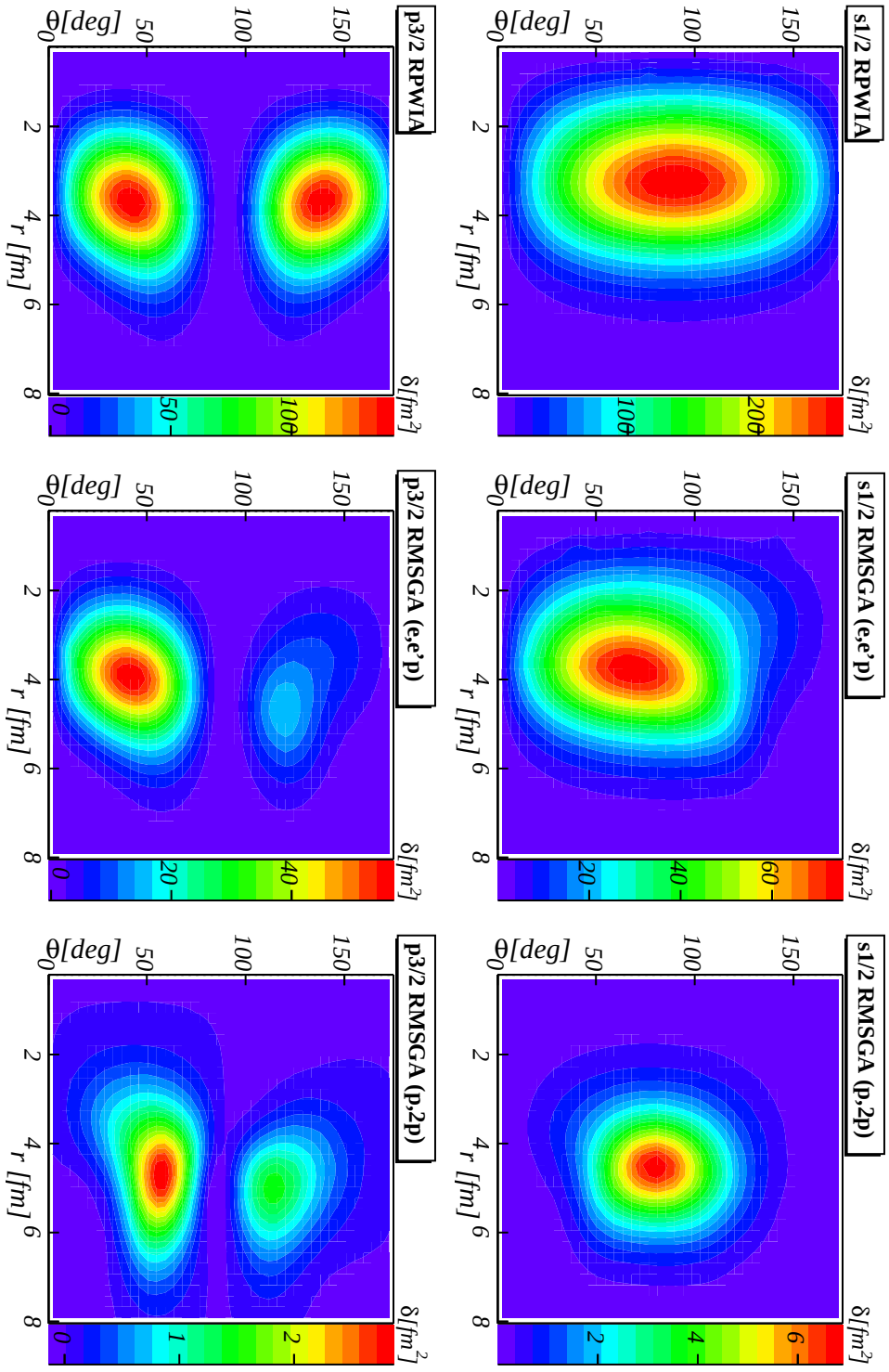

Figure 3.21 The function $\delta(r,\theta)$ for the ^{56}Fe$(e,e'p)$ and ^{56}Fe$(p,2p)$ reaction. For both types of reaction we consider an energy transfer of 1.5 GeV and a three-momentum transfer $\vec{q}$ which probes the maximum of the momentum distribution (i.e. p_m=0 MeV for knockout from the $1s1/2$-shell and p_m=100 MeV for removal from the $1p3/2$-shell). For the $(e,e'p)$ results, the proton is detected along the direction of the momentum transfer. For the $(p,2p)$, the incoming proton has a kinetic energy of about 3 GeV and the two ejected protons have a kinetic energy of 1.5 GeV. They are detected under an angle of about 32° but on opposite sides of the incoming beam.

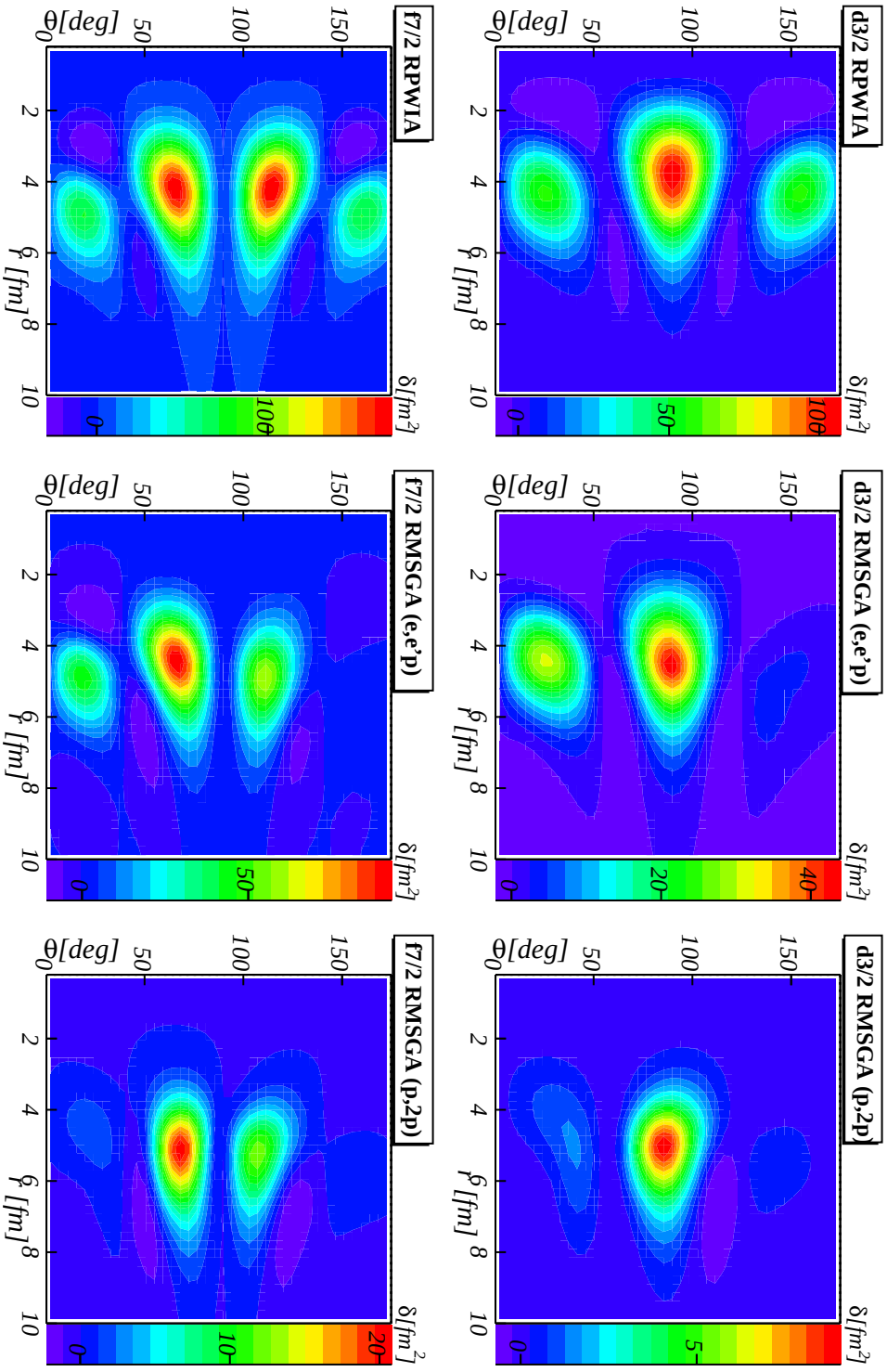

Figure 3.22 The function $\delta(r,\theta)$ for the ^{56}Fe$(e,e'p)$ and ^{56}Fe$(p,2p)$ reaction. For both types of reaction we consider an energy transfer of 1.5 GeV and a three-momentum transfer $\vec{q}$ which probes the maximum of the momentum distribution (i.e. p_m=140 MeV for knockout from the $1d3/2$-shell and p_m=180 MeV for removal from the $1f7/2$-shell). For the $(e,e'p)$ results, the proton is detected along the direction of the momentum transfer. For the $(p,2p)$, the incoming proton has a kinetic energy of about 3 GeV and the two ejected protons have a kinetic energy of 1.5 GeV. They are detected under an angle of about 32° but on opposite sides of the incoming beam.

nucleus would equally contribute to $\delta(r,\theta)$ and the measured signal. Moreover, the $\delta(r,\theta)$ becomes equal for $(e,e'p)$ and $(p,2p)$. The ISI and FSI have the strongest impact at the highest nuclear densities, which makes the $\delta(r,\theta)$ to shift to larger values of the radial coordinate r. In addition, the contribution from the upper and lower hemisphere becomes asymmetric when considering attenuation mechanisms. Indeed, the nuclear hemisphere which is closest to the proton detector will provide the strongest contribution to the detected signal. The stronger the effect of attenuations, the larger the shifts in r, the larger the induced asymmetries between the upper and lower hemisphere and the stronger the reduction. Obviously, the asymmetry, shift and reduction occur for the $\delta(r,\theta)$ in $(e,e'p)$ and $(p,2p)$. All three effects, however, are far more pronounced for the $(p,2p)$ than for the corresponding $(e,e'p)$ $\delta(r,\theta)$. The same observations apply for Figs. 3.21 and 3.22, where we plotted the $\delta(r,\theta)$ function f or a ^{56}Fe target for the same kinematical conditions as in Fig. 3.20. Fig 3.21 shows results for the inner $11s1/2$ and $11p3/2$ shells, and Fig. 3.22 for the outer $11d3/2$ and $11f7/2$ shells. A comparison between the two figures also shows the greater reduction by the FSI of the signal strength for the inner shells in Fig. 3.20.

In Fig. 3.23 we display for the ^{12}C target the function $\delta(R,\theta)$ defined in the Eq. (3.10) for two-proton knockout from the $(1s1/2-1s1/2)$-, $(1s1/2-1p3/2)$-, and $(1p3/2-1p3/2)$-orbits. Comparing Figs. 3.20 and 3.23 it is clear that two-proton removal at high energies, really succeeds in probing the high-density regions of the target nucleus (note the different range in the radial coordinate r for Figs. 3.20 and 3.23. The attenuation mechanisms induce shifts to the surface but the bulk of the measured strength can be clearly attributed to high-density regions in the target nucleus. Results for the ^{56}Fe target are shown in Fig. 3.21 for several two proton removals from the same shell . Here too, higher densities are probed when compared to the $(e,e'p)$ and $(p,2p)$ results.

In order to quantify the average densities that the various reactions can probe, we introduce [81, 139]

$$\overline{\rho} = \frac{\int dr d\theta \rho_p(\vec{r})\,\delta(r,\theta)}{\int dr d\theta \delta(r,\theta)}\,, \tag{3.11}$$

where $\rho(\vec{r})$ is the density of the target nucleus and $\delta(r,\theta)$ [or $\delta(R,\theta)$] the function as it was defined in Eq. (3.8) [(3.10)]. Table 3.6 lists a systematic comparison of the computed values of $\overline{\rho}$ for ^{12}C and ^{56}Fe. For both nuclei, the average density probed in the two-proton removal reaction from the $(1s1/2-1s1/2)$ orbits approaches the nuclear saturation density of $\rho_0 = 0,17\text{fm}^{-3}$. We wish to stress the strong dependence on the nuclear orbit. Despite the strong attenuation, the $(p,2p)$ reaction from the $1s1/2$ orbit in ^{12}C can effectively probe higher densities than the $(e,e'p)$ reaction from the valence $1p3/2$ shell. One can also see

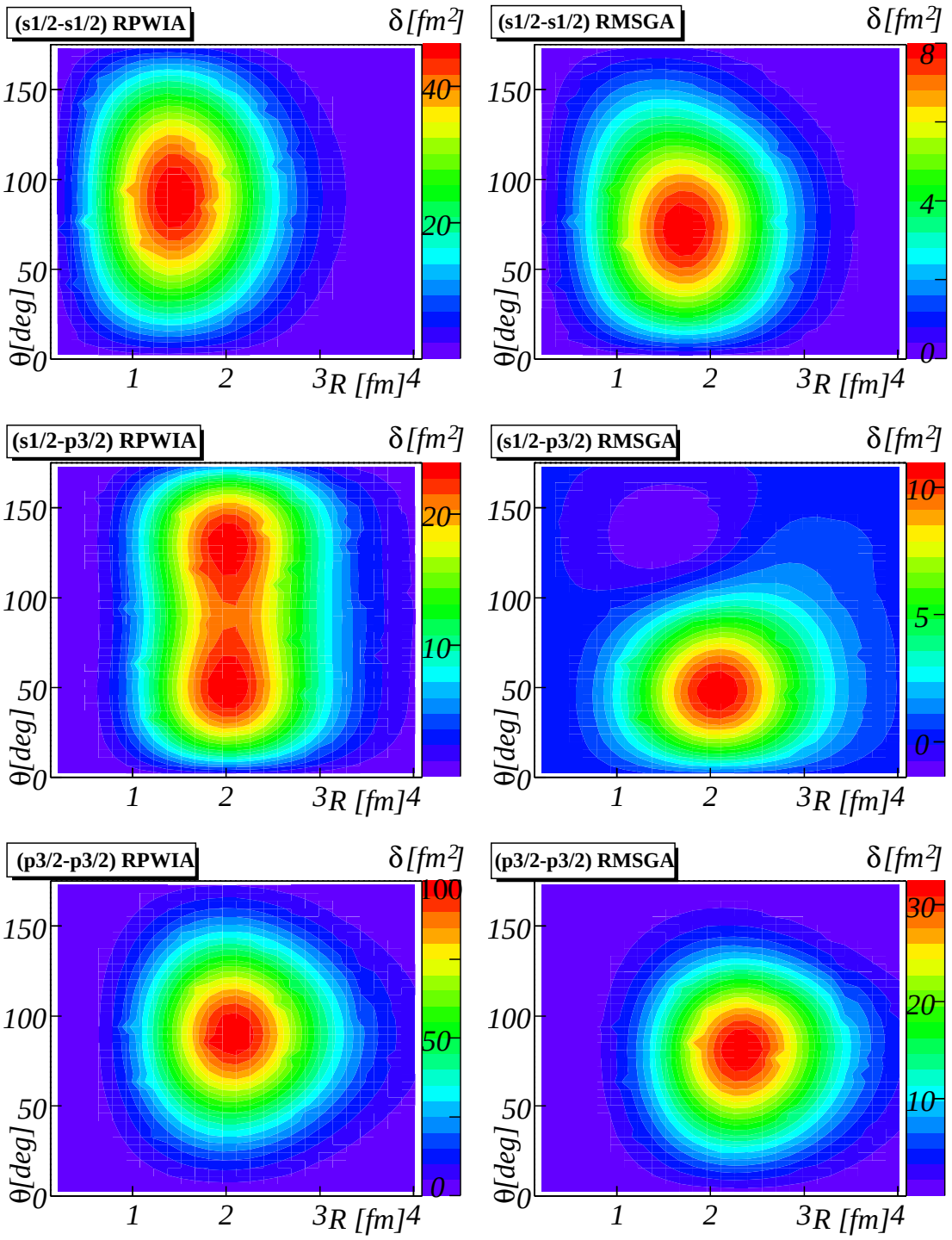

Figure 3.23 The function $\delta(r,\theta)$ for the exclusive ^{12}C(γ,pp) cross section. In all situations we consider an energy transfer of 3 GeV and a three-momentum transfer $\vec{q}$ which probes the maximum of the momentum distribution $\rho_{\alpha_1\alpha_2}(\vec{P})$ (i.e. P=0 MeV for knockout from the $(1s1/2-1s1/2)$- and $(1p3/2-1p3/2)$-orbits, and P=160 MeV for removal from the $(1s1/2-1p3/2)$-orbits). We consider coplanar and symmetric kinematics.

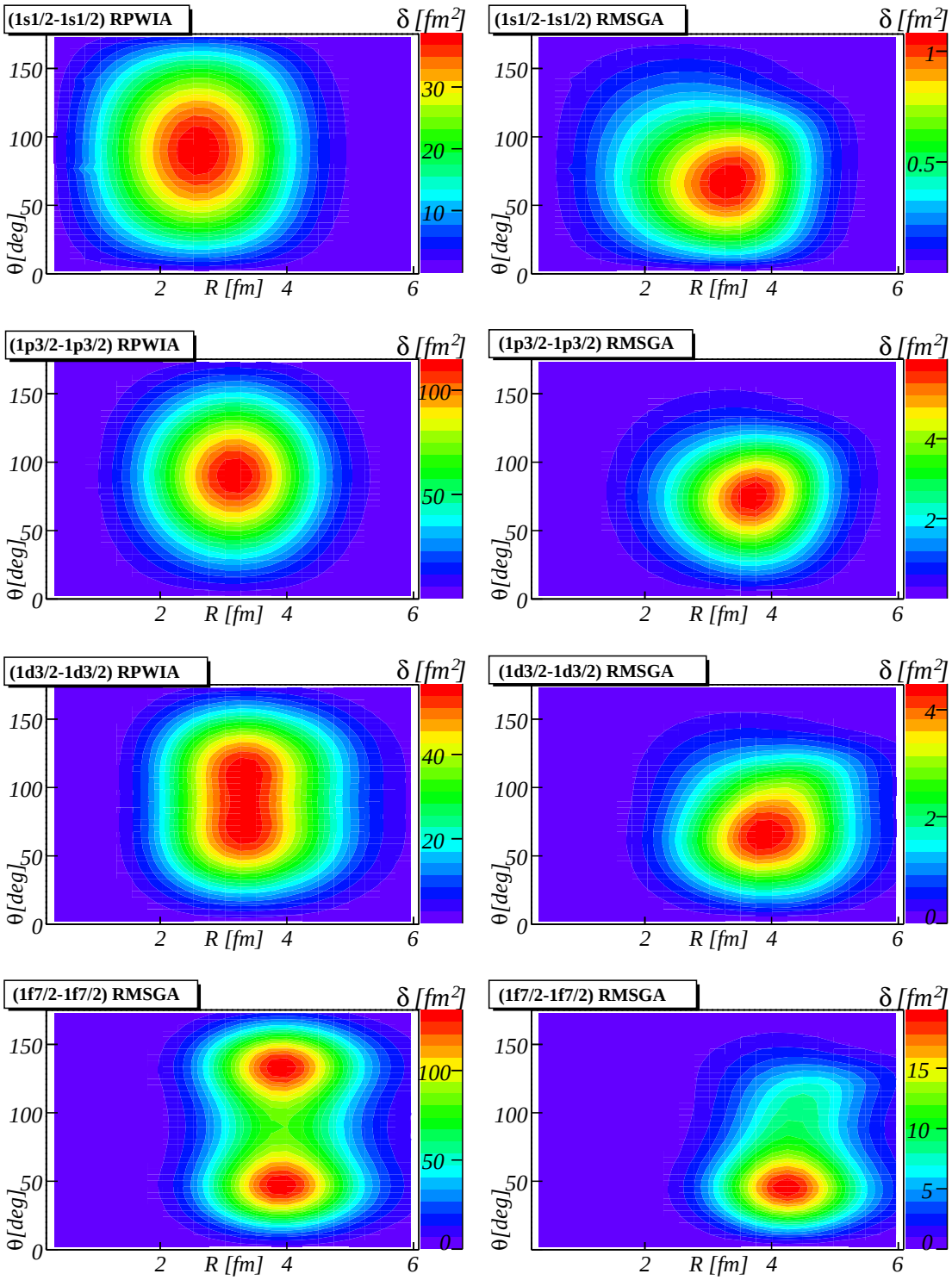

Figure 3.24 The function $\delta(r,\theta)$ for the exclusive ^{56}Fe(γ,pp) cross section. In all situations we consider an energy transfer of 3 GeV and a three-momentum transfer $\vec{q}$ which probes the maximum of the momentum distribution $\rho_{\alpha_1\alpha_2}(\vec{P})$ (i.e. P=0 MeV for knockout from all orbits). We consider coplanar and symmetric kinematics.

Nucleus	Reaction	Orbits	$\overline{\rho}(RPWIA)$ [fm^{-3}]	$\overline{\rho}(RMSGA)$ [fm^{-3}]
^{12}C	$(e,e'p)$	$1s1/2$	0.09975	0.08563
^{12}C	$(p,2p)$	$1s1/2$	0.09975	0.05548
^{12}C	$(e,e'p)$	$1p3/2$	0.04966	0.03821
^{12}C	$(p,2p)$	$1p3/2$	0.04966	0.02547
^{12}C	(γ,pp)	$(1s1/2-1s1/2)$	0.15005	0.13493
^{12}C	(γ,pp)	$(1p3/2-1p3/2)$	0.09547	0.07533
^{12}C	(γ,pp)	$(1s1/2-1p3/2)$	0.11546	0.09847
^{56}Fe	$(e,e'p)$	$1s1/2$	0.12631	0.11335
^{56}Fe	$(p,2p)$	$1s1/2$	0.12631	0.07784
^{56}Fe	$(e,e'p)$	$1p3/2$	0.11547	0.10228
^{56}Fe	$(p,2p)$	$1p3/2$	0.11547	0.06991
^{56}Fe	$(e,e'p)$	$1d3/2$	0.09444	0.08056
^{56}Fe	$(p,2p)$	$1d3/2$	0.09444	0.05295
^{56}Fe	$(e,e'p)$	$1f7/2$	0.07793	0.06587
^{56}Fe	$(p,2p)$	$1f7/2$	0.07793	0.04500
^{56}Fe	(γ,pp)	$(1s1/2-1s1/2)$	0.14513	0.13828
^{56}Fe	(γ,pp)	$(1p3/2-1p3/2)$	0.14005	0.12610
^{56}Fe	(γ,pp)	$(1d3/2-1d3/2)$	0.12982	0.10730
^{56}Fe	(γ,pp)	$(1f7/2-1f7/2)$	0.10995	0.08679

Table 3.6 The average density $\overline{\rho}$ probed in various reactions.

that the difference in densities probed between the different reactions is less pronounced for ^{56}Fe than for ^{12}C. Densities for both the $1s1/2$ and $1f7/2$ orbit in $A(p,2p)$ are about half of those in $A(\gamma,pp)$ in iron, whereas in carbon they are more about one third for both the $1s1/2$ and the $1p3/2$. For the $(p,2p)$ reaction with knockout from the $1s1/2$ orbit, the predicted effective mean density from the RMSGA calculations is $\overline{\rho} \approx 0.33\rho_0$. This number is almost identical to the DWIA results of Ref. [81] for ^{12}C$(p,2p)$ for 1 GeV incoming protons. Figs. 3.25 and 3.26 show $\delta(r)$ and $\delta(R)$ for knockout from the Fermi level of ^{12}C and ^{56}Fe compared to r squared times the nuclear density. Here, one can again clearly see only the (γ,pp) reaction succeeds in probing the high density region while the dominating contributions for the $(e,e'p)$ and $(p,2p)$ reactions stem from regions more than 1 fm removed from this maximum.

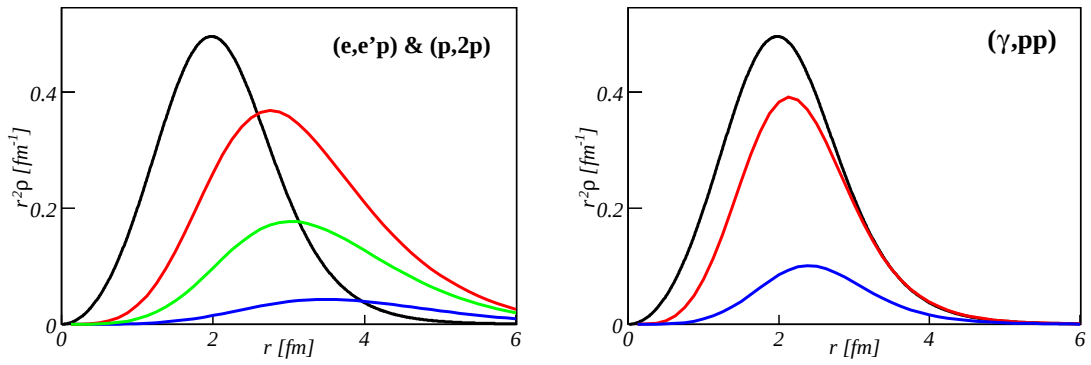

Figure 3.25 Contribution to the exclusive $^{12}\mathrm{C}(e,e'p)$ (green) , $^{12}\mathrm{C}(p,2p)$ (blue) and $^{12}\mathrm{C}(\gamma,pp)$ (blue) cross section as a function of the radial coordinate r. The kinematic conditions are those of Figs. 3.20 and 3.23. We consider one- and two-nucleon removal from the $1p3/2$-shell. The RPWIA result is displayed in red. The black solid line shows $r^2\rho(r)$ for the $^{12}\mathrm{C}$ nucleus. The ordinate is given for $r^2\rho(r)$. The $\delta(r)$ are plotted in units fm^2 up to an arbitrary scaling factor.

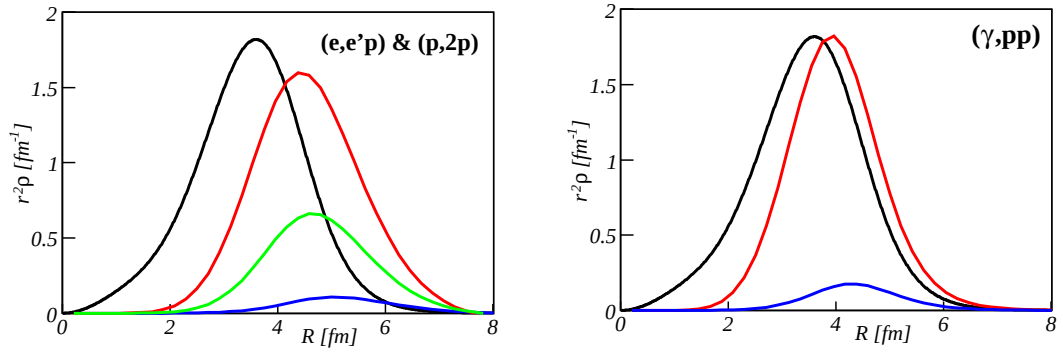

Figure 3.26 Contribution to the exclusive $^{56}\mathrm{Fe}(e,e'p)$ (green) , $^{56}\mathrm{Fe}(p,2p)$ (blue) and $^{56}\mathrm{Fe}(\gamma,pp)$ (blue) cross section as a function of the radial coordinate r. The kinematic conditions are those of Figs. 3.22 and 3.24. We consider one- and two-nucleon removal from the $1f7/2$-shell. The RPWIA result is displayed in red. The black solid line shows $r^2\rho(r)$ for the $^{56}\mathrm{Fe}$ nucleus. The ordinate is given for $r^2\rho(r)$. The $\delta(r)$ are plotted in units fm^2 up to an arbitrary scaling factor.

Chapter 4

Conclusions

In this work, we have addressed the issue of the crossover between the hadronic and partonic degrees of freedom. To study this crossover, we outlined a relativistic and quantum mechanical framework based on hadronic degrees of freedom. It was employed in this thesis to describe single pion, pion-nucleon and two-nucleon removal reactions from nuclear targets. For these removal reactions, sophisticated calculations were compared to data taken in the search for the onset of QCD phenomena at intermediate energies. Such an onset (e.g. of the color transparency effect) manifests itself in deviations between these data and our calculations.

The model used to perform the calculations is devoid of free parameters and both kinematics and dynamics are treated in a relativistic manner. The relativistic bound-state wave functions for the nucleons in the initial and residual nucleus are obtained in an independent particle model, based on the Hartree approximation to the $\sigma - \omega$ model [146]. We treat the interaction of the incoming beam with the target nucleus in the impulse approximation. The effect of final-state interactions on the detected nucleons and pions is described in the eikonal approximation. Originating from optics, this eikonal approximation is a semi-classical method that uses linear trajectories for particles that are subject to elastic and mildly inelastic rescattering over small angles. Typically, the wavelength of the incoming particle is small in comparison with the range of the scattering potential.

At sufficiently high nucleon and pion energies, the intranuclear attenuation on the ejected particles can be computed with a relativistic version of the Glauber model dubbed RMSGA. The attenuating effect of the medium on the ejected particles is computed by means of a Glauber phase operator. The numerical computation of the latter, requires knowledge about $\pi N \rightarrow \pi N$ and $N'N \rightarrow N'N$ scattering data. In contrast to the models available in the literature, which adopt a semi-classical approach, our description of the FSI mechanisms is quantum mechanical and relativistic. For nucleons with low momenta

where the conditions to apply a Glauber approach are not valid anymore, the framework offers the flexibility to compute the effect of FSI in a ROMEA model. The ROMEA model incorporates the FSI with the help of optical potentials, adopting an eikonal approximation. These optical potentials are based on global fits to elastic nucleon-nucleus scattering data (as opposed to the nucleon-nucleon scattering approach of the RMSGA). Analysis of the RMSGA FSI factor, that contains all the medium attenuation for an escaping nucleon and pion, showed that the effect of distortions (both in the norm and the phase of the FSI factor) grows when larger amounts of nuclear matter are transversed. The biggest attenuations occurred when the particles transverse long chunks of nuclear material. The effect of short-range correlations on the FSI can also be included in our model calculations. This was done by replacing the nuclear density in the integrations of the FSI factor with a modified one, accounting for the presence of a nucleon at the point of the hard interaction in the removal process, along the lines of Ref. [124]. A hole is introduced in this modified density that reflects the hard core of the nucleon-nucleon interaction, and densities are enhanced at the edge of this hole. Normalization of this modified density was ensured by the introduction of a $\gamma(\vec{r})$ function, and a solution for this function was found through solving an integral equation.

We performed transparency calculations for kinematics corresponding to completed and planned experiments [47, 49, 50, 126]. These transparency experiments are looking for the onset of color transparency. We implemented the CT effect in our model via the quantum diffusion model of Farrar *et al.* [111]. This replaces the total cross section parameter in the Glauber profile function with an effective one. This effective cross section evolves from a reduced value (accounting for the reduced interaction of a color transparent PLC) to the normal value along a certain formation length.

Our pion electroproduction transparency calculations including the CT effect are in good agreement with the data taken at Jefferson Lab [50]. Both the energy dependence and the A dependence of the transparency show deviations from the traditional nuclear physics expectations and are in agreement with calculations including the effect of CT. The quality of agreement with the JLab data [47] was worse for the pion photoproduction calculations. The calculations overpredict the measured ^{4}He$(\gamma, p\pi^-)$ transparencies and fall short in reproducing their low-$|t|$ dependence. At higher values of $|t|$, the slope of the calculations including CT is in better agreement with the data than those without. In order to check the robustness of our results, we compared the Glauber and optical-potential based models for nucleon momenta where both approaches can be applied. The calculations predicted transparencies in ^{4}He that follow similar trends in both models. The differences in the magnitude of the transparency are smaller than 5% and shrink with higher nucleon momentum.

Our RMSGA predictions for the pion electroproduction transparencies are also in reasonable agreement with the semiclassical results of Larson, Miller and Strikman. Both models predict similar trends, with the RMSGA predictions for the pion transparencies being systematically $\sim 5\%$ higher. This provides strong support for that the baseline nuclear-physics transparencies can be computed in a rather model-independent fashion. Better opportunities to study the onset of CT phenomena will become available at the upgraded Jefferson Lab facility. We predict an increase of the transparency of over 20 % at the highest energies due to color transparency. Transparencies are also enhanced through the inclusion of SRC effects in the calculations. This yields an increase of about 5%, independent of the hard-scale. Accordingly, the SRC and CT mechanisms can be clearly separated.

For the photo-induced two-proton knockout reaction, we performed calculations in kinematics corresponding to an experiment completed at JLab and currently undergoing analysis [49]. Our model for two-nucleon knockout accomodates two competing reaction mechanisms, one of the single-step (or direct) type, and one of the two-step type. The single-step mechanism describes the process as the knockout of a correlated pair, residing in a relative S-state. The two-step mechanism uses a hard rescattering mechanism, whereby the nucleon that interacts with the incoming photon knocks out a second nucleon on its way out of the nucleus. Transparency calculations confirmed the trends established in the pion photoproduction calculations with a transparency rising for low $|t|$. The magnitude of the transparency, however, was lower than what could be naively expected from the $A(e,e'p)$ values. For the knockout of a relative S pair, this was due to the reaction probing high density regions. For the hard rescattering reaction, excluding the FSI of the intermediate nucleon propagator increased the transparency with around 5%. Transparencies values in the rescattering model were lower than those for the knockout of a correlated pair, implying even higher density regions are probed in this reaction mechanism.

Finally, we exploited the robustness and multifaceted properties of the relativistic Glauber framework to make a comparative and consistent study of the effective nuclear densities that can be probed in $(p,2p)$, $(e,e'p)$ and (γ,pp) reactions. As representative examples we selected a carbon and iron target and ejected proton kinetic energies of 1.5 GeV. The $(e,e'p)$ reaction has the potential to probe reasonable densities. Of all reactions considered, the (γ,pp) reaction is the one that can get closest to the deep nuclear interior. The $(p,2p)$ reaction is subject to large attenuation, but a high resolution experiment picking protons from s-orbits in ^{12}C, for example, can probe densities that are of the order of 30% of the nuclear saturation density. Calculations in iron showed similar trends, but the reduction of the effectively probed densities in $(e,e'p)$ and $(p,2p)$ compared to (γ,pp) was less pronounced than in carbon. These findings are of importance for ongoing and planned searches of

nuclear effects at small distance scales.

Outlook

In order to establish the onset of CT effect on a firm footing, it is important to extend the pion transparency measurements to higher energies, where the largest CT effects are predicted. The upgrade of Jefferson Lab to 12 GeV that is currently underway will make this possible and experiments are already being planned. We can also extend our model to include reactions with a kaon or rho meson in the final state, so that it allows us to perform calculations for the completed JLab experiment [45]. As experimental information about kaon-nucleon and rho-nucleon scattering is rather limited, the parameters entering the Glauber phase are not as well determined as for the nucleon and pion. There is still room for improvement in the two-nucleon knockout calculations. For instance, the two competing reaction mechanisms can be combined on amplitude level and the resulting interference effects can be studied.

Other improvements and extensions to the model can also be made. Realistic wave functions for light nuclei could be included. The description of the correlations in the FSI could be improved through the inclusion of tensor correlations. However, we estimate that the correction due to the tensor correlations would be small, as the medium-range character of these correlations reaches beyond the small transverse range of the Glauber FSI. As correlations imply high density fluctuations, there is also the possibility to include a model for the correlations that departs from partonic degrees of freedom. In combination with the hadronic picture used in this work, this would give us a kind of hybrid model wherein the two approaches could be compared with each other and with results from experiments.

Appendix A

Notations and Abbreviations

Notations

The spin vector operator acts on two component spinors and is defined as

$$\vec{\sigma} = (\sigma_x, \sigma_y, \sigma_z) = \sigma^i \vec{e}_i \equiv (\vec{\sigma} \cdot \vec{e}_i^{\dagger})\vec{e}_i \,, \tag{A.1}$$

where the Pauli matrices are given by

$$\sigma_x = \begin{pmatrix} 0 & 1 \\ 1 & 0 \end{pmatrix}, \quad \sigma_y = \begin{pmatrix} 0 & -i \\ i & 0 \end{pmatrix}, \quad \sigma_z = \begin{pmatrix} 1 & 0 \\ 0 & -1 \end{pmatrix}. \tag{A.2}$$

The Dirac or γ matrices are defined by the anticommutation relations

$$\{\gamma^\mu, \gamma^\nu\} = 2g^{\mu\nu} \,. \tag{A.3}$$

In the Pauli-Dirac representation used throughout this work, they are written as

$$\gamma^0 = \begin{pmatrix} \mathbb{1} & 0 \\ 0 & -\mathbb{1} \end{pmatrix}, \quad \gamma^i = \begin{pmatrix} 0 & \sigma_i \\ -\sigma_i & 0 \end{pmatrix}. \tag{A.4}$$

γ^5 is defined as

$$\gamma^5 = i\gamma^0\gamma^1\gamma^2\gamma^3 \,, \tag{A.5}$$

and the commutators $\sigma^{\mu\nu}$ as

$$\sigma^{\mu\nu} = \frac{i}{2}\left[\gamma^\mu, \gamma^\nu\right] . \tag{A.6}$$

The matrices β and α_i are defined as

$$\beta = \gamma^0 , \quad \vec{\alpha}\gamma^0\vec{\gamma} . \tag{A.7}$$

Abbreviations

BNL	Brookhaven National Laboratory
c.m.	center of mass
CT	color transparency
EA	eikonal approximation
FSI	final-state interactions
GPD	generalized parton distribution
HRM	hard rescattering model
IA	impulse approximation
IPM	independent particle model
ISI	initial state reactions
LRC	long-range correlations
MAMI	Mainz microtron
NIKHEF	Nationaal Instituut voor Kernfysica en Hoge-energiefysica
PLC	point-like configuration
pQCD	perturbative quantum chromodynamics
QCD	quantum chromodynamics
QED	quantum electrodynamics
(R)DWIA	(relativistic) distorted-wave impulse approximation
RMSGA	relativistic multiple-scattering Glauber approximation
ROMEA	relativistic optical model eikonal approximation
(R)PWIA	(relativistic) plain-wave impulse approximation
SRC	short-range correlations

Appendix B

Relativistic Bound-State Wave Functions

The wave functions for the bound nucleons are constructed in an independent-particle model (IPM). We use relativistic wave functions from the Hartree approximation to the Walecka model with the W1 parametrization [146]. For the sake of conciseness of the notation, only the spatial coordinates of the nucleons are written throughout this work. The single-particle wave functions ϕ_α adopt the following form for a spherically symmetric nuclear potential [147]:

$$\phi_\alpha(\vec{r}) \equiv \phi_{n\kappa m}(\vec{r},\vec{\sigma}) = \begin{bmatrix} i\frac{G_{n\kappa}(r)}{r}\mathscr{Y}_{\kappa m}(\Omega,\vec{\sigma}) \\ -\frac{F_{n\kappa}(r)}{r}\mathscr{Y}_{-\kappa m}(\Omega,\vec{\sigma}) \end{bmatrix}. \tag{B.1}$$

Here, n is the principal quantum number and κ and m denote the generalized angular momentum quantum numbers. The spin spherical harmonics $\mathscr{Y}_{\pm\kappa m}$ are defined as:

$$\begin{aligned} \mathscr{Y}_{\kappa m}(\Omega,\vec{\sigma}) &= \sum_{m_l m_s} \langle l m_l \tfrac{1}{2} m_s | j m\rangle Y_{l m_l}(\Omega)\chi_{\frac{1}{2}m_s}(\vec{\sigma}), \\ \mathscr{Y}_{-\kappa m}(\Omega,\vec{\sigma}) &= \sum_{m_l m_s} \langle \bar{l} m_l \tfrac{1}{2} m_s | j m\rangle Y_{\bar{l} m_l}(\Omega)\chi_{\frac{1}{2}m_s}(\vec{\sigma}), \end{aligned} \tag{B.2}$$

$$\text{with} \quad j = |\kappa| - \frac{1}{2}, \quad l = \begin{cases} \kappa, & \kappa > 0 \\ -\kappa - 1, & \kappa < 0 \end{cases}, \quad \bar{l} = \begin{cases} \kappa - 1, & \kappa > 0 \\ -\kappa, & \kappa < 0 \end{cases}.$$

The Fourier transform of the bound-state wave functions (B.1) is given by

$$\phi_\alpha(\vec{p}) = \int d\vec{r}\, e^{-i\vec{r}\cdot\vec{p}}\phi_\alpha(\vec{r}) = (-i)^l (2\pi)^{3/2} \begin{bmatrix} g_{n\kappa(p)}\mathscr{Y}_{\kappa m}(\Omega_p) \\ -S_\kappa f_{n\kappa(p)}\mathscr{Y}_{-\kappa m}(\Omega_p) \end{bmatrix}, \tag{B.3}$$

with $S_\kappa = \kappa/|\kappa|$. The radial functions $g_{n\kappa}(\vec{p})$ and $f_{n\kappa}(\vec{p})$ are defined by

$$g_{n\kappa}(\vec{p}) = \sqrt{\frac{2}{\pi}} \int_0^\infty r^2 dr \frac{G_{n\kappa}(r)}{r} j_l(pr), \tag{B.4}$$

$$f_{n\kappa}(\vec{p}) = \sqrt{\frac{2}{\pi}} \int_0^\infty r^2 dr \frac{F_{n\kappa}(r)}{r} j_l(pr), \tag{B.5}$$

with $j_l(pr)$ the spherical Bessel function of the first kind.

Appendix C

Klein-Gordon Scattering

We consider the relativistic scattering of a spinless particle with mass m in the presence of a potential $V(r)$. The time-independent Klein-Gordon equation of the system is given by

$$(\hat{p}^2 + m^2)\psi(\vec{r}) = (E - V(r))^2\psi(\vec{r}), \tag{C.1}$$

with $E = \sqrt{k^2 + m^2}$ and $\hat{\vec{p}}$ the momentum operator. We consider an incoming plane wave

$$\Phi_{\vec{k}_i}(\vec{r}) = \frac{1}{(2\pi)^{3/2}} e^{i\vec{k}_i\cdot\vec{r}}, \tag{C.2}$$

and a scattering wave function that obeys the asymptotic boundary condition

$$\psi^{(+)}_{\vec{k}_i}(\vec{r}) \xrightarrow[r\to\infty]{} A\left(e^{i\vec{k}_i\cdot\vec{r}} + f(\Omega)\frac{e^{ikr}}{r}\right). \tag{C.3}$$

Here, A is a normalization factor, $f(\Omega)$ is the scattering amplitude, and we assume that the potential $V(r)$ vanishes faster than r^{-1} for $r \to \infty$. The conserved probability current associated with the Klein-Gordon Eq. (C.1) is

$$j_\mu(\vec{r}) = -\frac{i}{2m}\left[\left(\psi^\dagger(\vec{r})\right)\nabla_\mu\psi(\vec{r}) - \psi(\vec{r})\left(\nabla_\mu\psi^\dagger(\vec{r})\right)\right]. \tag{C.4}$$

After a derivation similar to the one made for the Schrödinger case in [103], one readily finds

$$\frac{d\sigma}{d\Omega} = |f(\Omega)|^2. \tag{C.5}$$

We can write Eq. (C.1) as

$$(E^2 - \hat{p}^2)\psi(\vec{r}) = (2EV(r) - V^2(r))\psi(\vec{r}), \tag{C.6}$$

and its solution as an integral equation

$$\psi^{(+)}_{\vec{k}_i}(\vec{r}) = \frac{1}{(2\pi)^{3/2}} e^{i\vec{k}_i\cdot\vec{r}} + \int d\vec{r}' G^{(+)}_0(\vec{r},\vec{r}')(2EV(r') - V(r')^2)\psi^{(+)}_{\vec{k}_i}(\vec{r'}) \,. \tag{C.7}$$

When adopting the following form of the Green's function

$$G^{(+)}_0(\vec{r},\vec{r}') = -\frac{1}{4\pi}\frac{e^{ik|\vec{r}-\vec{r}'|}}{|\vec{r}-\vec{r}'|} \,, \tag{C.8}$$

the wave function $\psi^{(+)}_{\vec{k}_i}(\vec{r})$ has the asymptotic form of Eq. (C.3) For $r \to \infty$, we can write Eq. (C.7) as

$$\psi^{(+)}_{\vec{k}_i}(\vec{r}) \to \frac{1}{(2\pi)^{3/2}} e^{i\vec{k}_i\cdot\vec{r}} + \frac{e^{ikr}}{r}\left[-\frac{1}{4\pi}\int d\vec{r'} e^{-i\vec{k}_f\cdot\vec{r'}}(2EV(r') - V^2(r'))\psi^{(+)}_{\vec{k}_i}(\vec{r'})\right] \,, \tag{C.9}$$

where $\vec{k}_f = k\vec{r}/r$. Comparing this with Eq. (C.3) and taking $A = (2\pi)^{-3/2}$ gives us

$$f(\Omega) = -(2\pi)^2 E\langle \Phi_{\vec{k}_f} \mid V - \frac{V^2}{2E} \mid \psi^{(+)}_{\vec{k}_i}\rangle \,. \tag{C.10}$$

If the wavelength of the incident particle is sufficiently short in comparison with the distance in which the potential varies ($ka \gg 1$, with a the typical range of the potential, and $V/E \ll 1$), the eikonal approximation can be used. Scattering is assumed to occur over small angles and we can write

$$\hat{p}^2 = [(\hat{\vec{p}} - \vec{K}) + \vec{K}] \approx 2\vec{K}\cdot\hat{\vec{p}} - K^2 \,, \tag{C.11}$$

with

$$\vec{K} = \frac{\vec{k}_i + \vec{k}_f}{2} \,. \tag{C.12}$$

This allows us to write Eq. (C.1) as

$$\left[\vec{K}\cdot\hat{\vec{p}} - K^2 - \frac{V^2(r)}{2} + V(r)E\right]\psi(\vec{r}) = 0 \,. \tag{C.13}$$

Employing the eikonal ansatz for the scattering wave function

$$\psi_{\vec{k}_i} = \frac{1}{(2\pi)^{3/2}} e^{i\vec{k}_i\cdot\vec{r}} e^{iS(r)} \,, \tag{C.14}$$

and substituting it in Eq. (C.13) yields the following equation for the eikonal phase $S(r)$

$$\vec{K}\cdot\vec{\nabla}S(r) = \frac{V^2(r)}{2} - V(r)E \,. \tag{C.15}$$

If we choose the z-axis along $\vec{K}$, we obtain (with $\vec{b}$ perpendicular to the z-axis)

$$iS(r) = \frac{i}{K}\int_{-\infty}^{z} dz' \left(\frac{V^2(\vec{b},z')}{2} - V(\vec{b},z')E \right) . \tag{C.16}$$

We can now write the scattering amplitude of Eq. (C.10) as

$$f(\Omega) = -\frac{E}{2\pi}\int d\vec{b} e^{i\vec{q}\cdot\vec{b}} \int dz e^{iS(r)} \left(V(r) - \frac{V^2(r)}{2E} \right) , \tag{C.17}$$

where $\vec{q} = \vec{k}_i - \vec{k}_f$. To simplify this last equation, we can make use of

$$\left(V(r) - \frac{V^2(r)}{2E} \right) e^{iS(r)} = \frac{iK}{E}\frac{de^{iS(r)}}{dz} \tag{C.18}$$

to write

$$f(\Omega) = \frac{K}{2\pi i}\int db^2 e^{i\vec{q}\cdot\vec{b}} \left(e^{i\chi(\vec{b})} - 1 \right) , \tag{C.19}$$

with

$$\chi(\vec{b}) = \frac{1}{K}\int_{-\infty}^{\infty} dz' \left(\frac{V^2(\vec{b},z')}{2} - V(\vec{b},z')E \right) . \tag{C.20}$$

Appendix D

NN Amplitudes: Representations

The helicity amplitudes for the free nucleon-nucleon scattering process are defined as

$$\mathscr{M}_{\lambda_1'\lambda_2';\lambda_1\lambda_2} = [\bar{u}_{\lambda_1'}(\vec{p'}_1)]_\alpha [\bar{u}_{\lambda_2'}(\vec{p'}_2)]_\beta \mathscr{D}^{NN}_{\alpha\beta;\gamma\delta} [u_{\lambda_1}(\vec{p}_1)]_\gamma [u_{\lambda_2}(\vec{p}_2)]_\delta \,, \tag{D.1}$$

where λ denotes the helicity of the spinor. They can be expanded into a partial wave sum as

$$\mathscr{M}_{\lambda_1'\lambda_2';\lambda_1\lambda_2} = \frac{1}{2ik}\sum_J (2J+1)\langle \lambda_1'\lambda_2' \mid T^J(E) \mid \lambda_1\lambda_2\rangle d^J_{\mu\nu}(\theta), \tag{D.2}$$

with k and θ the momentum and scattering angle in the center of mass frame and $\mu = \lambda_1 - \lambda_2$, $\nu = \lambda_1' - \lambda_2'$. The Wigner D-matrices $d^J_{\mu\nu}(\theta)$ satisfy

$$d^J_{\mu\nu}(\theta) = (-1)^{\lambda-\mu} d^J_{\nu\mu}(\theta) = (-1)^{\lambda-\mu} d^J_{-\nu-\mu}(\theta)\,. \tag{D.3}$$

Parity, time-reversal and particle exchange symmetries can respectively be used to write

$$\begin{aligned}
\langle \lambda_1'\lambda_2' \mid T^J(E) \mid \lambda_1\lambda_2\rangle &= \langle -\lambda_1' - \lambda_2' \mid T^J(E) \mid -\lambda_1 - \lambda_2\rangle\,,\\
\langle \lambda_1'\lambda_2' \mid T^J(E) \mid \lambda_1\lambda_2\rangle &= \langle \lambda_1\lambda_2 \mid T^J(E) \mid \lambda_1'\lambda_2'\rangle\,,\\
\langle \lambda_1'\lambda_2' \mid T^J(E) \mid \lambda_1\lambda_2\rangle &= \langle \lambda_2'\lambda_1' \mid T^J(E) \mid \lambda_2\lambda_1\rangle\,.
\end{aligned} \tag{D.4}$$

By using Eqs. (D.3) and (D.4) in Eq. (D.2), the total helicity amplitudes satisfy

$$\begin{aligned}
\langle -\lambda_1' - \lambda_2' \mid T^J(E) \mid -\lambda_1 - \lambda_2\rangle &= (-1)^{\lambda_1-\lambda_2-\lambda_1'+\lambda_2'} \langle \lambda_1'\lambda_2' \mid T^J(E) \mid \lambda_1\lambda_2\rangle\,,\\
\langle \lambda_1\lambda_2 \mid T^J(E) \mid \lambda_1'\lambda_2'\rangle &= (-1)^{\lambda_1-\lambda_2-\lambda_1'+\lambda_2'} \langle \lambda_1'\lambda_2' \mid T^J(E) \mid \lambda_1\lambda_2\rangle\,,\\
\langle \lambda_2'\lambda_1' \mid T^J(E) \mid \lambda_2\lambda_1\rangle &= (-1)^{\lambda_1-\lambda_2-\lambda_1'+\lambda_2'} \langle \lambda_1'\lambda_2' \mid T^J(E) \mid \lambda_1\lambda_2\rangle\,.
\end{aligned} \tag{D.5}$$

These symmetry relations can be used to reduce the total amount of independent helicity amplitudes from 16 to 5:

$$
\begin{aligned}
a &\equiv \mathcal{M}_{1,1;1,1} = \mathcal{M}_{-1,-1;-1,-1}\,,\\
b &\equiv \mathcal{M}_{1,1;1,-1} = \mathcal{M}_{1,-1;1,1} = \mathcal{M}_{1,1;-1,1} = \mathcal{M}_{-1,1;1,1}\\
&= \mathcal{M}_{-1,-1;-1,1} = \mathcal{M}_{-1,-1;1,-1} = \mathcal{M}_{-1,1;-1,-1} = \mathcal{M}_{1,-1;-1,-1}\,,\\
c &\equiv \mathcal{M}_{1,-1;1,-1} = \mathcal{M}_{-1,1;-1,1}\,,\\
d &\equiv \mathcal{M}_{1,1;-1,-1} = \mathcal{M}_{-1,-1;1,1}\,,\\
e &\equiv \mathcal{M}_{1,-1;-1,1} = \mathcal{M}_{-1,1;1,-1}\,.
\end{aligned}
\tag{D.6}
$$

These five helicity amplitudes are available online from the SAID database [67] for lab momentum up to 2 GeV. After substituting Eq. (2.75) in Eq. (D.1) for these five amplitudes and solving for the Fermi invariants, one gets [95]

$$
\begin{pmatrix} \mathcal{F}_S \\ \mathcal{F}_V \\ \mathcal{F}_T \\ \mathcal{F}_P \\ \mathcal{F}_A \end{pmatrix} = \frac{1}{s-4m^2} \begin{pmatrix} a_{11} & a_{12} & a_{13} & a_{14} & a_{15} \\ a_{21} & a_{22} & a_{23} & a_{24} & a_{25} \\ a_{31} & a_{32} & a_{33} & a_{34} & a_{35} \\ a_{41} & a_{42} & a_{43} & a_{44} & a_{45} \\ a_{51} & a_{52} & a_{53} & a_{54} & a_{55} \end{pmatrix} \begin{pmatrix} a \\ b \\ c \\ d \\ e \end{pmatrix}\,,
\tag{D.7}
$$

with

$$
\begin{aligned}
a_{11} &= -a_{24} = a_{25} = -2a_{31} = a_{41} = -a_{54} = a_{55} = -\frac{2m^4}{s}\,,\\
a_{14} &= -a_{15} = -a_{21} = -2a_{34} = 2a_{35} = a_{44} = -a_{51} = \frac{2m^4}{s} - m^2\,,\\
a_{12} &= \frac{m\left(8m^2 - (3+\cos\theta)s\right)}{\sqrt{s}\sin\theta}\,,\\
a_{13} &= \frac{m^2\left(2m^2(1+\cos\theta) - s(3+\cos\theta)\right)}{s(1+\cos\theta)}\,,\\
a_{22} &= \frac{4m^3(1+\cos\theta)}{\sqrt{s}\sin\theta}\,,\\
a_{23} &= \frac{2m^2\left(m^2(1+\cos\theta)+s\right)}{s(1+\cos\theta)}\,,\\
a_{32} &= -\frac{m\sqrt{s}(1-\cos\theta)}{2\sin\theta}\,,\\
a_{33} &= -\frac{m^2\left(2m^2(1+\cos\theta)+s(1-\cos\theta)\right)}{2s(1+\cos\theta)}\,,\\
a_{42} &= -\frac{m\left(8m^2+s(3+\cos\theta)\right)}{\sqrt{s}\sin\theta}\,,
\end{aligned}
$$

$$
\begin{aligned}
a_{43} &= \frac{m^2\left(2m^2(1+\cos\theta)-s(3+\cos\theta)\right)}{s(1+\cos\theta)}\,,\\
a_{45} &= -\frac{m^2\left(2m^2(1-\cos\theta)+s(7+\cos\theta)\right)}{s(1-\cos\theta)}\,,\\
a_{52} &= -\frac{4m^3(1-\cos\theta)}{\sqrt{s}\sin\theta}\,,\\
a_{53} &= \frac{2m^2\left(m^2(1+\cos\theta)-s\right)}{s(1+\cos\theta)}\,.
\end{aligned}
\tag{D.8}
$$

In all these equations θ is the scattering angle in the center of mass system and s is the Mandelstam variable.

Appendix E

Parametrization of the pion electroproduction cross section

With the notations used in subsec. 2.1.2, the pion electroproduction cross section of Eq. (2.46), can be written as the product of the electron fluxfactor with the sum of four response functions:

$$\frac{d^5\sigma^{eN}}{dE_{e'}d\Omega_{e'}d|t|d\phi_\pi^*} = \Gamma'\left(\frac{d\sigma_T^{eN}}{d|t|} + \epsilon\frac{d\sigma_L^{eN}}{d|t|} + \epsilon\frac{d\sigma_{TT}^{eN}}{d|t|}\cos 2\phi_\pi^* + \sqrt{\epsilon(\epsilon+1)}\frac{d\sigma_{TL}^{eN}}{d|t|}\cos\phi_\pi^*\right). \quad \text{(E.1)}$$

In JLab experiment E01-004, that measured the pion charge form factor through pion electroproduction, the four response functions in Eq. (E.1) were initially parametrized as [129]

$$\begin{aligned}
\frac{d\sigma_T^{eN}}{d|t|} &= f(s')\left(4.5/Q^2 + 2/Q^4\right), \\
\frac{d\sigma_L^{eN}}{d|t|} &= f(s')350Q^2\frac{e^{-t(16-7.5\ln Q^2)}}{(1+1.77Q^2+0.05Q^4)^2}, \\
\frac{d\sigma_{TT}^{eN}}{d|t|} &= -f(s')\frac{5}{Q^4}\frac{|t|}{(|t|+0.02)^2}\sin\theta_\pi^{*2}, \\
\frac{d\sigma_{TL}^{eN}}{d|t|} &= f(s')\left(e^{0.79-\frac{3.4}{\sqrt{Q^2}}t} + 1.1 - 3.6/Q^4\right)\sin\theta_\pi^*. \quad \text{(E.2)}
\end{aligned}$$

Here, θ_π^* denotes the pion angle with the virtual photon in the pion-nucleon c.o.m. frame and the dependence on the Mandelstam variable $s' = (p_N^\mu + p_\pi^\mu)^2$ is assumed to have the following t-pole dependence

$$f(s') = \frac{8.539}{2\pi(s'-m_N^2)^2}. \quad \text{(E.3)}$$

For the pion electroproduction transparency experiment, a multiplicative correction function was applied to the parametrization of Eq. (E.1) for each Q^2 setting to make the Monte Carlo distributions match the data [128]. These functions for each Q^2 setting are as follows (with $W = \sqrt{s'}$):

$$\begin{aligned}
Q^2 = 1.10(\mathrm{GeV/c})^2 \quad \rightarrow \quad & (-47.5984 + 43.4145W - 9.64264W^2) \\
& \times (1.32289 - 0.698424Q^2 + 0.35561Q^4) \\
& \times (1.17152 - 7.03367t + 52.053t^2) \\
& \times (1.0612 + 0.147858\cos\phi^*_\pi - 0.0430268\cos 2\phi^*_\pi) \\
Q^2 = 2.15(\mathrm{GeV/c})^2 \quad \rightarrow \quad & (-23.1723 + 20.6505W - 4.37408W^2) \\
& \times (2.29646 - 1.11745Q^2 + 0.229736Q^4) \\
& \times (0.704879 + 1.61954t + 0.0859429t^2) \\
& \times (0.979176 + 0.044882\cos\phi^*_\pi - 0.0743073\cos 2\phi^*_\pi) \\
Q^2 = 3.00(\mathrm{GeV/c})^2 \quad \rightarrow \quad & (-6.14191 + 5.64149W - 1.0843W^2) \\
& \times (2.43486 - 0.888779Q^2 + 0.136267Q^4) \\
& \times (0.745356 + 1.22215t - 1.24105t^2) \\
& \times (0.962609 - 0.0608404\cos\phi^*_\pi - 0.0084712\cos 2\phi^*_\pi) \\
Q^2 = 4.00(\mathrm{GeV/c})^2 \quad \rightarrow \quad & (-7.8696 + 6.48878W - 1.16624W^2) \\
& \times (-0.703888 + 0.814839Q^2 - 0.0957087Q^4) \\
& \times (0.723372 + 0.140101t + 0.809151t^2) \\
& \times (1.00054 - 0.100002\cos\phi^*_\pi + 0.00780768\cos 2\phi^*_\pi) \\
Q^2 = 4.80(\mathrm{GeV/c})^2 \quad \rightarrow \quad & (-11.1202 + 9.4995W - 1.86788W^2) \\
& \times (2.27339 - 0.469771Q^2 + 0.0421723Q^4) \\
& \times (1.08961 - 1.06851t + 1.36125t^2) \\
& \times (0.89789 - 0.118188\cos\phi^*_\pi - 0.0350948\cos 2\phi^*_\pi)\,.
\end{aligned} \tag{E.4}$$

Bibliography

[1] E. Rutherford. The scattering of α and β particles by matter and the structure of the atom. *Philosophical Magazine*, 21:669–688, 1911.

[2] J. Chadwick. Possible existence of a neutron. *Nature,* 129:312, 1932.

[3] H. Yukawa. On the Interaction of Elementary Particles. I. *Proc. Phys.-Math. Soc. Jpn.*, 17:48, 1935.

[4] M. Xu, M. Yu, and L. Liu. Examining the crossover from the hadronic to partonic phase in qcd. *Physical Review Letters*, 100(9):092301, 2008.

[5] G. A. Miller. Colour transparency, in *Close, Frank (ed.) et al.: Electromagnetic interactions and hadronic structure* 457-494. 2007.

[6] F. Close, S. Donnachie, and G. Shaw. *Electromagnetic Interactions and Hadronic Structure*. Cambridge University Press, 2007.

[7] A. Mueller. *Proceedings of the Seventeenth Rencontre de Moriond, Moriond*, page 13, 1982.

[8] S. J. Brodsky, G. T. Bodwin, and G. P. Lepage. Breakdown of QCD factorization theorems for inclusive react ions. *Proceedings of the 13th Int. Symp. on Multiparticle Dynamics, Volendam*, page 963, 1982.

[9] Chudakov, A. E. . *Bull. Acad. Sci. USSR, Phys. Ser.*, 19:589, 1955.

[10] Perkins, D. H. Ionization at the origin of electron pairs, and the lifetime of the neutral pion. *Philosophical Magazine*, 46(381):1146–1148, 1955.

[11] P. L. Jain. Nucleon-Nucleon Interactions at Energies Greater than 1012 eV. *Phys. Rev.*, 125(2):679–687, Jan 1962.

[12] T. Virkus *et al.* Direct measurement of the Chudakov effect. *Phys. Rev. Lett.*, 100: 164802, 2008.

[13] A. Belkacem and A. H. Sørensen. The pair-production channel in atomic processes. *Radiation Physics and Chemistry*, 75(6):656 – 695, 2006. Pair Production.

[14] Mandal, Sourav K. and Klein, Spencer R. and Jackson, J. David. Cherenkov radiation from e^+e^- pairs and its effect on νe induced showers. *Phys. Rev. D*, 72(9):093003, Nov 2005.

[15] Nemenov, L. L. Superpenetration of ultrarelativistic positronium atoms. *Sov. J. Nucl. Phys.*, 34:726, 1981.

[16] G. D. Alekseev *et al.* Observation of ultrarelativistic positronium. *Sov. J. Nucl. Phys.*, 40:87, 1984.

[17] L. G. Afanasév *et al.* Measurement of the cross section for interaction of ultrarelativistic positronium atoms with carbon. *Sov. J. Nucl. Phys.*, 50:4, 1989.

[18] Nemenov, L. L. Time-of-formation effects in ultrarelativistic positronium. *Sov. J. Nucl. Phys.*, 51:284, 1990.

[19] L. L. Frankfurt and M. I. Strikman. High-Energy Phenomena, Short Range Nuclear Structure and QCD. *Phys. Rept.*, 76:215–347, 1981.

[20] L. Frankfurt and M. Strikman. Color screening and color transparency in hard nuclear processes. *Prog. Part. Nucl. Phys.*, 27:135–193, 1991.

[21] L. Frankfurt, W. R. Greenberg, G. A. Miller, and M. Strikman. Sum rule description of color transparency. *Phys. Rev.*, C46:2547–2553, 1992.

[22] L. L. Frankfurt, G. A. Miller, and M. Strikman. The Geometrical color optics of coherent high-energy processes. *Ann. Rev. Nucl. Part. Sci.*, 44:501–560, 1994.

[23] L. L. Frankfurt and M. I. Strikman. Hard Nuclear Processes and Microscopic Nuclear Structure. *Phys. Rept.*, 160:235–427, 1988.

[24] S. J. Brodsky and A. H. Mueller. Using Nuclei to Probe Hadronization in QCD. *Phys. Lett.*, B206:685, 1988.

[25] L. Frankfurt, G. A. Miller, and M. Strikman. Color transparency phenomenon and nuclear physics. *Comments Nucl. Part. Phys.*, 21:1–40, 1992.

[26] L. Frankfurt, G. A. Miller, and M. Strikman. Precocious dominance of point - like configurations in hadronic form-factors. *Nucl. Phys.*, A555:752–764, 1993.

[27] S. Liuti and S. K. Taneja. Generalized parton distributions and color transparency phenomena. *Phys. Rev.*, D70:074019, 2004.

[28] M. Burkardt and G. A. Miller. Color transparent GPDs? *Phys. Rev.*, D74:034015, 2006.

[29] A. S. Carroll *et al.* Nuclear transparency to large anplge $p-p$ elastic scattering. *Phys. Rev. Lett.*, 61:1698–1701, 1988.

[30] I. Mardor *et al.* Nuclear transparency in large momentum transfer quasielastic scattering. *Phys. Rev. Lett.*, 81:5085, 1998.

[31] A. Leksanov *et al.* Energy dependence of nuclear transparency in $C(p,2p)$ scattering. *Phys. Rev. Lett.*, 87:212301, 2001.

[32] L. Frankfurt, M. Strikman, and M. Zhalov. Single particle strength restoration and nuclear transparency in high Q^2 exclusive $(e,e'p)$ reactions. *Phys. Lett.*, B503:73–80, 2001.

[33] J. P. Ralston and B. Pire. Fluctuating Proton Size and Oscillating Nuclear Transparency. *Phys. Rev. Lett.*, 61:1823, 1988.

[34] J. P. Ralston and B. Pire. Quantum chromotransparency. *Phys. Rev. Lett.*, 65:2343–2346, 1990.

[35] S. J. Brodsky and G. F. de Teramond. Spin Correlations, QCD Color Transparency and Heavy Quark Thresholds in Proton Proton Scattering. *Phys. Rev. Lett.*, 60:1924, 1988.

[36] G. Garino *et al.* Proton propagation in nuclei studied in the $(e,e'p)$ reaction. *Phys. Rev.*, C45:780–790, 1992.

[37] N. Makins *et al.* Momentum transfer dependence of nuclear transparency from the quasielastic ^{12}C$(e,e'p)$ reaction. *Phys. Rev. Lett.*, 72:1986–1989, 1994.

[38] T. G. O'Neill *et al.* A-dependence of nuclear transparency in quasielastic $A(e,e'p)$ at high Q^2. *Phys. Lett.*, B351:87–92, 1995.

[39] D. Abbott *et al.* Quasifree $(e,e'p)$ reactions and proton propagation in nuclei. *Phys. Rev. Lett.*, 80:5072–5076, 1998.

[40] K. Garrow *et al.* Nuclear transparency from quasielastic $A(e,e'p)$ reactions up to $Q^2 = 8.1$ (GeV/c)^2. *Phys. Rev.*, C66:044613, 2002.

[41] D. Dutta *et al.* A study of the quasi-elastic $(e,e'p)$ reaction on ^{12}C, ^{56}Fe and ^{97}Au. *Phys. Rev.*, C68:064603, 2003.

[42] M. R. Adams *et al.* Measurement of nuclear transparencies from exclusive ρ^0 meson production in muon - nucleus scattering at 470 GeV. *Phys. Rev. Lett.*, 74:1525–1529, 1995.

[43] K. Ackerstaff *et al.* Observation of a coherence length effect in exclusive ρ^0 electroproduction. *Phys. Rev. Lett.*, 82:3025–3029, 1999.

[44] A. Airapetian *et al.* The Q^2-dependence of nuclear transparency for exclusive ρ^0 production. *Phys. Rev. Lett.*, 90:052501, 2003.

[45] J. Arrington *et al.* Q^2 dependence of nuclear transparency for incoherent ρ^0 electroproduction. 2002. JLAB-PR-02-110.

[46] E. M. Aitala *et al.* Observation of color-transparency in diffractive dissociation of pions. *Phys. Rev. Lett.*, 86:4773–4777, 2001.

[47] D. Dutta *et al.* Nuclear transparency with the gamma $n \to \pi^- p$ process in ^{4}He. *Phys. Rev.*, C68:021001, 2003.

[48] D. Margaziotis *et al.* Hard desintegration of a Proton Pair. 2003. JLAB-PR-03-005.

[49] D. Margaziotis *et al.* Hard desintegration of a Proton Pair. 2003. JLAB-PR-03-101.

[50] B. Clasie *et al.* Measurement of Nuclear Transparency for the $A(e,e'pi^+)$ Reaction. *Phys. Rev. Lett.*, 99:242502, 2007.

[51] E. C. Svensson, V. F. Sears, A. D. B. Woods, and P. Martel. Neutron-diffraction study of the static structure factor and pair correlations in liquid ^{4}He. *Phys. Rev.*, B21: 3638–3651, 1980.

[52] R. B. Hallock. X-Ray Scattering from Liquid ^{4}He. *Phys. Rev. A*, 5(1):320–330, Jan 1972.

[53] O. Benhar, V. R. Pandharipande, and S. C. Pieper. Electron-scattering studies of correlations in nuclei. *Rev. Mod. Phys.*, 65:817–828, 1993.

[54] L. Frankfurt, M. Sargsian, and M. Strikman. Recent observation of short range nucleon correlations in nuclei and their implications for the structure of nuclei and neutron stars. *Int. J. Mod. Phys.*, A23:2991–3055, 2008.

[55] S. C. Pieper, R. B. Wiringa, and V. R. Pandharipande. Variational calculation of the ground state of ^{16}O. *Phys. Rev. C*, 46(5):1741–1756, Nov 1992.

[56] C. Ciofi degli Atti and S. Simula. Realistic model of the nucleon spectral function in few- and many-nucleon systems. *Phys. Rev. C*, 53(4):1689–1710, Apr 1996.

[57] K. S. Egiyan *et al.* Measurement of 2- and 3-Nucleon Short Range Correlation Probabilities in Nuclei. *Phys. Rev. Lett.*, 96:082501, 2006.

[58] A. Tang *et al.* n p short-range correlations from (p,2p + n) measurements. *Phys. Rev. Lett.*, 90:042301, 2003.

[59] J. L. S. Aclander *et al.* The large momentum transfer reaction ^{12}C$(p, 2p + n)$ as a new method for measuring short range N N correlations in nuclei. *Phys. Lett.*, B453: 211–216, 1999.

[60] K. S. Egiyan *et al.* Observation of Nuclear Scaling in the $A(e, e')$ Reaction at x_B >1. *Phys. Rev.*, C68:014313, 2003.

[61] L. Lapikás. Quasi-elastic electron scattering off nuclei . *Nucl. Phys. A*, 553:297–308, 1993.

[62] C. Barbieri and W. H. Dickhoff. Faddeev treatment of long-range correlations and the one-hole spectral function of ^{16}O. *Phys. Rev. C*, 65(6):064313, Jun 2002.

[63] D. Rohe *et al.* Correlated Strength in Nuclear Spectral Function. *Phys. Rev. Lett.*, 93: 182501, 2004.

[64] R. Shneor *et al.* Investigation of Proton-Proton Short-Range Correlations via the ^{12}C$(e, e'pp)$ Reaction. *Phys. Rev. Lett.*, 99:072501, 2007.

[65] R. Subedi *et al.* Probing Cold Dense Nuclear Matter. *Science*, 320:1476–1478, 2008.

[66] D. Higinbotham, E. Piasetzky, and M. Strikman. Protons and neutrons cosy up in nuclei and neutron stars. *Cern Courier*, 49, 2009.

[67] URL http://gwdac.phys.gwu.edu/.

[68] J. D. Walecka. A Theory of highly condensed matter. *Annals Phys.*, 83:491–529, 1974.

[69] C. J. Horowitz and B. D. Serot. Selfconsistent Hartree Description of Finite Nuclei in a Relativistic Quantum Field Theory. *Nucl. Phys.*, A368:503, 1981.

[70] B. D. Serot and J. D. Walecka. The Relativistic Nuclear Many Body Problem. *Adv. Nucl. Phys.*, 16:1–327, 1986.

[71] R. J. Glauber. *Lectures in Theoretical Physics*. Interscience, New York, 1959.

[72] J. Ryckebusch, D. Debruyne, P. Lava, S. Janssen, B. Van Overmeire, and T. Van Cauteren. Relativistic formulation of Glauber theory for $A(e, e'p)$ reactions. *Nucl. Phys.*, A728:226–250, 2003.

[73] P. Lava, M. C. Martínez, J. Ryckebusch, J. A. Caballero, and J. M. Udias. Nuclear transparencies in relativistic $A(e, e'p)$ models. *Phys. Lett.*, B595:177–186, 2004.

[74] B. Van Overmeire, W. Cosyn, P. Lava, and J. Ryckebusch. Relativistic eikonal description of $A(p, pN)$ reactions. *Phys. Rev.*, C73:064603, 2006.

[75] B. Van Overmeire and J. Ryckebusch. A relativistic framework to determine the nuclear transparency from $A(p, 2p)$ reactions. *Phys. Lett.*, B644:304–310, 2007.

[76] J. D. Bjorken and S. D. Drell. *Relativistic Quantum Mechanics*. McGraw-Hill, New York, 1964.

[77] F. X. Lee, T. Mart, C. Bennhold, and L. E. Wright. Quasifree kaon photoproduction on nuclei. *Nucl. Phys.*, A695:237–272, 2001.

[78] N. S. Chant and P. G. Roos. Spin orbit effects in quasifree knockout reactions. *Phys. Rev. C*, 27(3):1060–1072, Mar 1983.

[79] E. D. Cooper, S. Hama, B. C. Clark, and R. L. Mercer. Global dirac phenomenology for proton nucleus elastic scattering. *Phys. Rev.*, C47:297–311, 1993.

[80] R. A. Arndt, I. I. Strakovsky, and R. L. Workman. Nucleon-nucleon elastic scattering to 3 gev. *Phys. Rev. C*, 62(3):034005, Aug 2000.

[81] V. A. Andreev *et al.* Polarizations for proton knockout reactions from $s(1/2)$ orbits at 1 GeV. *Phys. Rev.*, C69:024604, 2004.

[82] R. Szmytkowski. Some summation formulae for spherical spinors. *J. Phys. A: Math. Gen.*, 38:8993–9005, 2005.

[83] J. R. Vignote, M. C. Martinez, J. A. Caballero, E. Moya de Guerra, and J. M. Udias. A($\vec{e}, e'\vec{p}$)B responses from bare nucleons to complex nuclei. *Phys. Rev.*, C70:044608, 2004.

[84] F. X. Lee, L. E. Wright, and C. Bennhold. Quasifree pion electroproduction from nuclei in the delta region. *Phys. Rev.*, C55:318–337, 1997.

[85] J. Ryckebusch. Photoinduced two-proton knockout and ground-state correlations in nuclei. *Phys. Lett.*, B383:1–8, 1996.

[86] J. Ryckebusch and W. Van Nespen. The ^{16}O$(e, e'pp)^{14}$C reaction to discrete final states. *Eur. Phys. J.*, A20:435–441, 2004.

[87] G. Rosner. Probing short-range nucleon-nucleon correlations with virtual photons at MAMI. *Progress in Particle and Nuclear Physics*, 44:99 – 112, 2000. ISSN 0146-6410.

[88] C. J. G. Onderwater *et al.* Dominance of S-01 Proton-Pair Emission in the ^{16}O$(e, e'pp)$ Reaction. *Phys. Rev. Lett.*, 78:4893–4897, 1997.

[89] C. J. G. Onderwater *et al.* Signatures for Short-Range Correlations in ^{16}O Observed in the Reaction ^{16}O$(e, e'pp)$ ^{16}C. *Phys. Rev. Lett.*, 81:2213–2216, 1998.

[90] R. Starink *et al.* Evidence for short-range correlations in ^{16}O . *Phys. Lett.*, B474: 33–40, 2000.

[91] J. Ryckebusch *et al.* Electroinduced two-nucleon knockout and correlations in nuclei. *Nucl. Phys.*, A624:581–622, 1997.

[92] C. Giusti *et al.* Selectivity of the ^{16}O$(e, e'pp)$ reaction to discrete final states. *Phys. Rev.*, C57:1691–1702, 1998.

[93] T. De Forest. Off-Shell electron Nucleon Cross-Sections. The Impulse Approximation. *Nucl. Phys.*, A392:232–248, 1983.

[94] C. Gearhart. *Self-Consistently Dressed Nucleons and Nuclear Wave Functions*. PhD thesis, Washington University St.-Louis, 1994.

[95] S. Jeschonnek and J. W. Van Orden. A new calculation for $D(e, e'p)n$ at GeV energies. *Phys. Rev.*, C78:014007, 2008.

[96] M. J. Moravcsik, J. Pauschenwein, and G. R. Goldstein. Amplitude systems for spin-1/2 particles. *J. Phys. France*, 50:1167–1194, 1989.

[97] R. A. Arndt, W. J. Briscoe, I. I. Strakovsky, and R. L. Workman. Updated analysis of NN elastic scattering to 3 GeV. *Phys. Rev.*, C76:025209, 2007.

[98] S. Jeschonnek, Private Communication.

[99] R. D. Amado, J. Piekarewicz, D. A. Sparrow, and J. A. Mcneil. Dirac eikonal scattering amplitude. *Phys. Rev.*, C28:1663–1667, 1983.

[100] G. D. Alkhazov, S. L. Belostotsky, and A. A. Vorobev. Scattering of 1-GeV Protons on Nuclei. *Phys. Rept.*, 42:89–144, 1978.

[101] G. D. Alkhazov *et al.* Elastic scattering of 1 GeV protons from medium and heavy nuclei and nuclear densities. *Nucl. Phys.*, A381:430–444, 1982.

[102] D. R. Marlow *et al.* Pion scattering from C and Ca at 800 MeV/c. *Phys. Rev.*, C30: 1662, 1984.

[103] C. J. Joachain. *Quantum Collision Theory*. North-Holland Publishing Company, Amsterdam, 1975.

[104] W.-M. Yao *et al.* Review of Particle Physics. *Journal of Physics G*, 33:1+, 2006. URL http://pdg.lbl.gov.

[105] T. Lasinski, R. Levi Setti, B. Schwarzschild, and P. Ukleja. Energy dependence of the elastic diffraction slopes. *Nucl. Phys.*, B37:1–58, 1972.

[106] R. A. Arndt, W. J. Briscoe, I. I. Strakovsky, R. L. Workman, and M. M. Pavan. Dispersion relation constrained partial wave analysis of πN elastic and $\pi N \to \eta N$ scattering data: The baryon spectrum. *Phys. Rev.*, C69:035213, 2004.

[107] R. L. Workman, Private Communication.

[108] D. Debruyne, J. Ryckebusch, W. Van Nespen, and S. Janssen. The relativistic eikonal approximation in high-energy $A(e,e'p)$ reactions. *Phys. Rev.*, C62:024611, 2000.

[109] D. Debruyne, J. Ryckebusch, S. Janssen, and T. Van Cauteren. Bridging Two Ways of Describing Final-State Interactions in $A(e,e'p)$ Reactions. *Phys. Lett.*, B527:62–68, 2002.

[110] W. T. H. van Oers *et al.* Study of the ^{4}He$(p,2p)^3$H reaction at intermediate energies. *Phys. Rev.*, C25:390–407, 1982.

[111] G. R. Farrar, H. Liu, L. L. Frankfurt, and M. I. Strikman. Transparency in nuclear quasiexclusive processes with large momentum transfer. *Phys. Rev. Lett.*, 61:686–689, 1988.

[112] F. E. Low. A Model of the Bare Pomeron. *Phys. Rev.*, D12:163–173, 1975.

[113] B. K. Jennings and G. A. Miller. On color transparency. *Phys. Lett.*, B236:209, 1990.

[114] B. K. Jennings and G. A. Miller. Color transparency: The Wherefore and the why. *Phys. Rev.*, D44:692–703, 1991.

[115] B. K. Jennings and G. A. Miller. Color transparency and nonperturbative contributions to high-energy (p, p p) reactions. *Phys. Lett.*, B274:442–448, 1992.

[116] B. K. Jennings and G. A. Miller. Realistic hadronic matrix element approach to color transparency. *Phys. Rev. Lett.*, 69:3619–3622, 1992.

[117] B. Z. Kopeliovich and B. G. Zakharov. Quantum effects and color transparency in charmonium photoproduction on nuclei. *Phys. Rev.*, D44:3466–3472, 1991.

[118] B. Z. Kopeliovich and B. G. Zakharov. Preasymptotics of color transparency. *Phys. Lett.*, B264:434–439, 1991.

[119] B. Z. Kopeliovich, A. Schafer, and A. V. Tarasov. Nonperturbative effects in gluon radiation and photoproduction of quark pairs. *Phys. Rev.*, D62:054022, 2000.

[120] B. Z. Kopeliovich, J. Nemchick, N. N. Nikolaev, and B. G. Zakharov. Novel color transparency effect: Scanning the wave function of vector mesons. *Phys. Lett.*, B309: 179–186, 1993.

[121] B. Z. Kopeliovich, J. Nemchick, N. N. Nikolaev, and B. G. Zakharov. Decisive test of color transparency in exclusive electroproduction of vector mesons. *Phys. Lett.*, B324:469–476, 1994.

[122] O. Benhar, B. G. Zakharov, N. N. Nikolaev, and S. Fantoni. Nuclear effects in the diffractive electroproduction of s anti-s mesons. *Phys. Rev. Lett.*, 74:3565–3568, 1995.

[123] B. Z. Kopeliovich, J. Nemchik, and I. Schmidt. Color transparency at low energies: Predictions for JLAB. *Phys. Rev.*, C76:015205, 2007.

[124] S. Frankel, W. Frati, and N. Walet. Extracting nuclear transparency from $p-A$ cross-sections. *Nucl. Phys.*, A580:595–613, 1994.

[125] K. I. Blomqvist *et al.* Investigation of short-range nucleon nucleon correlations using the reaction ^{12}C$(e,e'pp)$ in close to 4π geometry. *Phys. Lett.*, B421:71–78, 1998.

[126] D. Dutta, Private Communication.

[127] H. Gao, R. J. Holt, and V. R. Pandharipande. $\gamma n \to \pi^- p$ process in ^{4}He and ^{16}O. *Phys. Rev.*, C54:2779–2782, 1996.

[128] B. Clasie, Private Communication.

[129] T. Horn. *The pion charge form factor through pion electroproduction*. PhD thesis, University of Maryland, 2006.

[130] A. Larson, G. A. Miller, and M. Strikman. Pionic color transparency. *Phys. Rev.*, C74: 018201, 2006.

[131] M. M. Kaskulov, K. Gallmeister, and U. Mosel. Pionic transparency in semi-exclusive electroproduction off nuclei. *Phys. Rev.*, C79:015207, 2009.

[132] URL http://gibuu.physik.uni-giessen.de/GiBUU.

[133] K. Gallmeister and T. Falter. Space-time picture of fragmentation in PYTHIA / JETSET for HERMES and RHIC. *Phys. Lett.*, B630:40–48, 2005.

[134] B. Andersson, G. Gustafson, G. Ingelman, and T. Sjostrand. Parton Fragmentation and String Dynamics. *Phys. Rept.*, 97:31–145, 1983.

[135] A. S. Carroll *et al.* Absorption Cross-Sections of π^{+-}, K^{+-}, p and anti-p on Nuclei Between 60 GeV/c and 280 GeV/c. *Phys. Lett.*, B80:319, 1979.

[136] E. Piasetzky and I. Pomerantz, Private Communication.

[137] J. J. Kelly. Nucleon knockout by intermediate-energy electrons. *Adv. Nucl. Phys.*, 23: 75–294, 1996.

[138] G. Jacob and T. A. J. Maris. Quasi-free scattering and nuclear structure. 2. *Rev. Mod. Phys.*, 45:6–21, 1973.

[139] K. Hatanaka *et al.* Exclusive Measurement of Proton Quasifree Scattering and Density Dependence of the Nucleon-Nucleon Interaction. *Phys. Rev. Lett.*, 78:1014–1017, 1997.

[140] T. Kobayashi *et al.* $(p, 2p)$ reactions on C-(9-16) at 250-MeV/A. *Nucl. Phys.*, A805: 431–438, 2008.

[141] T. Aumann. Prospects of nuclear structure at the future GSI accelerators. *Prog. Part. Nucl. Phys.*, 59:3, 2007.

[142] S. Strauch *et al.* Polarization transfer in the ^{4}He$(\vec{e}, e'\vec{p})^3$H reaction up to $Q^2 = 2.6$ (GeV/c)^2. *Phys. Rev. Lett.*, 91:052301, 2003.

[143] A. Gade *et al.* Reduction of spectroscopic strength: Weakly-bound and strongly-bound single-particle states studied using one- nucleon knockout reactions. *Phys. Rev.*, C77:044306, 2008.

[144] M. S. Hussein, R. A. Rego, and C. A. Bertulani. Microscopic theory of the total reaction cross-section and application to stable and exotic nuclei. *Phys. Rept.*, 201: 279–334, 1991.

[145] W. Reuter, G. Fricke, K. Merle, and H. Miska. Nuclear charge distribution and rms radius of C-12 from absolute elastic electron scattering measurements. *Phys. Rev.*, C26:806–818, 1982.

[146] R. J. Furnstahl, B. D. Serot, and H.-B. Tang. A chiral effective lagrangian for nuclei. *Nucl. Phys.*, A615:441–482, 1997.

[147] W. Greiner. *Relativistic Quantum Mechanics: Wave Equations*. Springer-Verlag, Berlin, 2000.

Samenvatting

Inleiding

Sinds de ontwikkeling in de jaren ’50 en ’60 van kwantumchromodynamica (QCD) als ijktheorie voor de sterke wisselwerking, weet men dat quarks en gluonen de fundamentele bouwstenen vormen voor haast alle zichtbare materie. Door het confinementgedrag van QCD, treden bij lage energieën echter kleurloze baryonen en mesonen naar voren als effectieve vrijheidsgraden. De beschrijving aan de hand van deze hadronische vrijheidsgraden is in de nucleaire- en hadronfysica al geruime tijd zeer efficiënt en succesvol gebleken. Bij welke energieschaal en op welke wijze de transitie van hadronische naar de partonische vrijheidsgraden plaatsvindt, is nog steeds niet opgehelderd en vormt heden ten dage een zeer actief en boeiend onderzoeksgebied. Om deze overgang in kaart te brengen gaat men op zoek naar QCD-gerelateerde fenomenen die afwijken van wat door de nucleaire fysica standaard voorspeld wordt.

Een voorbeeld van zo’n fenomeen is kleurtransparantie. Bij reacties met een hoge vierimpulstransfer, voorspelt QCD dat hadronen in een toestand met een kleine dwarsdoorsnede gevormd worden. Deze kleine objecten lijken kleurloos, en ondervinden verminderde reacties met het medium waarin ze gevormd worden alvorens te evolueren tot een normale hadronische toestand. In de zoektocht naar kleurtransparantie meet men de nucleaire transparantie, een observabele die een maat vormt voor de attenuatie van een hadron in een medium. Kleurtransparantie zou zich manifesteren als een stijging van de transparantie bij toenemende energieën. Transparanties werden al voor verschillende reacties gemeten, maar tot nog toe is de aanvang van het fenomeen van kleurtransparantie niet eenduidig vastgesteld. De voorbije jaren werden in Jefferson Lab experimenten uitgevoerd waarin men de transparantie gemeten heeft bij foto- en elektroproductie van het pion, en tweenucleon-uitstootreacties. In dit werk wordt de transparantie berekend in de kinematische gebieden die overeenkomen met bovenvermelde experimenten.

Korte-drachtscorrelaties zijn een tweede afwijking van de standaardbeschrijving van nucleaire systemen die in dit werk van naderbij bekeken worden. Korte-drachtscorrelaties ontstaan door de repulsieve kern en het tensorgedeelte van de nucleon-nucleonkracht. Omdat deze delen van de nucleon-nucleonkracht niet compatibel zijn met een typische gemiddeldveldbenadering, vindt men de korte-drachtscorrelaties niet terug in het traditionele schillenmodel. De sterke afstoting creëert nucleonparen met een hoge relatieve impuls en zorgt voor fluctuaties van hoge dichtheid in de kern.

Formalisme

In dit werk wordt een relativistisch en kwantummechanisch raamwerk uiteengezet dat gebruikt wordt om exclusieve uitstootreacties aan kernen te beschrijven en dat geen enkele vrije parameter bevat. Het wordt hier specifiek toegepast op foto- en elektroproductie van pionen en twee-nucleon foto-uitstootreacties. Bij het modelleren van uitstootreacties verdienen drie deelproblemen onze aandacht:

- De beschrijving van de harde reactie, die de uitstoot van de deeltjes veroorzaakt.
- De structuur van de golffuncties voor de trefkern en de restkern.
- De behandeling van de finale-toestandsinteracties (FSI), die de invloed van het nucleaire medium op de uitgaande deeltjes uitdrukken.

De interactie van de inkomende probe gebeurt bij alle reacties in de impulsbenadering. Bij de foton- en elektrongeïnduceerde productiereacties van pionen, wordt voor het beschrijven van de harde reactie gebruik gemaakt van een zogenaamde gefactoriseerde benadering voor de werkzame doorsnede. Hierbij wordt amplitude van het uitstootproces gerelateerd aan die van het vrije proces, waarna de werkzame doorsnede van het vrije proces optreedt als een factor in die van het proces aan een kern. Voor de fotongeïnduceerde uitstoot van twee nucleonen worden twee concurrerende reactiemechanismes ongefactoriseerd behandeld. Het eerste beschrijft de reactie als een eenstapsproces waarbij het inkomend foton interageert met één van de nucleonen in een gecorreleerd paar waarbij dit nucleon de kern verlaat. Het tweede nucleon blijft achter met een hoge impuls, waardoor het de kern ook kan verlaten. Het gecorreleerd nucleonpaar wordt beschreven d.m.v. golffuncties die zich in een relatieve $^1S_0$ toestand bevinden. Het tweede reactiemechanisme gebruikt een tweestapsproces waarbij het foton interageert met een nucleon dat op zijn baan uit de kern een tweede harde reactie veroorzaakt met een tweede nucleon, dat daardoor ook uit de kern vliegt. Om deze harde herverstrooiing te beschrijven wordt er gebruik gemaakt van de nucleon-nucleonverstrooiingsamplitudes uit de SAID database.

Voor de beschrijving van alle inkomende en uitgaande deeltjes worden relativistische golffuncties gebruikt. De golffunctie van de tref- en restkern wordt bekomen in het nucleaire schillenmodel. Hierbij bewegen de individuele nucleonen van de kern in een gemiddeld-veldpotentiaal opgewekt door alle andere nucleonen. De totale golffunctie van de kernen neemt de vorm aan van een Slater-determinant. De relativistische één-deeltjesgolffuncties worden bekomen in de Hartree-benadering van het $\sigma - \omega$ model.

Bij voldoende hoge energieën wordt de invloed van het nucleaire medium op de uitgestoten deeltjes berekend in een relativistische Glauber veelvoudige-verstrooiingsbenadering (RMSGA). De Glauber-beschrijving, voor het eerst toegepast in optica, is een eikonale benadering en steunt op de kleine golflengte van het deeltje in vergelijking met de dracht van de potentiaal. De verstrooiingen gebeuren over kleine hoeken en zijn elastisch of licht inelastisch. De banen van de uitgestoten deeltjes worden door een lineair traject beschreven en de residuele nucleonen worden *bevroren* tijdens de verstrooiingen. De implementatie van de RMSGA benadering gebeurt d.m.v. een scalaire Glauber-operator die inwerkt op de golffunctie van het uitgaand deeltje. Elke verstrooiing met een residueel nucleon voegt een extra fase toe aan deze operator. Deze Glauber-operator hangt van drie verstrooiingsparameters af. Voor de numerieke bepaling van deze parameters worden fits aan pion-nucleon- en nucleon-nucleonverstrooiingsdata gebruikt.

Voor uitgestoten nucleonen met een lage impuls, waarvoor de onderliggende aannames van de Glauber-benadering niet meer toepasbaar zijn, voorziet het model ook de mogelijkheid om de FSI te beschrijven met behulp van een ROMEA model in een eikonale benadering. Het ROMEA model steunt op optische potentialen om de interacties van de uitgaande deeltjes met het nucleaire medium te beschrijven. In tegenstelling tot de aanpak van de RMSGA benadering, die steunt op nucleon-nucleonverstrooiing, zijn deze optische potentialen gebaseerd op globale fits aan elastische nucleon-kern verstrooiingsdata.

De implementatie van het kleurtransparantie-effect gebeurt in het kwantumdiffusiemodel van Farrar e.a. De totale werkzame doorsnede voor pion-nucleon- en/of nucleon-nucleonverstrooiing (die één van de Glauber-parameters is), wordt vervangen door een effectieve werkzame doorsnede. Deze evolueert lineair van een gereduceerde waarde over een bepaalde formatielengte tot zijn normale waarde.

De invloed van korte-drachtscorrelaties kan toegevoegd worden aan de berekening van de FSI. De ééndeeltjesdichtheid in de integralen bij de berekening van de Glauber-operator wordt vervangen door een gemodificeerde dichtheid die rekening houdt met de aanwezigheid van een nucleon op de plaats van de harde interactie. Deze gemodificeerde dichtheid vertoont een gat op de plaats van de harde interactie, veroorzaakt door de harde kern van de nucleon-nucleoninteractie. Dichtheden aan de rand van dit gat zijn hoger dan de gewone

ééndeeltjesdichtheid. De normalisatie blijft behouden bij het gebruik van de gemodificeerde dichtheid, door het invoeren van een extra functie die afhankelijk is van de coördinaat van de harde interactie. Deze functie vormt de oplossing van een integraalvergelijking, die numeriek opgelost wordt.

Numerieke resultaten

De resultaten van de numerieke berekeningen werden samengevat in hoofdstuk 3. Dit hoofdstuk begint met de numerieke analyse van de Glauber-FSI-factor (die alle informatie omtrent de attenuatie door het nucleaire medium omvat) voor een uitgestoten pion en nucleon uit koolstof met een kinematiek die overeenstemt met die waarvoor in Jefferson Lab data werden genomen. De analyse toont aan dat het effect van de verstoringen in de norm en fase van de FSI-factor sterker wordt naarmate meer materie doorkruist wordt. De invloed van de FSI-factor op de impulsdistributies van de nucleonen laat zien dat het signaal sterk gereduceerd wordt in de aanwezigheid van de finale-toestandsinteracties.

Het hoofddoel van dit werk is het uitvoeren van berekeningen met een kinematiek die overeenstemt met die van de hierboven aangehaalde transparantie-experimenten uitgevoerd in Jefferson Lab. Berekeningen voor de fotongeïnduceerde pionproductiereactie tonen een transparantie die relatief weinig afhangt van de harde schaal. De toevoeging van korte-drachtscorrelaties zorgt voor een toename in de transparantie van ongeveer 5%, onafhankelijk van de harde schaal. Berekeningen met inclusie van het kleurtransparantie-effect tonen een volledig andere afhankelijkheid van de harde schaal. De invloed op de transparantie varieert van ongeveer 0% bij de laagst opgemeten fotonenergie tot meer dan 20% bij de energieën die beschikbaar zullen zijn na de 12-GeV-upgrade van JLab. Een vergelijking met de data en een semi-klassieke berekening laat zien dat de RMSGA-berekeningen deze in het ganse energiebereik overschatten en er niet in slaagt de lage $|t|$-afhankelijkheid te reproduceren. Bij hogere energie is de helling van de data wel in goede overeenstemming met de berekeningen waarbij kleurtransparantie in rekening werd gebracht. Transparantieberekeningen met de RMSGA- en ROMEA-aanpak in het energiegebied waar ze beide toepasbaar zijn, tonen verschillen van ongeveer 5% tussen beide modellen, die bovendien kleiner worden bij hogere energie.

Voor de elektrongeïnduceerde productiereactie van pionen bevestigen de berekeningen dat de korte-drachtscorrelaties en kleurtransparantie-effecten op verschillende manieren afhankelijk zijn van de harde schaal. De energie- en A-afhankelijkheid van de data vertonen bovendien duidelijke afwijkingen van de voorspellingen uit de traditionele nucleaire fysica, hetgeen in zeer goede overeenstemming is met zowel de RMSGA-berekeningen die het

kleurtransparantie-effect bevatten, als resultaten uit een semiklassiek model. Meer bewijs voor de modelonafhankelijkheid van de transparantieberekeningen wordt geleverd door extra vergelijkingen met resultaten uit het semiklassiek model. Deze vertonen gelijkaardige trends, met RMSGA-berekeningen die meestal ongeveer 5% hoger liggen.

Resultaten in zowel het een- als tweestapsreactiemechanisme voor de fotongeïnduceerde twee-nucleonuitstootreactie, tonen transparanties die duidelijk lager liggen dan wat men uit een één-protonuitstootreactie zou verwachten. Dit is het gevolg van het feit dat beide reactiemechanismes zones met hoge dichtheid in de kern bereiken. Hoge dichtheden betekenen meer FSI, en dus lagere transparanties. Bij de tweestaps-harde-herverstrooiingsreactie wordt het effect van de nucleon propagator FSI op de transparantie bepaald op 5%.

In een laatste deel, worden de robuustheid en veelzijdigheid van het Glauber-raamwerk aangewend om een consistente vergelijkende studie van de effectief bereikte dichtheid te maken voor uitstootreacties met één $\big((e,e'p)\big)$, twee $\big((\gamma,pp)\big)$ en drie $\big((p,2p)\big)$ nucleonen. Vergelijkingen in een koolstof- en een ijzerkern tonen dat de (γ,pp)-reactie de hoogste dichtheid in het centrum van de kern bereikt. Door de sterke initiële-toestandsinteracties is de $(p,2p)$-reactie sterk aan het oppervlak gelocaliseerd, waar het een eerder lage dichtheid bereikt. De $(e,e'p)$-reactie valt ergens tussen deze twee uitersten. Het verschil in effectieve dichtheid tussen de drie reacties was minder uitgesproken voor de ijzerkern dan voor de koolstofkern.

Conclusie

We hebben een relativistisch formalisme ontwikkeld dat gebruikt werd voor de modellering van foton- en elektrongeïnduceerde pionproductie aan kernen. Ook de twee-nucleonuitstootreactie kan worden beschreven, zowel in een eenstapsreactie (uitstoot van een gecorreleerd paar) als tweestapsreactie (harde herverstrooiing). De FSI van de pionen en nucleonen worden behandeld in het RMSGA-model. Voor nucleonen met lage impuls is er ook een beschrijving in het ROMEA-model mogelijk. Transparantieberekeningen toonden een duidelijk verschil in de manier waarop korte-drachtscorrelatie- en kleurtransparantie-effecten afhankelijk zijn van de harde schaal. De data voor pion elektroproductie waren bovendien in zeer goede overeenstemming met de berekeningen die het kleurtransparantie-effect in rekening brachten.

In de toekomst, na de upgrade van de Jefferson Lab versneller tot 12 GeV, zullen experimenten ons meer kunnen leren over het verloop van de transparantie bij hogere energieën. Ook kan het model nog verder uitgebreid worden en beschrijvingen voor uitstootreacties met een kaon- of rho-meson voorzien. Verbeteringen die nog mogelijk zijn in het model zijn

bijvoorbeeld het gebruik van meer realistische golffuncties voor lichte kernen, het toevoegen van tensorcorrelaties, en een beschrijving voor de korte-drachtscorrelaties die vertrekt vanuit partonische vrijheidsgraden.